Physical Aspects of Spreadable semi-solid Animal Protein Emulsions

Dissertation zur Erlangung des Grades

Doktor rerum naturalium (Dr.rer.nat.)

im Promotionsfach Chemie

am Fachbereich 09
Chemie, Pharmazie, Geographie und Geowissenschaften
der Johannes Gutenberg-Universität Mainz

Mathias Bächle

1. Gutachter:

[redacted]

2. Gutachter:

[redacted]

Tag der mündlichen Prüfung: tba

Declaration of Authorship

I hereby declare that I wrote this dissertation submitted without any unauthorized external assistance and used only sources acknowledged in the work. All textual passages which are appropriated verbatim or paraphrased from published and unpublished texts as well as all information obtained from oral sources are duly indicated and listed in accordance with bibliographical rules. In carrying out this research, I complied with the rules of standard scientific practice as formulated in the statutes of Johannes Gutenberg-University Mainz to insure standard scientific practice.

Mathias Bächle
Mainz, 17. April 2025

“*’An apple a day keeps the doctor away.’ - ’Na dann hör’ auf Äpfel zu essen!*”

- C.B.

Abstract

This thesis investigates the physical aspects of semi-solid animal protein emulsions, specifically foie gras pâté and duck liver pâté, with the goal of developing a foie gras alternative without the need for force-feeding. By characterizing these systems using various analytical techniques, such as rheology, textural force measurements, differential scanning calorimetry (DSC) and coherent anti-stokes Raman scattering (CARS) microscopy, unique insights were gained into their textural properties and microstructure.

A key focus was the comparison between foie gras pâté and a simplified duck liver pâté composed of rendered duck fat. Experimental findings showed that foie gras pâté exhibited significantly higher viscoelastic properties and hardness than the control pâté, attributed to its unique fat particle clusters, which support the protein network and contribute to its textural properties. These clusters, observed through CARS microscopy, acted as hard filler particles, increasing the pâté's structural integrity but also causing rapid collapse under shear stress.

Two approaches were explored to modify the properties of the liver-based emulsion: the systematic use of different emulsifiers and the alteration of fat structure via lipase treatment.
The study examined the effect of three stabilizers and emulsifiers — collagen, sodium stearate, and mono- and diglycerides (MDG) — on the physical properties and microstructure of the emulsion. Each emulsifier influenced the texture differently; collagen increased elasticity and hardness, sodium stearate increased hardness due to increasing electrostatic repulsion, and MDG affected rheological properties primarily in the unheated state. Additionally, emulsifiers led to a reduction in fat particle size and improved dispersion within the emulsion.

A successful approach to mimicking foie gras pâté involved treating duck fat with lipase. The enzymatic modification altered the fat's melting profile and solid fat content without changing its fatty acid composition. This lipase-treated fat replicated the structural characteristics of foie gras fat, leading to pâtés with similar rheological and textural properties and a similiar microstructure.

Overall, this research demonstrates the importance of understanding emulsion-based food systems to effectively manipulate their properties. The findings highlight the crucial role of fat particle structure in determining foie gras pâté's texture and provide a foundation for creating ethical and high-quality foie gras alternatives and enzymatic fat modification.

Zusammenfassung

In dieser Arbeit werden die physikalischen Aspekte halbfester Emulsionen aus tierischen Proteinen untersucht, insbesondere Foie Gras-Pastete und Entenleberpastete, mit dem Ziel, eine Stopfleberalternative ohne Zwangsfütterung zu entwickeln. Durch die Charakterisierung dieser Systeme mit Hilfe verschiedener Analysetechniken wie Rheologie, Texturkraftmessungen, Differential-Scanning-Kalorimetrie (DSC) und kohärenter Anti-Stokes-Raman-Streuung (CARS) wurden einzigartige Einblicke in ihre texturellen Eigenschaften und Mikrostruktur gewonnen.

Ein Schwerpunkt war der Vergleich zwischen Foie Gras-Pastete und einer Entenleberpastete aus ausgelassenem Entenfett, Leber und Wasser . Die Versuchsergebnisse zeigten, dass Stopfleberpastete deutlich steifer, aber auch weniger elastisch ist und eine höhere Festigkeit aufweist als die Kontrollpastete, was auf die einzigartigen Fettpartikelstruktur zurückzuführen ist, die das Proteinnetzwerk unterstützen und zu den Textureigenschaften beitragen. Diese Cluster, die mit Hilfe der CARS-Mikroskopie beobachtet wurden, wirkten wie harte Füllpartikel, die die strukturelle Integrität der Pastete erhöhten, aber auch zu einem schnelleren Zusammenbruch unter Scherbeanspruchung führten.

Es wurden zwei Ansätze untersucht, um die Eigenschaften der Emulsion auf Leberbasis zu verändern: die systematische Verwendung verschiedener Emulgatoren und die Veränderung der Fettstruktur durch Lipase-Behandlung.
In der Studie wurde die Wirkung von drei Emulgatoren - Kollagen, Natriumstearat und Mono- und Diglyceride (MDG) - auf die physikalischen Eigenschaften und die Mikrostruktur der Emulsion untersucht. Jeder Emulgator beeinflusste die Textur auf unterschiedliche Weise; Kollagen erhöhte die Elastizität und Festigkeit , Natriumstearat erhöhte die Festigkeit aufgrund der zunehmenden elektrostatischen Abstoßung, und MDG beeinflusste die rheologischen Eigenschaften vor allem im nicht erhitzten Zustand. Darüber hinaus führten Emulgatoren zu einer Verringerung der Fettpartikelgröße und verbesserten die Dispersion innerhalb der Emulsion.

Ein vielversprechender Ansatz zur Nachbildung von Gänseleberpastete bestand darin, Entenfett gezielt mit Lipase zu behandeln. Durch diese enzymatische Modifikation veränderte sich das Schmelzverhalten sowie der Anteil an festem Fett, während die Fettsäurezusammensetzung erhalten blieb. Das Fett hat damit die gleichen texturgebenden Eigenschaften wie das natürlichen Stopfleberfett. Das Ergebnis waren Pasteten mit vergleichbarer Konsistenz und Textur und einer ähnlichen Mikrostruktur wie das Original.

Insgesamt zeigt diese Arbeit, wie wichtig es ist, emulsionsbasierte Lebensmittelsysteme zu verstehen, um ihre Eigenschaften wirksam zu beeinflussen. Die Ergebnisse unterstreichen die entscheidende Rolle der Fettpartikelstruktur auf die Textur von Stopfleberpasteten und bilden eine Grundlage für die Entwicklung ethischer und hochwertiger Stopfleberalternativen und die enzymatische Fettmodifikation.

Publications Covered in this Thesis

Chapter 3:

Via, M. A.; **Baechle, M.**; Stephan, A.; Vilgis, T. A.; Clausen, M. P. Microscopic characterization of fatty liverbased emulsions: Bridging microstructure and texture in foie gras and pâté. *Physics of Fluids* 33, 117119 (2021)
https://doi.org/10.1063/5.0070998

Chapter 4:

Baechle, M.; Via, M. A.; Clausen, M. P.; Vilgis, T. A. Function of different emulsifiers in spreadable meat emulsions: A systematic study of physical properties *Food Biophysics* 20, 57 (2025) https://doi.org/10.1007/s11483-025-09941-2

Chapter 5:

Baechle, M.; Marques, A. M. L.; Via, M. A.; Clausen, M. P.; Vilgis, T. A. Foie gras pâté without force feeding. *Physics of Fluids* 37, 037196 (2025)
https://doi.org/10.1063/5.0255813

Other publications:

Ghebremedhin, M.; **Baechle, M.**; Vilgis, T. A. Meat-, vegetarian-, and vegan sausages: Comparison of mechanics, friction, and structure *Physics of Fluids* 34, 047112 (2022)
https://doi: 10.1063/5.0083730

Barua, S.; Hanewald, A.; **Baechle M.**; Mezger, M.; Srivastav, P. P.; Vilgis, T. A. Insights into the structural, thermal, crystalline and rheological behavior of various hydrothermally modified elephant foot yam (Amorphophallus paeoniifolius) starch *Food Hydrocolloids* 129 (2022) 107672
https://doi.org/10.1016/j.foodhyd.2022.107672

Outline and Contribution

This thesis focuses on the investigation of the physical properties of semi-solid protein emulsions, in particular duck liver and foie gras pâté, by combining different mechanical methods and microscopy to obtain the microstructure. In addition, the influence of different emulsifiers on the protein emulsion was investigated using the developed methods. The structure of liver pâté was also modified by lipase treatment of the fat to obtain similar textural and microstructural properties as foie gras pâté.

Chapter 3 investigates the differences between a simple homemade duck liver pâté and a foie gras pâté by rheological and force measurements. In addition, the emulsion structure was imaged by CARS microscopy and related to the mechanical behaviour. The fat particle structure was found to be the main contributor to the textural properties. M.A.V.: CARS imaging, image analysis, statistical analysis, manuscript draft, figures 3.3 to 3.6; **M.B.**: sample preparation, texture analysis, rheology measurements, writing, figures 3.1 and 3.2; A.S.: supervision, providing materials and funding; T.A.V.: project idea, interpretation, model development, supervision, writing, figure 3.7; manuscript review; M.P.C.: experimental design, interpretation, supervision, writing, manuscript review.

Chapter 4 investigates the influence of distinct emulsifiers on an identical matrix based on a liver protein emulsion. The samples were prepared with different concentrations of each emulsifier: collagen, sodium strearate and mono- and diglycerides of fatty acids. By combining mechanical methods such as rheology and texture measurements with CARS microscopy, the distinct effect of each surfactant could be studied. They show different effects on the structure depending on their molecular characteristics.
M.B.: sample preparation, texture analysis, rheology measurements, image analysis, statistical analysis, manuscript draft, figures; M.A.V.: CARS imaging, image analysis, statistical analysis; M.P.C.: experimental design, interpretation, manuscript review; T.A.V.: project idea, interpretation, model development, supervision, writing, manuscript review.

Chapter 5 discusses the treatment of native duck fat with *Candida rugosa type VII* lipase to mimic the fat structure of foie gras fat. The fat was analysed by various analytical methods such as DSC, NMR and XRD to verify its properties. The fat was used to produce a pâté with properties similar to those of foie gras pâté. The pâtés were analysed by rheology, texture measurements and CARS microscopy and it was found that the treated pâté had similar fat particle clusters to the foie gras pâté.
M.B.: sample preparation, texture analysis, rheology measurements, statistical analysis; manuscript draft; writing; figures; A.M.L.M: CARS imaging, image analysis; M.A.V.: CARS imaging, image analysis, figure 5.9; M.P.C.: experimental design, interpretation, supervision, writing, manuscript review; T.A.V.: project idea, interpretation, model development, supervision, writing, manuscript review, figures.

Contents

List of Figures

List of Tables

Chapter 1

Introduction

Liver pâté or liver sausage is a common cooked sausage worldwide and is made from cooked fatty meat, e.g. pork back fat, or pure fat emulsified with raw liver and pasteurized to obtain the final product[1]. A wide range of animal livers are used for patés, including beef, pork, poultry and shellfish, but mainly pork and duck liver patés are sold commercially[2, 3]. Scientifically, liver pâté is classified as a semi-solid emulsion composed mainly of proteins, fats and water, and is considered a typical example of soft matter due to its viscoelastic properties.[4]. The emulsion is formed by dispersing the fat in a protein-rich aqueous phase. The emulsifying capacity of liver proteins is high enough to form a stable emulsion and they form a weak gel when heated[4–6]. However, research on this type of food is limited and in recent years has focused on special interests such as fat replacement and nutritional improvement. Some older publications focused on textural properties and tried to map the emulsion structure. Initially, scientists focused on the influence of different fat types and livers on the stability of the paste batter[7–9].

Since about 2010, research articles have been published with the aim of investigating the viscoelastic properties of liver pâtés. Notable work in this area has been carried out by Steen et al. [4] with a study of the effect of salt and liver/fat ratio on the viscoelastic properties of liver paté. Salt increases the amount of solubilized proteins, which influences the viscoelastic parameters such as the storage modulus (G') of the different production steps. An increase in the storage modulus was observed for the liver paste batter and the final product when salt was added. On the other hand the liver/fat ratio (35 %/35 % compared to 20 %/50 %) has no effect on the viscoelastic properties of the final product. The effect of the presence of higher amounts of liver protein (35 %/35 %) is probably compensated by the increase in fat crystallisation at higher fat contents (20 %/50 %). They then performed emulsion stability tests and texture profile analysis on the same samples and imaged the emulsion microstructure using light microscopy. The higher salt and liver content resulted in more stable emulsions and smaller fat droplet distribution. However, the effect of salt and liver/fat ratio has no effect on the hardness of the final product[10]. These results were later supported by a study by Steen et al. [5] that liver proteins have great emulsifying properties, while foaming and gelling properties are limited compared to other proteins. Another study, more focused on fat composition and its influence on textural properties,

was carried out by Tiensa et al. [11]. They investigated the fatty acid composition, solid fat content and melting point of commercially available pâtés and related it to hardness. They also imaged the microstructure of the pâtés with light microscopy. An interesting approach of studying the gelation of proteins during heating was done by Pětová et al. [12], they measured the change in viscoelastic properties *in situ* during the heating process and reported an initial decrease in storage modulus up to about $\approx 58\,^{\circ}\mathrm{C}$ and which increases again during cooling.
In recent years, more research has focused on changing the composition of the liver pâté by reducing or partially replacing the fat, while maintaining their usually textural properties. Delgado-Pando et al. [13] investigated the total or partial replacement of fat with an oil/konjac gel to increase the content of polyunsaturated fatty acids (PUFA) in the pâtés. It was shown that the textural properties were affected by the addition of the oil emulsion due to the higher water content. However, the nutritionally improved pâtés still had good sensory results. The influence of different amounts of an oil-based emulsion and the addition of konjac gel on the textural properties was studied. Barbut et al. [14] investigated the use of organogels as fat replacers in meat products. Five different oleogels, prepared by gelling carnola oil with ethyl celluose and glycerol monostrearate, were used to replace pork fat in liver paté. It was found that two organogel compositions resembled the textural properties of the pork control pâté quite well[15]. However, the pâtes had a larger fat globule size and lacked oil retention and colour compared to the control pâté. This was further investigated with a partial replacement of pork fat with canola oil organogels, and it was shown that a replacement of 60 % of pork fat with organogel maintained the textural properties and improved the oil retention and colour of the pâté[16]. Lately, similar approaches were investigated by the use of sunflower oleogels, mushrooms, modified starches and microencapsulated fish oil to replace fat in liver pâtés[17–20].
The focus appears to be on modifying specific aspects, such as nutritional value, while maintaining certain textural properties, which has often been achieved using additives widely used in the food industry. However, a systematic approach investigating the influence of emulsifiers on a basic matrix based on liver, fat and water is still lacking. Such research, focusing on the molecular interactions of specific emulsifiers on a liver-based emulsion, provides insights to predict textural changes and microstructure of paté preparations and helps to understand interactions with other additives or replacements.

A well-known liver pâté speciality is foie gras pâté, which literally means 'fatty liver' in French and is made from force-fed duck and goose. Apart from being served as a dish, fried or poached, foie gras is mainly eaten as a pâté by adding spices and carefully mixing and pasteurising it[21]. Compared to liver pâtés made with spontaneously fattened duck liver and rendered duck fat, a foie gras pâté has a better melting and soft mouthfeel, which increases the release of flavours and coating of the palate. It is therefore a food product appreciated for its rich and smooth texture[22, 23]. However, this delicacy comes at a cost to animal welfare, as ducks and geese are

force-fed a high-calorie diet for up to fourteen days to produce a fatty liver[24]. After this procedure, such a liver is about 7 times larger than a spontaneously fattened liver and has about 60 % to 70 % fat content[25]. This process of force-feeding the animals is banned in many countries, as is the commercial distribution of foie gras and its products[26].
Research on foie gras has been limited in recent years. A few publications focus on the physiological processes that take place during force-feeding and the breed of animals used[25, 27]. The yield and nutritional values, such as fatty acid composition, fat and protein, of foie gras are studied and compared with non-force-fed liver as well[25, 28]. An interesting study tackled the differences in Aroma components of fried foie gras and natural geese liver as well as the fat content. They were estimated using gas chromatography with an attached mass spectrometer detector and sensory panels[28]. Another focus of the research is the conditions under which the animals are reared and the welfare aspects of the animal[26, 29]. A study by Théron et al. [30] focuses more on the behaviour of proteins during heating and how they are involved in the fat loss of different types of foie gras. A combination of histology and fluorescence microscopy was used to assess the size of fat droplets, improving on previous results[31]. A study by Carrillo et al. [32] determined the thermal properties of foie gras, foie gras paté, foie gras fat and duck fat. In addition to density, thermal conductivity and specific heat were determined. A mathematical model was derived to predict the values as a function of temperature in order to optimise pasteurisation times.
However, it is noticable that so far no research aimed to investigate the textural properties of the foie gras pâté in a complete manner and the differences between liver pâtés and foie gras pâtés are not fully understood yet, hence their noticeable culinary differences. This knowledge would be useful to improve liver pâtés so that they have a desired textural profile.

In some countries, such as France, Belgium, China and Canada, the demand for foie gras is high and its production is widespread[24]. Today, the ethical aspects of food production are more relevant to consumers and the demand for non-force-fed foie gras products is growing. Despite there is a lack of literature on textural properties, some attempts have been made to emulate the special texture and rich mouthfeel of foie gras. Some achieve this by adding fats and additives from other sources[33] or increasing the collagen content by extracting it from skin and adipose tissue[34]. Plant-based alternatives to sea foie gras, the fatty liver of monk fish, have also been reported in the literature. Recently, Nicholson and Marangoni [35] reported a remarkable method to influence the properties, such as melting behaviour and solid fat content, by applying lipase and cleaving the fatty acid from the triglycerides. They were able to increase the solid fat content of cottonseed and peanut oil by a factor of three and produce margarines with similar properties to commercial products.

First, an overview of the theoretical background and methods used in this thesis are presented in chapter 2.
Then, a systematic approach to obtain the textural properties of liver and foie gras pâté is presented inc Chapter 3. Rheological and texture analyser measurements were connected to microstructure obtained by CARS-Microscopy. Additionally, the sizes and shapes of the fat particle were evaluated.
In chapter 4 a study of different emulsifiers (collagen, sodium stearate and mono- and diglycerides of fatty acids) incorporated at different concentrations in a liver fat emulsion matrix is presented. After preparation, the microstructure was imaged using CARS microscopy and the textural properties were determined using rheology and texture analysis.
Combined with the results of chapters 3 and 4, a novel way of producing foie gras pâté with similar textural properties is presented in chapter 5. An intencive analysis of the treated fat is conducted and the pâté was characterised as described in the previous chapters.
In the chapter 6, the lipase-treated pâté is compared with a commercial product that is also made without force-feeding.
Chapter 7 contains a conclusion and outlook. In appendix A the supporting information from the publications are presented.

Chapter 2

Theoretical Background

The theoretical background and methods in this chapter are presented with a focus on food systems and food technology applications.

2.1 Theoretical fundamentals

2.1.1 Emulsions

Colloidal systems are mixtures of two (or more) immiscible phases, where one phase is dispersed in another continuous phase[36]. A major class of colloidal systems, besides foams (gas dispersed in liquid) and dispersions (solids dispersed in liquid)[37], are emulsions, which contain liquid phases that are immiscible. In food-related topics, systems containing semi-solid and solid phases are also referred to as emulsions[38]. Typically, emulsions are divided into two classifications: firstly, the oil-in-water (O/W) type where oil is dispersed in water (continuous phase) and secondly, the water-in-oil (W/O) type where water is dispersed in a continuous phase of oil (see Fig. 2.1 for a simple model). Most food emulsion systems are oil-in-water systems[39].

Multiple emulsions (O/W/O) or (W/O/W) are also possible, for example where the

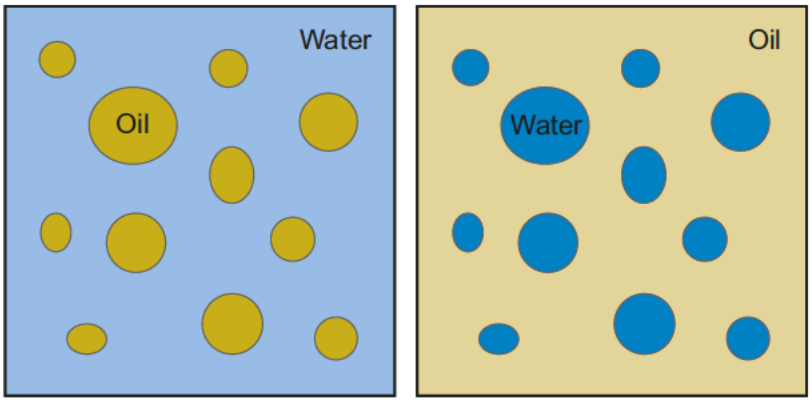

Figure 2.1: Simple models of common emulsions. On the left is the oil-in-water (O/W) type with oil dispersed in water, and on the right is a water-in-oil (W/O) type with water droplets in a continuous oil phase.

droplets themselves contain an 'inverse' emulsion. These types are of particular interest for texture enhancement or flavour release in food systems, as well as improved drug

release in pharmaceuticals[40]. Typical food emulsions are milk (products), mayonnaise, sauces, ice cream, margarine and (meat) spreads and sausages[39]. To form an emulsion, the two immiscible liquids must be homogenised. Typically, homogenisation is achieved by applying a high amount of energy (e.g. in the form of shear forces), resulting in a more or less stable emulsion. In the case of food emulsions, a distinction must be made between thermodynamic stability and kinetic stability. Emulsions are thermodynamically unstable systems and it is the kinetic stability that determines how long it takes the phases to separate again. Emulsion stability depends on the interfacial tension γ between the liquids and the *Laplace pressure*. When the interfacial tension is high, the pressure difference between the inside and outside of a droplet increases, as described by the *Young-Laplace equation* 2.1. It describes the relationship between the interfacial tension and the radius of a droplet.

$$\Delta P = \frac{2\gamma}{r} \tag{2.1}$$

A high Laplace pressure can be reduced either by reducing the interfacial tension γ or by increasing the radius r of the droplets. Reducing the interfacial tension with emulsifiers stabilises the particles and therefore the emulsion. Increasing the radius destabilises the emulsion and changes the physical properties[41].

Destabilising mechanisms

Several destabilising mechanisms are known and described in the literature[38] and an overview of the five main mechanisms is shown in Fig. 2.2.

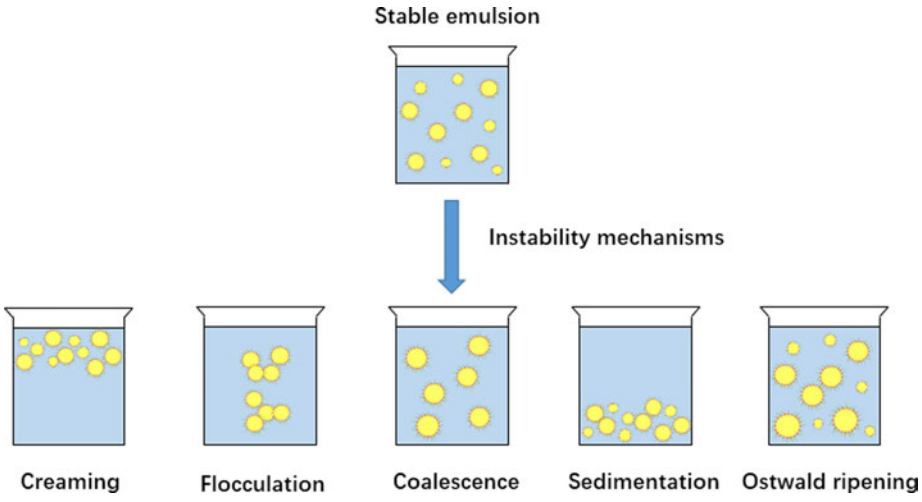

FIGURE 2.2: Different mechanisms leading to demixing of the emulsion. From left to right: creaming, flocculation, coalescence, sedimentation and Ostwald ripening. Reprinted from Shao et al. [41] with permission from Elsevier.

Flocculation Flocculation is described as the loose association of two or more droplets in an emulsion. This process can be reversible if the interaction of the

particles is weak. To form larger conglomerates, the particles must come into contact with each other, and the flocculation rate $\frac{dn_T}{dt}$ can be described with equation 2.2. The rate depends on the collision frequency F and collision efficiency E[42].

$$\frac{dn_T}{dt} = -\frac{1}{2}FE \tag{2.2}$$

The collision frequency depends on particle size and density, as well as the viscosity of the continuous phase. Collision efficiency is mostly determined by attractive forces, which are driven by numerous interactions such as steric, van der Waals and electrostatic interactions. For example, if the electrostatic repulsion from charged particles is reduced by increasing ionic strength of the continuous phase the attracting forces overcome a critical point (*CFC - critical flocculation concentration*) the droplets start to aggregate[41–43]. While other mechanisms have mostly a negative influence on the properties of an emulsion, a well-adjusted amount of flocculation can benefit the structure of food emulsion.

Gravitational mechanisms In addition to Brownian motion, other effects such as gravitational mechanisms lead to flocculation. Creaming and sedimentation are gravitational mechanisms that occur when there is a difference in the density ρ_2 of the dispersed phase and continuous phase ρ_1. In creaming, the dispersed phase has a lower density and starts to float on the continuous phase. Sedimentation is the opposite case where the density of the dispersed phase is higher than the density of the continuous phase. The physics behind these mechanisms is described by the *Stokes-law* in equation 2.3. To obtain the velocity v_{stokes} of a particle in an emulsion the stokes law connects two force terms. The first one (2.4) describes the gravitational force on a particle in a surrounding liquid depending on its densities ρ and radius r and the second (2.5) the hydrodynamic friction of the movement depending on the shear viscosity η_1 of the continuous phase.

$$v_{\text{stokes}} = -\frac{2gr^2(\rho_2 - \rho_1)}{9\eta_1} \tag{2.3}$$

$$F_g = -\frac{4}{3}\pi r^3(\rho_2 - \rho_1)g \tag{2.4}$$

$$F_f = 6\pi\eta_1 rv \tag{2.5}$$

A positive or negative velocity determines whether creaming or sedimentation occurs, and the velocity itself is a measure of emulsion stability. A v_{stokes} below 0.5 mm/d is technological considered to be stable[42].

Merging mechanisms There are two mechanisms by which the dispersed particles themselves can break up and form larger droplets or even separate completely into two phases. The first is Ostwald ripening, which is the effect of larger particles growing at the expense of smaller ones to reduce the high curvature effect and surface tension of small particles[41, 44]. To some extent, molecules from the dispersed phase are dissolved

in the continuous phase. The concentration around a particle depends on its radius because as the Laplace pressure increases, so does the solubility. The concentration gradient between small and large particles induces diffusion of molecules. This leads to a transfer of the dispersed substance from smaller to larger particles without the need for close contact. The equation 2.6 derived from the *Lifshitz-Slyozov-Wagner (LSW)* theory can give a prediction of the increase in particle size because the volume difference $(r^3 - r_0^3)$ of a particle with a radius r at time t and a radius r_0 at time $t = 0$ is proportional to solubility of the bulk phase S_∞ and the diffusion coefficient D at time t.

$$r^3 - r_0^3 = \frac{8\gamma V_m}{9RT} D S_\infty t \tag{2.6}$$

Therefore the interfacial tension γ, the molar volume V_m and temperature T must be known and R is the gas constant[42, 45].
The second mechanism is coalescence and describes the merging of all particles into larger droplets and is the most important mechanism on the way to thermodynamic stability of separated phases and is mostly driven by the Laplace-pressure in equation 2.1. The particles must be in close contact with each other for the separating film to break and the droplets to coalesce into a larger droplet. When the particles are in close contact, they deform slightly and the separating film (e.g. from the continuous phase or from the emulsifiers) ruptures randomly due to thermal motion. A prediction of the mean droplet diameter d at time t as influenced by coalescence is given by the equation 2.7. The evolution of the droplet size is determined by the number of nearest neighbours Z and the frequency of film breakage f which together define the rate of coalescence with the initial diameter d_0 at a time $t = 0$.

$$\frac{1}{d^2} = \frac{1}{d_0^2} - \frac{Z}{3} f t \tag{2.7}$$

The dependence is written as the reciprocal of the square of the diameter, but since $\frac{1}{d_0^2}$ decreases with time t, d^2 and therefore d increases. In a stable emulsion, the particles are usually well separated and coalescence usually follows one of the previously described mechanisms because they drastically reduce the distance between the emulsion particles[42, 46]. Each process can be described in isolation, but in real systems these effects are usually combined and interact. The stability of emulsions can be tuned by using appropriate emulsifiers to reduce the interfacial tension of the particles, increase stearic hindrance or increase the electrostatic repulsion of the emulsion particles[38, 39, 41].

2.1.2 Emulsifiers

Emulsifiers are amphiphile substances which belong to the class of surfactants. These Molecules are surface-active and able to absorb to the oil-water-interface and reduce the surface tension. These small molecules tend to have two parts, where one is a

hydrophilic 'head' group and a more lipophilic 'tail' group[39, 42]. With these properties, they can arrange themselves at the interface of water and oil in (food) emulsion. Structurally, emulsifiers in food systems range from small molecule surfactants such as phospholipids, mono- and diglycerides of fatty acids, sugar esters, salts of long chain fatty acids to long chain proteins such as casein, whey or liver proteins or polysaccharides (e.g. gum arabic). Particles can be used to stabilize emulsions as well and these emulsions are called pickering-emulsions[39, 47]. Fig. 2.3 shows a schematic of different emulsifiers on an oil droplet. Many emulsifiers are derived from fats or

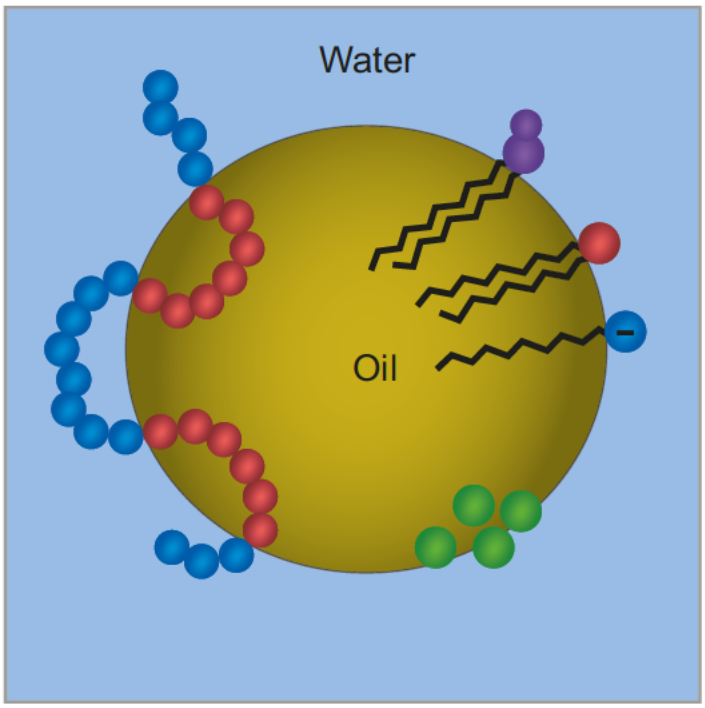

FIGURE 2.3: Schematic of different emulsifiers on an oil droplet. The red and blue chain resembles a protein, phospholipids have purple heads, mono- and diglycerides are shown in red and charged fatty acid salts are shown in blue. Green spheres represent emulsifying particles. Figure adapted and redrawn fromVilgis [39].

fatty acids. The long chain carbon backbone forms the lipophilic 'tail' of the emulsifier and the glycerol backbone with attached groups acts as the hydrophilic head.
A semi-empirical scale is used to evaluate the functionality of emulsifiers. The *hydrophilic-lipophilic balance* (HLB) can predict which type of emulsion will be stabilised by a particular emulsifier. Two empirical equations are used in different cases. The equation 2.8 (by Griffin) is used for non-ionic emulsifiers and uses the fraction of the molar mass of the hydrophilic part M_h and the total molar mass M multiplied by 20 to give the HLB value[39, 48].

$$HLB = 20 * \frac{M_h}{M} \tag{2.8}$$

$$HLB = 7 + \sum n_h(i) - \sum n_l(j) \tag{2.9}$$

The second equation 2.9 (Davis) takes the different chemical groups of the molecular structure of an emulsifier into account to calculate the HLB values. Therefore, empirical values, called hydrophilic group numbers n_h respectively lipophilic group numbers n_l for common chemical groups are estimated. The HLB value for an emulsifier is then calculated by adding the hydrophilic part (sum of n_h for each hydrophilic group i) to 7 and subtracting the lipophilic part (sum of n_l for each lipofilic group j). An overview of HLB values for common emulsifiers and group numbers is given in the Table 2.1. Typical chemical groups and their hydrophilic or lipophilic group number values are listed in 2.2. The HLB value ranges from 0 to 20 and could be divided into HLB <10, which predicts a more lipophilic character and the emulsifier tends to form W/O emulsions. Whereas an HLB >10 predicts a hydrophilic character of the emulsifier and O/W emulsions are more likely[49].

TABLE 2.1: Examples of common emulsifers and their corresponding HLP-values with abbrevations and typical applications[39, 42, 49, 50].

Emulsifier	**HLB-values**	**abbrevation**	**application**
Phospholipids	6-10	PL	fat spreads
Lecithin	2-8	-	chocolate
Mono- and diglycerides	2-5	MDG	bread, ice cream
Sodium stearate	16 - 18	-	abherent for powders
Lactic acid ester of MG	7-8	LACTEM	baked products whips
Citric acid ester of MG	11	CITREM	meat spreads, sauces
Polyglycerol ester of MG	5-7	PGE	icings, and fillings
Sodium stearyl lactylat	10-15	SSL	coffee whiteners, fat emulsions
Sucrose ester of fatty acids	6-15	-	sauces, sausages
Polysobate 60	15	PS60	forced fat crystallization

As this is an empirical method for assessing the emulsifying ability of a substance, there are some limitations and restrictions. Very low and very high HLB values may not accumulate on the droplet surface due to low surface activity. In many cases, an HLB value of around 10 indicates an unstable emulsion if the continuous and dispersed oil phases cannot compensate for this in terms of ionic strength, pH, fatty acid composition and molecular mobility at a given temperature[39, 42].

The viscosity of the continuous phase plays an important role in emulsion stability; higher viscosity produces a more stable emulsion and can be increased by thickeners such as xanthan gum, guar gum or carrageenans, but they do not have the same functionality as emulsifiers. However, they are often used in combination[39].

Classification of emulsifiers

The different types of emulsifiers can be classified in different ways depending on their molecular structure, size and functionality. Typically, they are categorised by the charge of the functional group into non-ionic and ionic emulsifiers. The group of ionic emulsifiers can be further divided into cationic, anionic and zwitterionic emulsifiers. Another common way of distinguishing emulsifiers is by size in low molecular weight surfactants and macromolecular emulsifiers such as biopolymers, or depending on their

Table 2.2: Examples of common group numbers for hydrophilic and lipophilic groups[42, 49].

hydrophyilic group number n_h		**lipophilic group number n_l**	
group	value	group	value
$-SO_4{}^{2-}2\,Na^+$	38.7	$-CH-$	0.475
$-COO^-Na^+$	21.1	$-CH_2-$	0.475
Tertiary amine	9.4	$-CH_3$	0.475
Sorbitan ester	6.8	$-CH=$	0.475
glycerol ester	5.25	$-(CH_2)_4-O-$	0.15
$-COOH$	2.1	-	-
$-OH$	1.9	-	-
$-O-$	1.3	-	-

origin in natural or synthetic emulsifiers.
A classification by charge is the most convenient and helps to understand aspects of their physical behaviour, as the charge plays a key role in interaction with other food componentens, such as proteins, salts and acids[48].

Nonionic emulsifier The hydrophilic head groups of nonionic emulsifiers have no net charge and instead derive their functionality from neutral polar groups, most commonly hydroxyl ($-OH$) or ether ($-O-$) groups. However, their polar nature increases their solubility in water and their lack of charge makes them more resistant to changes in pH or ionic strength of the continuous phase. Their functionality depends mainly on steric hindrance and spatial repulsion[51]. Common examples of emulsifiers are polysorbates, e.g. PS60, sorbitan esters or mono- and diglycerides of fatty acids and their esters derived from acetic and lactic acid (ACETEM and LACTEM)[42].

Ionic emulsifier The class of ionic emulsifiers can be divided into three groups according to their charge: anionic, cationic and zwitterionic. The first group has a negative charge due to its charged head group. The origin of the charge is usually carboxyl groups (COOH), their salts ($-COO^-M^+$ M^+: metal cation) or sulphate groups ($-SO_4{}^{2-}2\,Na^+$). Natural sources of these anionic emulsifiers are fatty acids or mono- and diglycerides (MDGs). For example, sodium stearate is used as an emulsifier. More common are MDG esters formed with citric acid (CITREM) and diacetyl tartaric acid (DATEM). They have two or three carboxyl groups and after esterification one or two may dissociate during emulsion formation. Other examples of anionic surfactants are stearoyl lactylate salts (e.g. sodium or calcium) which are esters of the fatty acid stearate and lactic acid. Some phospholipids, such as phosphatidylinositol (PI) are also anionic. Anionic emulsifiers stabilise the emulsion by electrostatic repulsion on the droplet surface induced by the charge. However, their performance is highly dependent on pH and ionic strength, as a low pH or high salt concentration can reduce the electrostatic repulsion by charge screening[42, 51].
The opposite case, cationic emulsifiers, are rarely used in food. They are usually

derived from quaternary ammonium groups (NH_4^+ or NR_4^+) and laureoyl arginate is an example which is important for food or pharmaceutical applications. Other cationic emulsifiers are more commonly used in cosmetic or research applications, such as cetyltrimethylammonium bromide (CTAB) or its chloride analogue CTAC[42, 52]. Zwitterionic emulsifiers are a special case. The molecules have a net charge of zero, although their functional group contains a negative and a positive charge. Lecithin, an important class of natural emulsifiers, is a mixture of different phospholipids and other lipids and therefore has different properties from pure phospholipids as shown in the Table 2.1. Two of the three main derivatives, phosphatidylcholine (PC) and phosphatidylethanolamonine (PE), found in lecithin are zwitterionic. Due to their amphoteric properties, they are responsive to pH changes and combine some of the properties of ionic and non-ionic emulsifiers and are suitable for a range of systems[42, 51, 53].

Amphiphilic biopolymers Proteins and some hydrocolloids are often used to stabilise emulsions because of their ability to adsorb at the oil-water interface and their properties such as solubility, surface activity, thickening and gelling depend on molecular characteristics (molecular weight, conformation, flexibility, polarity and hydrophobicity). The emulsification stabilising properties of proteins are determined by the interactions of the amino acids linked together to form the primary structure of the proteins. A unique feature of proteins is their ability to fold into 3D structures depending on their primary structure[54]. Both folded and unfolded structures result in specific hydrophilic and lipophilic regions that can be positioned at the oil-water interface, as shown in Fig. 2.4. Proteins are sensitive to changes in pH as they tend to flocculate around the isoelectric point. If the emulsion is formed by folded proteins, the emulsion will be sensitive to increases in temperature as the proteins unfold and increase attractive interactions[42, 55]. Typical proteins that act as emulsifiers are caseins and whey from milk, muscle proteins (myosin and actin), collagen/gelatin, liver, egg and sarcoplasmic proteins and plant proteins from soya, peas and rice[5, 42, 56]. Hydrocolloids have a polysaccharide backbone which is hydrophilic and the emulsifying capacity is introduced by hydrophobic groups such as alkanes (modified starches and cellulose) or an attached protein component (e.g. gum arabic or pectin). Without these modifications, hydrocolloids act more like gelling or thickening agents. A special case is collagen, a protein with a highly hydrophilic character, which has some emulsifying properties but acts more as a gelling and stabilising agent[55, 57].

Pickering emulsions Pickering emulsions are a type of emulsion stabilised by hard particles arranged at the oil-water interface and the particle can be from organic or inorganic nature (see Fig. 2.5). The ability of a particle to stabilise emulsions depends on the surface tension γ, the interfacial contact angle Θ_{ow} and the particle radius r, and the stabilising energy ΔE is calculated by the equation 2.10. However, particles with hydrophobic and hydrophilic parts or anisotropic shapes (e.g. rods) are more

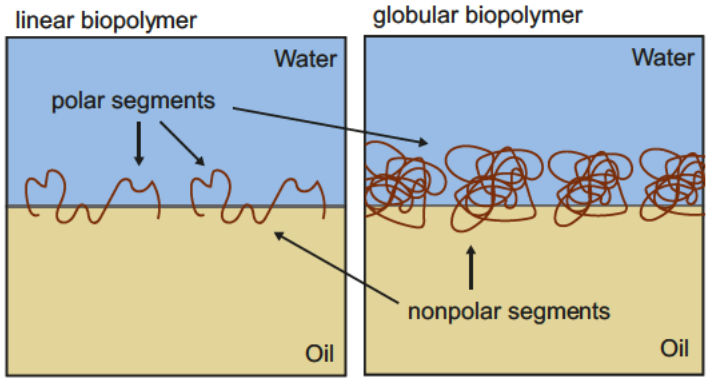

FIGURE 2.4: Model of linear biopolymers (left) and globular biopolymers (right). The figure shows the interaction of the biopolymers with their polar and non-polar regions at the oil-water interface. Figure adapted and redrawn from McClements [42].

efficient at forming an emulsion[58, 59].

$$\Delta E = \pi r^2 \gamma (1 \pm \cos \Theta_{ow})^2 \tag{2.10}$$

The equation is valid if the particles are much smaller than the curvature of the droplet and an optimum contact angle would be Θ =90°. Smaller or larger contact angles would favour oil-in-water or water-in-oil emulsions[58]. In addition to many other applications such as drug delivery, paints, personal care and agricultural products, some food products are stabilised by Pickering emulsions. Typical food Pickering emulsions

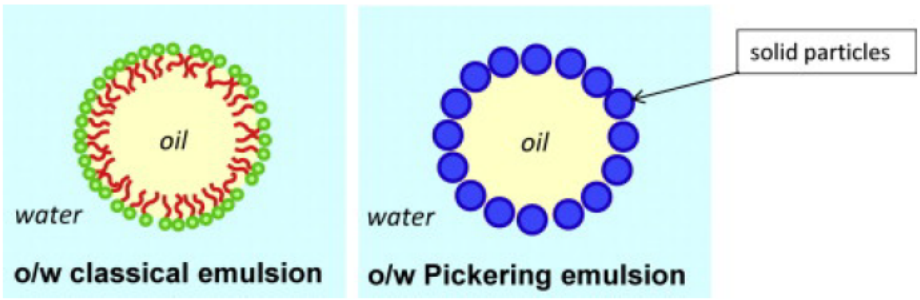

FIGURE 2.5: Model figure of a classical emulsion with emulsifiers (left) and a Pickering emulsions with solid particles at the interface (right). Figure reprinted from Chevalier and Bolzinger [60] with permission from Elsevier.

are milk stabilisation with casein micelles, O/W emulsions with microcrystalline starch or fat particles in whipped cream[39, 58, 61].

2.1.3 Fats and oils

Fats and oils play an important role in food and nutrition. Some foods are dominated by fats, such as sausages, cheese, butter and margarines, chocolate and nougat. Oils and fats consist of a distribution of non-polar triglycerides, which are composed of three fatty acids covalently bonded to a glycerol backbone (See Fig. 2.6). Fatty acids

are organic compounds with an alkane chain and a carboxyl group (up to 24 C atoms) at the end. If the C atoms are single bonded to their neighbours, it is a saturated fatty acid and if there are some alkene groups (−CH=CH−) they are unsaturated fatty acids. A common way of abbreviating the names is to indicate the number of carbon atoms and the degree of saturation, for example the monounsaturated oleic acid C18:1 shown in Fig. 2.6. Usually, the alkene group has a *cis*-configuration and the fatty acids lose their straight-chain behaviour[54]. The position of these double bonds is usually determined by counting from the $-CH_3$ end group ω and the typical positions $\omega 3$, $\omega 6$ *and* $\omega 9$ are set by the biosynthetic pathway. Most natural fatty acids have an even number of carbon atoms, but milk contains small amounts of fatty acids with an odd number of carbon atoms[39, 62]. The triglycerides in natural fats and oils have a

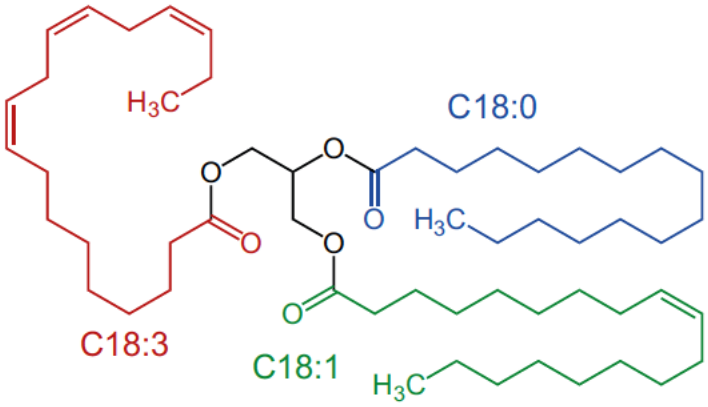

FIGURE 2.6: Molecular skeletal formula of a triglyceride with different fatty acids. A saturated fatty acid (C18:0 - stearic acid) is shown in blue, an unsaturated fatty acid (C18:1 - oleic acid) is shown in green and a poly unsaturated fatty acid (C18:3 - alpha-linolenic acid) is shown in red. Adapted from: Jü, CC0, via Wikimedia Commons[63].

distribution of different fatty acids attached to the glycerol, which determines their melting properties and therefore their physical appearance as liquid oil or solid fat. Every fat has a certain amount of liquid phase, which influences physical properties such as hardness and spreadability. Solid fat content is usually estimated by solid-state NMR[35, 39, 62, 64].

Crystallization of triglycerides

The crystallisation melting behaviour of a triglyceride depends on the fatty acid distribution because this, together with the cooling rate, influences the crystal structure. A model fat consistent of tristearin (C18:0) has three different crystal structures depending on the cooling rate. At high cooling rates the hexagonal α-structure is formed and has the lowest melting temperature of 54 °C, whereas at slow cooling rates the stable β-structure is formed. The triglycerides are now tilted in the plane to form a triclinic lattice. Compared to the α structure, the melting point increases up to 74 °C. A third structure is the β' configuration which crystallises in a hexagonal lattice and has a melting point of 63.5 °C [39, 65]. The influence of fatty acids is shown in a

TABLE 2.3: Melting temperature for different triglyceride combinations of stearic acid (S) C18:0 and palmitic acid (P) C16:0[66]

Triglyceride	SSS	PSP	SPS	SSP	PPP	PPS
Melting point/°C	72.0	68.2	67.7	66.2	66.0	63.5

second model system where the melting points of different mixtures of triglycerides with stearic acid (C18:0) and palmitic acid (C16:0) were determined.

The melting points decrease with shorter chain lengths as well as with the position of the fatty acid. The influence of the rearrangement of the positions is high and can prevent the formation of mixed crystals[39, 66].
Introducing unsaturated fatty acid such as oleic acid increases the possible crystal structures even further. The triglyceride SOS (S stearic acid C18:0, O oleic acid C18:1) can crystallize in five different structures (α, γ, β', β_2, β_1) with a melting range of 23.5 °C to 43.0 °C[65]

Fat crystal networks

In natural oils and fats, the number of different fatty acids and unsaturated fatty acids is higher than in these model systems, and when they crystallise, the oil, consisting of short-chain fatty acids and poly-unsaturated fatty acids, is freely distributed between the spherical crystals. The crystals are formed by layers of triglycerides forming single crystallites. These form the primary spherical particles as shown in the lower part of Fig. 2.7. These primary particles are connected to each other and from a network[39, 67].

These networks form larger blobs with a mean size ζ, which is the smallest size where

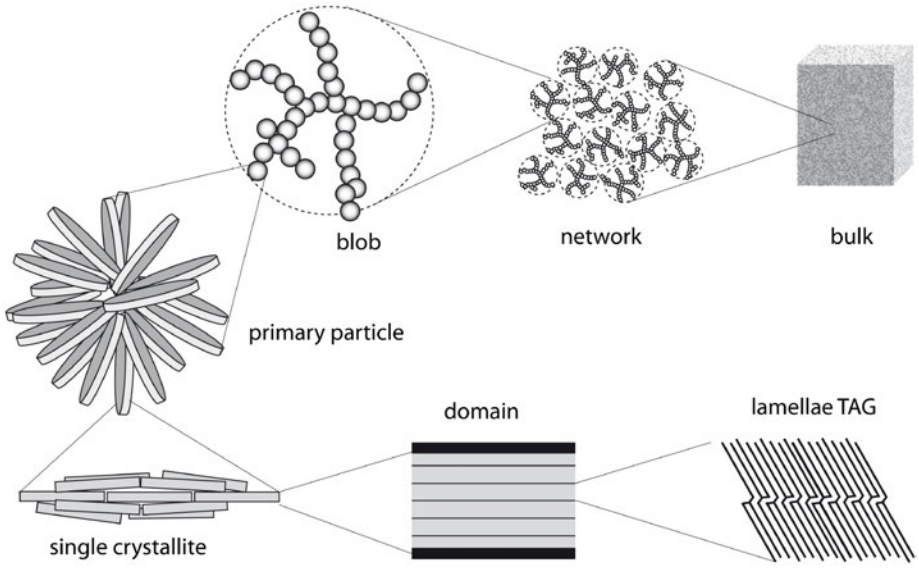

FIGURE 2.7: Fat crystal network at different length scales. Reprinted from Vilgis [39] with permission of IOP Publishing.

the network is fractal. This means that the number of particles n_b with a diameter b

scales with the fractal dimension d_f and therefore with the volume fraction ϕ as well as shown in the equations 2.11.

$$(\zeta/b)^{d_f} = cn_b \qquad \text{or} \qquad \zeta \propto \phi^{\frac{1}{d_f - d}} \tag{2.11}$$

Whereas d is the dimension of the system ($d = 3$ for spheres) and c is a proportionality constant[39, 68, 69].
In the bulk, these blobs themselves form a network, which is connected by the interactions of the primary particles, as can be seen in Fig. 2.7. For colloidal gels Shih et al. [69] derived a model showing the dependence of the modulus G and the limit of linear deformation γ_0 depending on the volume fraction ϕ. Two dependencies have been derived depending on the interactions of the blobs. The first, shown in equation 2.12, is for the strong binding regime, which is the case for larger blobs, where the interaction between the primary particles is weaker than the interaction between the blobs. Therefore, the fractal dimension of the blobs d_f and of the backbone particles x and the dimension of the system $d = 3$ are considered.

$$G \propto \phi^{\frac{3+x}{3-d_f}} \quad and \quad \gamma_0 \propto \phi^{-\frac{1+x}{3-d_f}} \tag{2.12}$$

$$G \propto \phi^{\frac{1}{3-d_f}} \quad and \quad \gamma_0 \propto \phi^{\frac{1}{3-d_f}} \tag{2.13}$$

In the second case, shown in equation 2.13, the particles are assumed to be small and rigid, and therefore the interactions between the blobs are weaker than those between the primary particles. In this case, the exponents of ϕ depend only on the fractal dimension of the blob network[68–70]. These models are further refined to better fit experimental data or to fit fat crystal networks. In this case there is an oil phase between the blobs and the fat crystals resemble the primary particles (see figure 2.7)[39, 68, 70].
Tang and Marangoni [68] derived an equation to predict the storage modulus G of fat crystal networks as a function of shear γ and volume fraction ϕ of the solid part.

$$G = \frac{mA}{6c\pi a\zeta d_0^3}\phi^{\frac{1}{3-d_f}} \tag{2.14}$$

The *Hamaker* constant A defines the van der Waals body-body interaction of the system, while m is the coordination number of the blobs, with a size of ζ, c is the non-universial proportionality constant. The mean distance is d_0 and the mean size of the primary particle is b when they are linked, and the number of particles in a blob is n_b.
Beside the equation 2.14 Tang and Marangoni [68] derived an equation to determine the yield stress Σ^* which needs to be applied to a fat crystal structure to break irreversible. The yield stress is calculated with equation 2.15 in dependency of the interface tension

σ and the volume fraction ϕ of the network.

$$\Sigma^* \frac{6\sigma}{b} \phi^{\frac{1}{3-d_f}} \tag{2.15}$$

The parameter b is the diameter of the primary fat crystals and d_f is the fractal dimension of the network as in the equation 2.11.
These networks of crystalline fat particles play an important role in the rheological behaviour. At low amplitudes the networks remain intact and the solid part determines the modulus. As the shear deformations increase, the links of the blobs break and the modulus decreases, and at higher deformation rates the links within the blob break and the system becomes liquid[39, 67, 68].

2.1.4 Enzymes

Enzymes are a specific class of proteins that have high catalytic activity with high specificity. When a substrate interacts with an enzyme active site, a reaction is catalysed to form the product. Enzymes increase the rate of reaction by lowering the activation barrier of the specific reaction they catalyse. Enzyme kinetics are often described by the Michaelis-Menten equation, which describes the rate of conversion v_0 of a substrate to a product as a function of substrate concentration $[S]$[54, 62].

$$v_0 = v_{max} \frac{[S]}{[S] + K_M} \tag{2.16}$$

In the equation 2.16 v_{max} is the maximum conversation rate of an enzyme when all active sites are saturated with substrate. The Michaelis-Menten constant K_M describes the interaction between the substrate and the enzyme and is independent of their concentrations.
Many enzymes require cofactors, which are small molecules (called coenzymes) or metals, to catalyse a particular reaction. They can be covalently bound to the enzyme. Conversely, some molecules can block enzyme activity by binding to the active side of the enzyme (competitive inhibitor) and blocking it, binding to the enzyme-substrate complex (non-competitive inhibitor) and deactivating the enzyme, or binding to another side of the enzyme (non-competitive inhibitor) and reducing the activity of the enzyme[54, 62].

Types of enzymes

Enzymes are categorised into seven different groups according to their function. These categories are further subdivided to refine the nomenclature, which gives each enzyme a unique four-digit code derived from its specific function. For example, lipase is classified as EC 3.1.1.3[71]. The main groups of enzymes are: oxidoreductases (EC 1, cataluse oxidation/reduction reactions), transferases (EC 2, transfer a functional group), hydrolases (EC 3, catalyze hydrolysis reactions), lyases (EC 4, cleave bonds), isomerases (EC 5, changes within a molecule), ligases (EC 6, join two molecules with

colvalent bond) and translocases (EC 7, movements of ions across membranes). The further divition is based on substrate, products or chemical mechanisms[72].

Lipases

Lipase is a specific enzyme capable of hydrolysing the ester bond to cleave fatty acids from triglycerols to give diglycerides, monoglycerides and glycerol. The reaction takes place at the interface between an aqueous phase and the substrate phase, which is usually oil or fat. Lipases are also capable of catalysing the reverse reaction, esterification, and attaching an acid to a $-OH$ group of glycerol, but only in the absence of water. Lipases are monomeric proteins with a molecular weight between 19 kDa and 60 kDa. They are stable over a range of pH values from pH 4 to pH 8 and there are two main groups that cleave either all positions of fatty acids or only positions 1 and 3. The kinetics of lipases cannot be described by the Michaelis-Menten equation (2.16), because interfacial adsorption and substrate binding is a two-step equilibrium process[73]. However, it can be used to approximate the reaction rate of lipases used in experiments[74]. Lipases have many applications in general, they

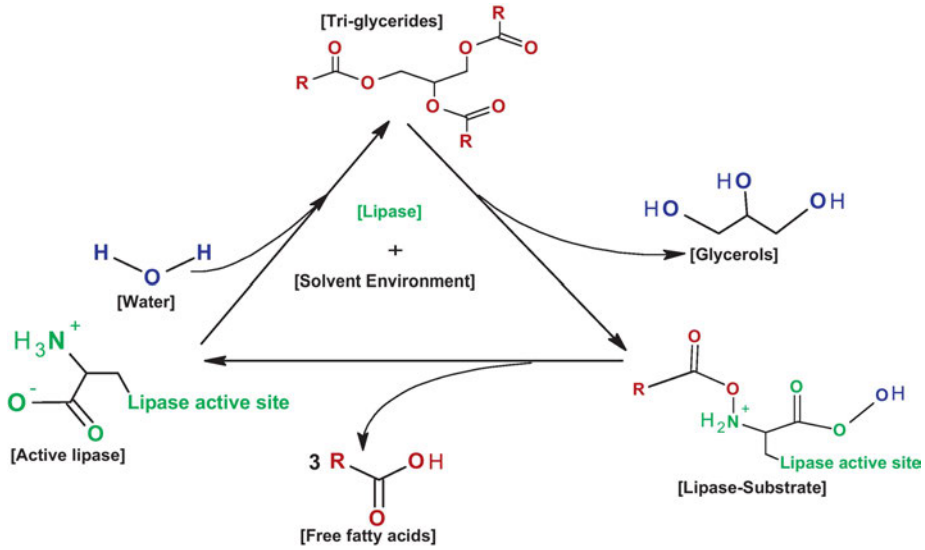

FIGURE 2.8: The schematic illustration shows the catalysis cycle of lipases. Reprinted from Sharma et al. [74] with permission from Elsevier.

are used in detergents, to aid enantioselective synthesis of pharmaceuticals, protein engineering, biodiesel production and in various cases in the food industry. It is used in dairy products to modify the fatty acid chain length and to enhance the flavour of cheese. Structured oils and fats are produced by esterification and interesterification of fatty acids with lipase to obtain cocoa butter analogues from cheaper fats and to increase the oleic acid content of soybean oil by replacing unfavourable fatty acids. The same reactions are used to introduce short-chain fatty acids into oils and fats to reduce calorie content. Spreadable and plastic fats have been produced by partial hydrolysis of the fatty acids[73, 75].

2.2 Methods

2.2.1 Rheologie

Rheology is an important method for investigating the flow behaviour of dispersed materials such as paints, varnishes, coatings, polymers, cosmetic and pharmaceutical products, emulsions and food systems. Almost all types of liquid and semi-solid food products can be characterised using rheological techniques[76, 77].

2.2.2 Rheology basics

The rheological behaviour of most materials lies between two extremes, on the one hand we have Newtonian viscous fluids and on the other ideal Hookian solids. Thus, most materials exhibit partial behaviour of both and therefore have visoelastic properties.

$$\sigma = \eta\dot{\gamma} \tag{2.17}$$

$$\sigma = G\gamma \tag{2.18}$$

Viscosity is the constant η which is proportional to the shear stress $\sigma = F/A$ required to achieve steady flow at a given shear rate $\dot{\gamma} = v/h$, which is a velocity gradient perpendicular to the direction of flow. Dispersed materials often behave differently from the ideal Newtonian case in the equation 2.17 and the viscosity increases or decreases with increasing shear rates, showing dilatant or shear thinning behaviour. To account for the time dependence, the decrease in viscosity at constant shear rate and partial recovery of structure by removal of shear stress is called thixotropic behaviour. The opposite case of increasing viscosity at constant shear rate is called rheopexy[77]. The other case is an ideal Hookian solid, where the shear stress σ is related to the shear strain γ by the shear modulus G, as shown in the equation 2.18. As many food systems have viscoelastic properties, dynamic testing is becoming a standard method for investigating viscoelastic properties. A sinusoidal strain is applied to the sample and the stress is measured. The applied strain γ is time dependent on its maximum amplitude γ_0 and angular frequency ω (see equation 2.19) and therefore the measured stress τ is also time and frequency dependent.

$$\gamma = \gamma_0 \cos(\omega t) \tag{2.19}$$

$$\tau = \tau_0 \cos(\omega t + \delta) \tag{2.20}$$

However, the material-dependent relaxation mechanism causes a phase shift δ of the stress, as seen in the equation 2.20. The dynamic shear moduls G can be expressed in its complex form 2.21

$$G = G' + iG'' \tag{2.21}$$

Where G' is the storage modulus (or elastic modulus), which is a measure of the energy stored by the elastic part, and G'' is the loss modulus (or viscous modulus), which is the energy dissipated due to the viscous behaviour of the sample. Both can be expressed as a function of the phase shift as given by the equations 2.22 and 2.23.

$$G' = \frac{\sigma_0}{\gamma_0} \cos \delta \tag{2.22}$$

$$G'' = \frac{\sigma_0}{\gamma_0} \sin \delta \tag{2.23}$$

The strain applied in these types of tests should be small so that the material is in the *linear viscoelastic regime* (LVR) because in this regime strain and stress are proportional and the structure is not deformed irreversible[42, 77].

Linear rheology

Linear or rotational rheology is used to characterise most complex viscous fluids at a given shear rate. Such a controlled shear rate test can calculate the viscosity with the measured torque and shear stress. Controlled shear stress tests estimate viscosity from measured shear rate and rotational speed[76, 77].

Oscillatory rheology

Oscillatory rheology is suitable for investigating viscoelastic systems such as polymer melts, dispersions, pastes, gels or elastomers. It can therefore be used to characterise semi-solid food systems as different tests can be applied[76].

Amplitude sweeps Amplitude sweeps allow the sample to be characterised by increasing shear amplitude and the shear stress is measured. Frequency and temperature are kept constant throughout the measurements. From the measurements the storage modulus G' and the loss modulus G'' can be obtained as a function of shear strain. Usually the measurements are made with a parallel plate geometry as shown in Fig. 2.9 A[78]. From a typical measurement, as shown in Fig. 2.9 B, several pieces of information can be obtained. An impression of the overall stiffness of the sample is given by the initial modulus G'_0 at $\gamma = 0\,\%$. The plateau where the modulus remains constant is the linear viscoelastic regime and in this region the stress and strain are proportional and the sample deformation remains reversible. As γ_L, the yield point marks the end of the LVR and indicates the beginning of the sample's structural decomposition[78].
In general, the nature of the sample can be determined by the values of G' and G''. If $G' > G''$ the sample has a gel character and the elastic properties are dominant. This applies to solids, rubbers, gels and stable dispersions.
In the opposite case, $G'' > G'$, the sample has a liquid character and the viscous properties are more pronounced than the elastic properties and the sample is even liquid in the LVR range. This behaviour is typical of gases, liquids, polymer solutions

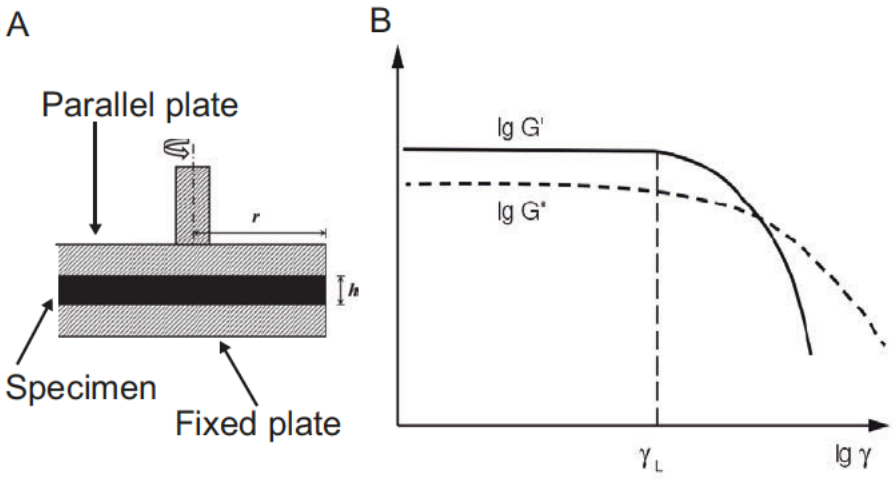

FIGURE 2.9: A: Model figure of a parallel plate geometry with specimen. The radius of the plate is r and the height of the specimen is h. Adapted from Li et al. [79]. B: A typical graph of an amplitude measurement with modulus G'' and G' and strain γ. γ_L marks the end of the linear viscoelastic regime. Adapted from Mezger [76].

and unlinked high viscosity polymers (e.g. PDMS)[77].
At the flow point ($G' = G''$) the viscous modulus begins to exceed the elastic modulus, indicating that the sample is beginning to flow. In most cases for viscoelastic samples this means that the structure is irreversibly deformed[76].

Temperature sweeps Temperature sweeps or ramps are performed to evaluate viscoelastic properties as a function of temperature. The sample is therefore measured at a constant amplitude and frequency at a specific temperature rate or profile. Usually the amplitude is chosen to be in the LVR. The values G' and G'' are plotted against temperature. This can be used to investigate the stability of emulsions against heat, the gelling properties of hydrocolloids or the freeze-thaw cycles of various products[76].

2.2.3 Texture profile analysis

Food texture is largely influenced by the gelling properties of hydrocolloids and proteins, and the structure of the fat. These food systems undergo massive deformation during chewing and therefore the mechanical properties are crucial for a good textural experience during oral processing. In order to gain insight into the textural properties, compression tests, called texture profile analysis (TPA), have been carried out to obtain various parameters such as hardness, elasticity, cohesiveness and adhesiveness. Such tests are performed with a (usually) cylindrical specimen that is compressed or penetrated with a probe of a defined geometry using a texturometer or other force measuring device[80, 81]. The measured force is a function of the contact area A and the applied stress σ, as shown in the equation 2.24.

$$F = \sigma A = \sigma\pi(\frac{d}{2})^2 \tag{2.24}$$

The area depends on the diameter of either the probe or the round shape of the sample, whichever is smaller. A typical texture analyser measurement is a two stage compression of around 75 % of the sample and therefore also called 'two-bite-test'[80, 82]. Figure 2.10 shows a graph of the force against the time of measurement and

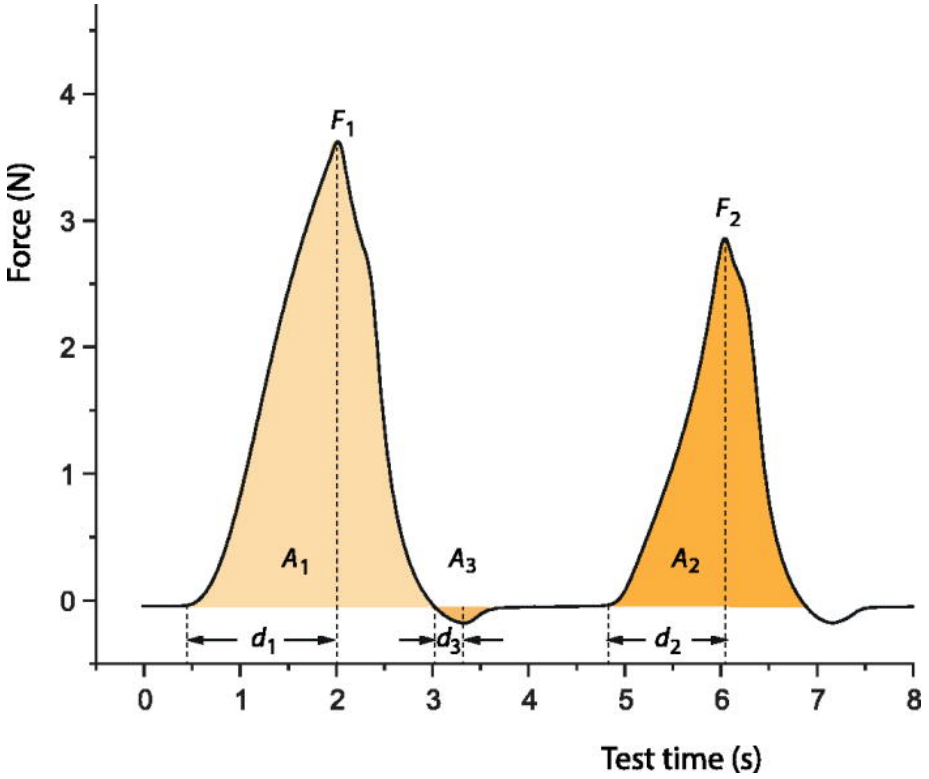

FIGURE 2.10: The measured force of a TPA measurement is plotted against time. The graph shows the two 'bites' with the two maxima. Reprinted from Toultchinski and Vilgis [83] under Creative Common BY license.

from this force profile the various parameters can be derived. Hardness (HDN) is the maximum force of the first 'bite' F_1, which defines the force required to achieve a predefined deformation. Adhesion (ADH) is the work required to overcome the adhesive forces between the sample and the probe, corresponding to the area of A_3. Cohesiveness (COH) is the ratio of the areas of the two maxima A_2 and A_1 and is a measure of the strength of the internal bond. Springiness (SPG) is the rate at which a sample returns to its original shape and is defined as d_2/d_1. Gumminess (GUM) defines the energy required to break the semi-solid food structure and is the product of hardness and cohesiveness. For solid food structures, chewiness (CHW) is defined as HDN $\cdot$ COH $\cdot$ SPG. Stickiness is used when a material sticks to the surface of the probe and is defined as the ratio of d_3/d_1. An overview is given in Table 2.4. All the characteristics, except adhesiveness, can be related to the forces of attraction between the molecules that make up the network of the food sample. Adhesion is related to the surface properties of the sample[83].

TABLE 2.4: Overview off TPA parameters and their location in a texture profile as shown in Fig. 2.10. Adapted from Toultchinski and Vilgis [83] and Trinh and Glasgow [84].

TPA parameter	Definition	Location in TPA
Hardness (HDN)	Force required for defomation	F_1
Adhesiveness (ADH)	work required to sticky forces	A_3
Cohesiveness (COH)	Strength of internal bonds	A_2/A_1
Springiness (SPG)	rate of sample shape recovery	d_2/d_1
Chewiness (CHW)	Energy needed to chew solid food	HDN · COH · SPG
Gumminess (GUM)	Energy needed to chew semi-solid food	HDN · COH

2.2.4 Differential scanning calorimetry

Differential Scanning Calorimetry (DSC) is a sensitive thermal analysis technique for measuring heat flow. Every reaction or transition of molecules releases or absorbs energy, which can be detected by DSC and leads to a wide range of applications. Examples include heat capacity determination, polymer and glass transition characterisation, kinetic studies, melting and crystallisation processes. In food research, DSC is used to study melting and crystallisation processes of fats, oils and gels. Gelling of hydrocolloids and denaturation of proteins can also be characterised[85, 86].
The principle of a heat flux DSC bases on the defined exchange of heat on a heat conductive path with given thermal resistance. The primary signal which is measured is the temperature difference ΔT between a reference cell and a sample cell. In Fig. 2.11 a disk type measurement cell is shown. The sample in the furnace is heated or

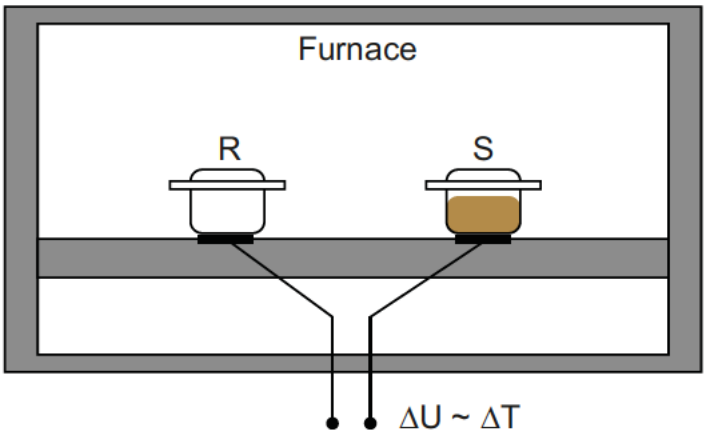

FIGURE 2.11: In the crucible of a heat flux DSC, a reference cell and a sample cell are placed on two thermocouples that measure the temperature difference between the reference and sample during heating/cooling. Adapted and redrawn from Drebushchak [87].

cooled at a specific rate. This creates a heat flow and the temperature of both cells is measured and the difference ΔT is estimated.

$$\Phi_{FS} - \Phi_{FR} \sim -\Delta \tag{2.25}$$

$$\Delta T = T_S - T_R \tag{2.26}$$

In an ideal symmetrical arrangement, the heat flows to the sample and reference cells are equal and therefore the differential temperature signal is zero. If a transition of the sample disturbs this steady state equilibrium, a signal is generated which is proportional to the heat flows as shown in equation 2.25 and 2.26.
This ideal arrangement is never reached in a real measurement and therefore the heat flow rate Φ_m is calculated with equation 2.27 with dependency of ΔT and a calibration factor k' and usually given in W/g.

$$\Phi_m = -k'\Delta T \tag{2.27}$$

The calibration factor is determined by a defined sample with known heat capacity[85]. Figure 2.12 shows an example graph of two fat samples. From the melting part (lower

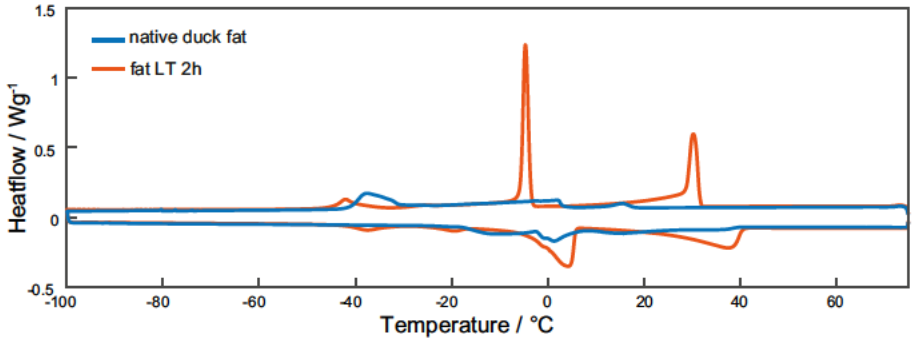

FIGURE 2.12: Example graph of DSC measurements of two different fat samples. The samples show exothermic crystallisation (upper part) and endothermic melting (lower part). Adapted from Baechle et al. [88]

part of the graphs) the different melting points can be determined. The peak area can be related to the enthalpy of fusion ΔH_{fus}. Therefore, the heat flow must be plotted as a function of time and the integration of the peak area gives the amount of heat. The enthalpy of fusion ΔH_{fus} is calculated by dividing the heat amount by the sample weight. The same can be applied to the crystallisation part[89].

2.2.5 Coherent anti-Stokes Raman Scattering Microscopy

Coherent anti-Stokes Raman scattering microscopy (CARS microscopy) is a technique based on molecular vibrational spectroscopy that can image biological samples in a label-free, non-invasive and real-time manner. It has high chemical selectivity due to the specific vibrational frequencies of molecules. It is a multi-photon technique that is widely used in biological, biomedical and food applications due to its ability to image proteins, lipids, DNA/RNA and polysaccharides. This is possible due to many Raman active groups in those molecules, such as the $-CH_2$ mode (at $2845\,cm^{-1}$) for lipids and proteins or the Amide group (with $1620\,cm^{-1}$) for proteins[90–92]. To generate the signal, two laser beams are required to interact with the sample in a wave mixing process. A probe beam with a tunable frequency ω_p and a Stokes beam with a fixed frequency ω_s. If the generated frequency $\omega_p - \omega_s$ matches the vibrational frequency

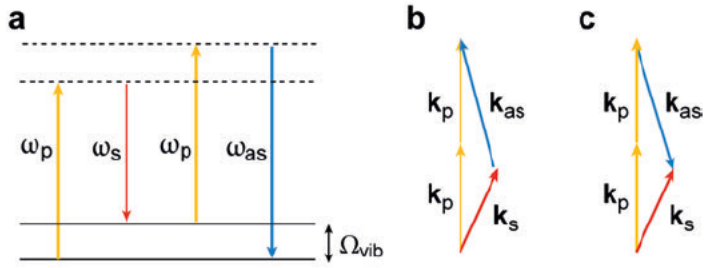

FIGURE 2.13: a: Diagram of the coherent anti-Stokes Raman scattering process. At the frequencies of the probe (ω_p) and the Stokes beam (ω_s), the antistokes signal $\omega_a s$ is generated when Ω_{vib} matches. b: Phase matching conditions of forward generated CARS. c: Phase matching conditions of the backward generated CARS. With the wavevectors k with the matching indices and is given as $k = \pi/\lambda$. Reprinted from Evans and Xie [90] with permission from Annual review.

Ω_{vib} of a Raman active molecule, the strong anti-Stokes signal is generated by the excitation field which coherently drives resonant osszilators as shown in Fig. 2.13 and equation 2.28[90].

$$\omega_{as} = 2\omega_p - \omega_s \tag{2.28}$$

The laser pulses polarise the electron cloud in the extinction volume and generate two fields, a non-resonant field depending on the pure electron motion and the oscillating field depending on the Raman mode. A signal is generated when the wave vectors k_s and k_p are in phase with the wave vector k_{as}[91].

$$\Delta k = k_{as} - (2k_p - k_s) \tag{2.29}$$

The wavevector mismatch Δk must be close to zero for phase matching conditions as shown in equation 2.14. The wavevector k_{as} has two possible directions, shown in Fig. 2.13 b and c, and therefore produces a forward detected and a backward (epi) detected signal[90]. This can be used to detect the signal through the sample (if thin enough) and, in epi-CARS mode, 'reflected' from the sample. A general schematic of a CARS microscopy setup is shown in Fig. 2.14 A. A vanadate laser (532 nm) is coupled into an optical parametric oscillator (OPO) which generates the two laser beams using an optical resonator and a nonlinear optical crystal. The laser beams are then coupled into the objective of the microscope with an XY scanner to image the sample pixel by pixel. A condenser, filter and detector are placed on the opposite side of the sample to detect the foreword CARS signal. The epi-CARS signal is collected by the objective and directed to the detector by a dichroic mirror through a filter[90]. Images are generated from the scan signal. Different modes are possible, such as z-stacks (different heights in the sample) or spectral stacks with different probe wavelengths. In Fig. 2.14 part B two example images are shown, the upper one shows the emulsion structure of a liver pâté with the fat particles in red and the aqueous phase in black. The lower image

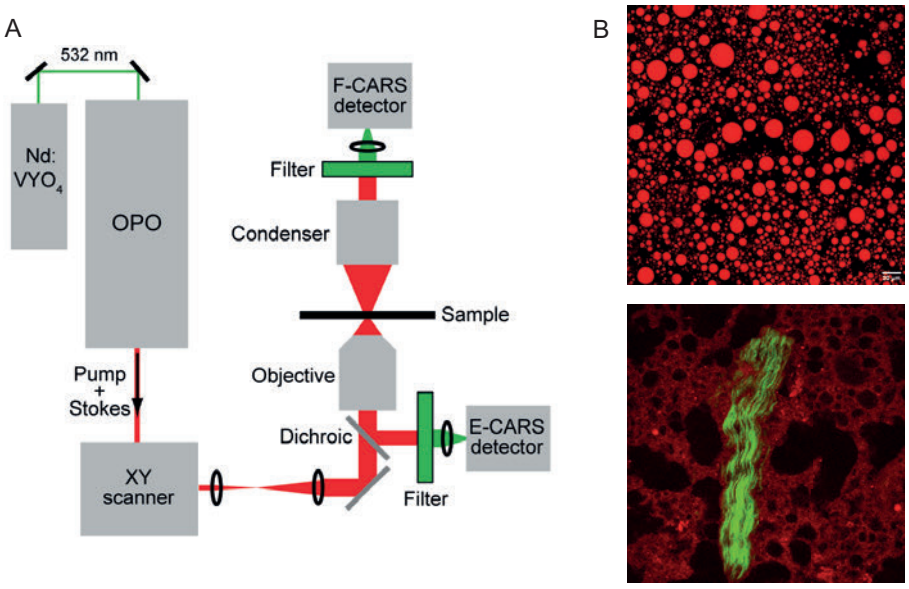

FIGURE 2.14: A: Schematic of a CARS microscope. Adapted from Evans and Xie [90] with permission from Annual Reviwe. B: Example images of a liver paté emulsion. In the top image, the fat particles are red and the aqueous phase is black. In the lower image the fat particles are black and the aqueous phase is red. A protein is shown in green. Pictures provided by Matias Via.

shows a collagen enriched liver pâté sample. However, due to a different wavelength of the probe laser, the fat particles are black, the aqueous phase is red and the collagen protein is green

2.2.6 Solid-state Nuclear Magnetic Resonance (ssNMR)

Nuclear magnetic resonance is an analytical method that uses the resonance of the nuclear spin at S of atoms with odd mass number (or even mass number and odd atomic mass number) and is characterised by a nuclear spin quantum number I (for odd mass number I has semi-integer values, for odd atomic mass number I has integer values). Therefore, atoms with $I \neq 0$ have a quantized magnetic moment μ, as it behaves like a small magnet, according to the equation 2.30[93, 94].

$$\mu = \gamma\hbar\sqrt{I(I+1)} \tag{2.30}$$

With the magnetogyric ratio γ and the reduced Planck's constant $\hbar = /2\pi$. When these nuclei are affected by a strong magnetic field of strength B_0, which is applied in the direction of the z-axis, the nuclei have a particular orientation with a defined energy state. The energy difference ΔE (equation 2.31) between a low state α (parallel to the magnetic field) and a high state β (antiparallel to the magnetic field) depends on the magnetic field B_0 and the magnetogyric ratio[94].

$$\Delta E = \gamma\hbar B_0 \tag{2.31}$$

The nuclei start to precess in the magnetic field at a certain Lamor frequency $\omega = -\gamma B_0$ as shown in Fig: 2.15 A. The transition between these states can be achieved by irradiating the nuclei with a radiofrequency pulse perpendicular to B_0 at a frequency given in 2.32, depending on the magnetogyric ratio γ and the strength of the magnetic field B_0.

$$\nu = \frac{\gamma}{2\pi} B_0 \tag{2.32}$$

The nuclei are flipped sideways by the radiofrequency pulse and induce a signal when they return to the beam precision[93, 94].

Since the frequency ν, the magnetic field strength B_0 and the magentogyric ratio

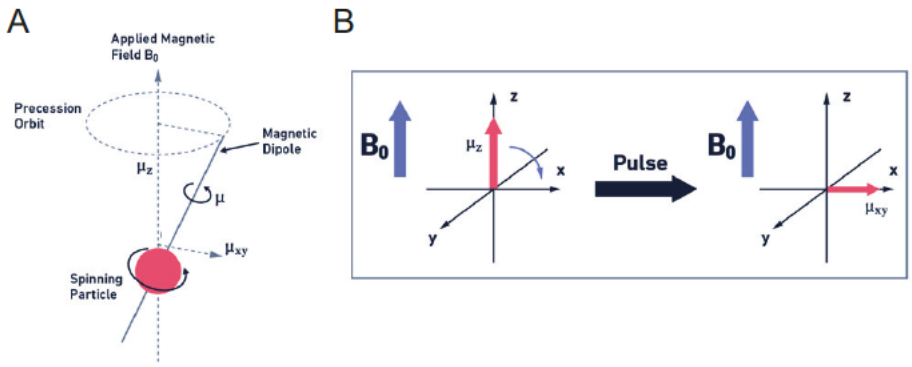

FIGURE 2.15: A: Diagram showing the motion and spin of an atomic nucleus in a magnetic field. B_0 is the direction of the magnetic field, magnetic moment μ. B: Effect of a radiofrequency pulse on a perpendicularly inverted nucleus. Reprinted from Bhande and Bhosale [95].

γ depend on the nuclei, the signal is influenced by the chemical environment. The most common nuclei measured by NMR are ^{1}H and ^{13}C. The signals from these atoms depend on the electronic structure (electrons also induce a magnetic field) in the molecule and shift the signal when they are more or less shielded[93].

In ssNMR, the signal is influenced by additional anisotropic factors, such as chemical shift anisotropy, dipolar coupling, conformation effects, and quadrupole splitting, resulting in a broadening of the spectrum[96]. Such solid-state NMR measurements can be used to obtain information about the solid or liquid state of a sample and are therefore suitable for measuring the solid fat content of fat samples, as the signal is influenced by the mobility of the triglyceride molecules in the sample[97]. A typical setup is shown in Fig. 2.16 and examples of NMR spectra are given in the appendix Fig. A.5 to Fig. A.9.

The fat samples are measured at a controlled temperature T and to estimate the solid fat content (SFC) the total area A_{fs} under the spectrum was integrated, and the baseline was adjusted to the peak of the liquid phase and integrated according to the

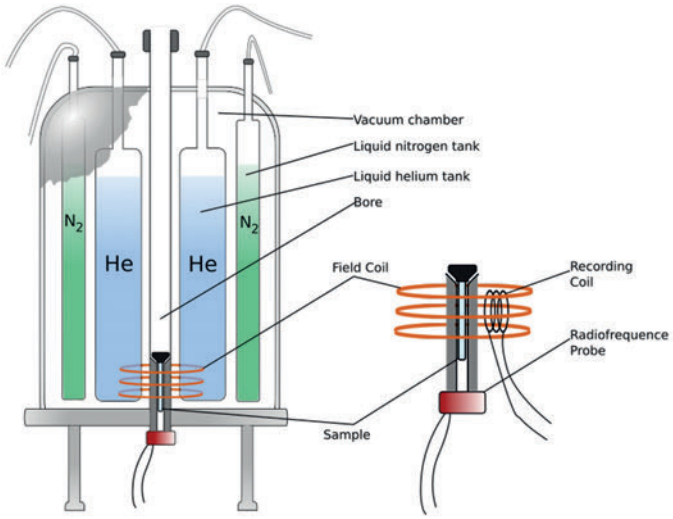

FIGURE 2.16: Schematic of an NMR instrument with cooling and detailed view of the coils that generate the field and detect the signal. Reprinted from Kiss under CC0 licence[98].

reference to obtain the Area A_{sp} of the sharp peak.

$$SFC(\%) = \frac{(A_{fs} - A_{sp})}{A_{fs}} \cdot 100\ \% \tag{2.33}$$

With the equation (2.33) the solid fat content can be calculated.

2.2.7 Wide-angle X-ray scattering

Wide-angle X-ray scattering (WAXS) or X-ray diffraction (XRD) is used to identify the crystalline and amorphous phases of a material and can therefore be used to identify crystalline fat content (CFC). The solid fraction of a fat is not completely crystalline due to the presence of different fatty acids and the resulting polymorphic forms. As a result, there is often a significant amorphous phase in which the lipid molecules lack long-range order. Wide-angle X-ray scattering (WAXS) is a commonly used technique to determine the degree of crystallinity, as it can distinguish between crystalline and amorphous regions within the fat matrix[99]. In contrast NMR can differentiate between the complete solid fat phase and the liquid phase because the signal depends on the mobility of the molecules (see subsection 2.2.6).
Like all electromagnetic radiation, X-rays are a wave of photons with energy $E = h\nu = hc/\lambda$. The energy depends on h, Planck's constant, ν the frequency of the wave, λ the wavelength and c the speed of light. X-rays are usually produced by hitting a cooled metal target (e.g. copper) with a beam of electrons, which produce a wide range of X-rays from the decelerated electrons. Some electrons are absorbed by shifting an inner core electron to a higher energy level. The electron relaxes back to its original state, releasing radiation. In the case of copper, the resulting X-ray radiation is K_α, due to shell K, with $\lambda = 0.1542\,\text{nm}$), which corresponds to the distances between atoms in

crystals[100].
This can be used to obtain information about the crystallinity of an unknown sample. Therefore, Bragg's law (equation 2.34) is used to relate the wavelength of X-rays to the distances between atoms in a crystal lattice.

$$n\lambda = 2d\sin\theta \tag{2.34}$$

It depends on the order of diffraction n, the wavelength λ, d the lattice spacing and θ the angle of incidence of the X-rays. In Fig. 2.17 Bragg's Law is shown for a scattering

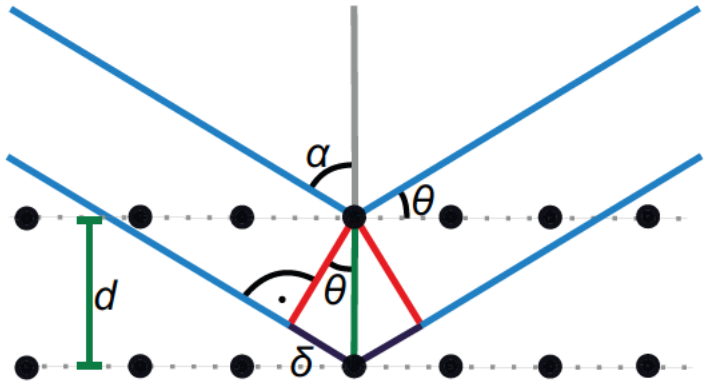

FIGURE 2.17: The Figure shows the diffraction on a lattice plane. With θ as angel of incident, d the lattice spacing and path difference δ. Reprinted from [101] under public domain via Wikimedia Commons.

event of two X-rays with an angle of incidence θ at two particles with a lattice spacing d, one wave has to travel a path difference δ. This path difference depends on θ as shown in the equation 2.35 for incoming and outgoing waves.

$$2\delta = 2d\sin\theta \tag{2.35}$$

If the path difference of the two waves 2δ is a multiple of the wavelength $n\lambda$, as in the equation 2.34, the intense Bragg reflexes result[100].
The samples were measured using a diffractometer (schematic setup is shown in Fig. 2.18) and the results are usually plotted in a diffractogram as shown in Fig. 2.18 B. The sample is mounted in the centre and the beam from the X-ray source is directed to the sample via the Göbel mirror. The reflected X-rays are collected by a detector through a Soller slit. The detector moves at an angle around the sample and the measured signal corresponds to 2θ. The lattice parameters can be derived from this diffractogram[100].

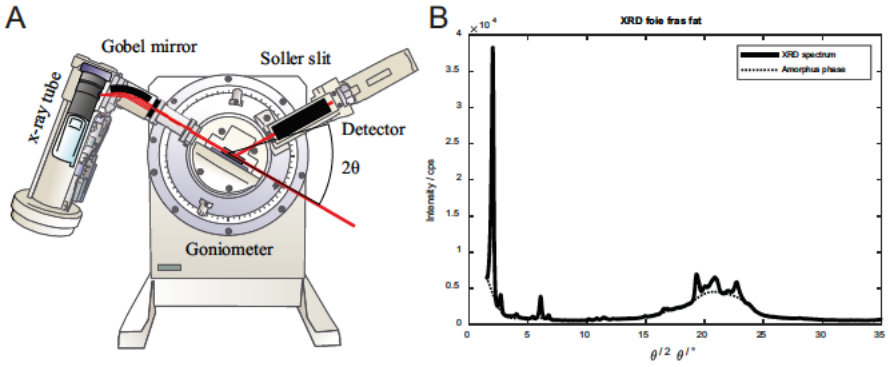

FIGURE 2.18: The figure, part A, shows a schematic diagram of a diffractometer, with the X-ray source and the optical components, the Göbel mirror and the slit to focus the beam. The sample is mounted in the centre and the detector moves at an angle around the sample. The angle between the beam and the detector is equal to 2θ. Part B shows the diffraction pattern of foie gras fat (solid line) with the amorphous phase marked by a dotted line on a lattice plane. Part A is Reprinted from DrBoStefanov, CC BY-SA 4.0, via Wikimedia Commons[102], Part B reprinted from [103]

This also applies to fat crystals, but to estimate the crystalline fat content (CFC), the amount of crystalline fat and amorphous phase must be estimated, so the total area with reflections is calculated as well as the amorphous phase without the peaks (dotted line in Fig. 2.18 B)[104].

$$CFC(\%) = (1 - \frac{A_{\text{amorphous}}}{A_{\text{total}}}) \cdot 100\ \% \tag{2.36}$$

The CFC is then calculated with the equation 2.36.

Chapter 3

Microscopic Characterization of Fatty Liver based Emulsions: Bridging Microstructure and Texture in Foie Gras and Pâté

Via, M. A.; **Baechle, M.**; Stephan, A.; Vilgis, T. A.; Clausen, M. P.

This chapter is a version of the manuscript published in *Physics of Fluids* 33, 117119 (2021) https://doi.org/10.1063/5.0070998

Abstract

Analysis of food materials often involve characterization of the molecular composition of the food matrix and measuring its mechanical properties. However, there is a gap in understanding how food materials organize at the microscopic level. This article shows the application of minimally invasive coherent anti-Stokes Raman scattering (CARS) microscopy to visualize the fat distribution in duck liver-based products. Further, in combination with quantitative image analysis, CARS provides a viable route for understanding how food texture relate to food microstructure. Strong correlations were found between microscopic structural descriptors of the fat particle (abundance, shape, and size) and rheological and textural parameters (hardness, storage modulus). Foie gras was found to have an irregular shaped fat network connected via relatively weak links that yield under stress correlating with foie gras being harder, more elastic, and more brittle in comparison with a homemade duck liver pâté. In turn, the higher total number of fat particles, more round and smooth in shape, found in the pâté was responsible for it being softer and less prone to fracture. Understanding the relation between molecular composition, microscopic structure, and macroscopic texture provides opportunities for future modification of pâté formulation and/or new preparation technique, using microstructure as a texture indicator.

3.1 Introduction

Correct texture of food has a crucial influence on the enjoyment of eating and acceptance of new food[105, 106]. Texture is often studied recording the mechanical properties of food materials and relating these to the composition and physicochemical state of the food or by sensory evaluation. However, the underlying microscopic structures and rearrangements that, to a large extent, determine food appearance, texture, and handling properties, remain more elusive. Insight into such microstructures therefore provides a valuable route for gaining a more complete gastrophysical (physics of gastronomy)[107] understanding of the relation between structure and function, and sensory properties of food materials. This in turn allows to bridge information from the molecular to the macroscopic scale and provides opportunities for better control and optimization of food preparation and processing.

Foie gras (*literal meaning: fatty liver*) is considered a delicacy and is highly appreciated for its unique textural properties. It is a food product based on the fatty liver of duck or goose typically produced as a sliceable whole liver organ (*entier*)[22] or as a mechanically reconstituted block of different homogenized pieces of foie gras (*bloc*)[108]. From a soft matter point-of-view, foie gras *bloc* is, in analogy to comminuted meat products, a multiphasic system comprised of a continuous phase consisting of proteins, salts, water, carbohydrates, and fibrous particles, and a dispersed phase consisting of solid fat particles, liquid fat globules, and non-soluble meat components[109]. Technically, it can be described as composite gel that contains fat particles emulsified in a protein gel matrix, but the term meat batter or meat emulsion is also often used[110, 111].

Production of foie gras exploits the natural tendency of these migratory birds to accumulate fat in the liver and often involves force-feeding[22]. Liver products from force-fed sources score considerably higher in sensory evaluation in texture, taste, and smell attributes as compared to products generated through spontaneous fattening,[112] but these differences are not fully understood from a gastrophysical perspective. However, since the force-feeding practice is questionable regarding animal welfare,[26] it puts forward the quest for finding alternative preparations that match the texture quality of foie gras.

Several studies have targeted liver pâté[11, 15, 16] and meat emulsion[113–115] texture and stability by varying either the lipid composition, introducing dietary fibres, or a combination of both. The main focus of these studies has been to obtain textural properties similar to the reference product, and simple attempts to quantify the microstructure and relating this to texture has been made [11]. So far, the mechanical properties of foie gras and liver pâté have not yet been compared, and the microstructure of neither have not been assessed in detail.

Optical microscopy has proven a valuable tool for unravelling the complex organization of biomaterials due to its non-destructive nature, high spatio-temporal resolution, and sectioning capabilities. While microscopy has been instrumental for understanding

food structure, some issues remain regarding sample preparation, making imaging impractical or impossible, or even altering the native structures in the worst scenario. Further, although not being a methodological limitation, most food microscopy studies are applied qualitatively rather than quantitatively limiting their direct comparison and correlation to relevant parameters at different length scales, e.g., mechanical properties.

In recent decades, coherent Anti-Stokes Raman scattering (CARS) microscopy and related techniques have emerged as powerful imaging techniques that have found increasing use in the biological and medical sciences. CARS microscopy requires minimal sample preparation without need for extrinsic staining, enables fast image acquisition (up to video rate, 30 fps) at high spatial resolution (<1 µm) and deep inside tissue (>100 µm). Contrast in the sample is based on intrinsic molecular vibrations targeted by simultaneous illumination of the sample with two lasers with an energy difference matching particular chemical bonds. By tuning the energy difference of the lasers, different molecular vibrations can be targeted, e.g., the -CH_2 stretching mode of lipids at 2845/cm, with signal produced being orders of magnitudes larger than spontaneous Raman scattering. In many respects, CARS is an ideal candidate for imaging food structures, yet so far, only very few applications are found[115–117].

In this study, we assessed the textural differences between force-fed duck foie gras and spontaneously-fattened duck liver pâté products. In light of their intrinsic high fat content, CARS microscopy and quantitative image analysis were used to determine microstructural parameters to explain the mechanical/textural differences between both type of liver products. Overall, we show that the correlation of mechanical properties and microstructures can provide valuable insight into the texture of complex multiphasic food materials.

3.2 Materials and Methods

3.2.1 Meat emulsions preparation

Foie gras sample, FG1, (Domaine de Langlardie, Piegut Dordogne, France) is comercially available in French supermarkets and foie gras sample, FG2, was bought directly from the producer (La Ferme Schmitt, Bischoffsheim, France). The home-made pâté (HME) emulsions were prepared using 50 % of spontaneously-fattened duck liver (Leon Dupont, Notre Dame de Riez, France), 40 % rendered duck fat (Bruno Siebert, Ergersheim, France), 10 % water and 2 % NaCl (w/w) (AnalaR NORMAPUR, VWR Chemicals, Darmstadt, Germany). The comminution was performed with a Hallde vertical cutter blender VCB-62 (AB Hallde Maskiner, Kista, Sweden). A first chopping step of the liver was performed at 1500 rpm for 5 s, followed by a second step at 3000 rpm for 10 s. Sodium chloride was added to the liver and stirred shortly. Afterwards, fat and water were added to the liver paste and emulsified following a two-step blending process: 1500 rpm for 15 s, followed by 3000 rpm for 30 s. Liquid nitrogen (50 mL to 100 mL) was added between each step for temperature control. The

final batter had a average temperature of 15.3 ± 3.3°C ranging from 9.8 °C to 20.7 °C. The batter was filled into plastic containers and cooked in a preheated oven at 80 °C for 90 min. After heating, the samples were stored in a fridge at 5 °C for cooling.

3.2.2 Rheological properties

Rheological measurements were performed with a Bohlin Instruments Gemini 200 rheometer (Malvern Panalytical Ltd., Malvern, UK) equipped with a 25 mm parallel plate geometry. To prevent sample slipping, both plates were covered with 80 grit sandpaper. Before placing under the geometry, the sample was shaped using a round stencil (⌀25 mm) and sliced in thin disks. The gap size was step wise adjusted to the thickness of the slices until an increase of the normal force was detected leading to gap sizes between 1100 µm to 1700 µm. Oscillatory amplitude sweeps were performed from 0.01 % to 200 % strain with a frequency of 1 Hz at 5 °C, while recording the storage (elastic) modulus, G', and loss (viscous) modulus, G''. Each sample was at measured at least 3 times. The limit of the linear viscoelastic region (LVR) was determined as the strain at which a 10 % deviation from the G'_0 was reached. The cross-point was determined as the strain where $G' = G''$.

3.2.3 Texture Measurements

Hardness of foie gras and pâté samples was measured with a ZwickRoell Universal Testing Machine AllroundLine Z005 (ZwickRoell GmbH, Ulm, Germany) [118]. Samples were trimmed into cylinders (⌀25 mm, 20 mm height). Penetration tests were performed using a steel rod probe (⌀10 mm) with a speed of 1 mm/s, until a deformation of 75 % of the sample height was reached. All measurements were performed at room temperature with samples cooled to 5 °C. Each sample was measured at least three times. Sample hardness was calculated considering the maximum peak force during compression, while the initial slope of the compression curve was determined by linear regression of the first five points above a threshold from 0.01 % strain, to estimate the elasticity of the samples.

3.2.4 Moisture Analysis

The moisture content of the samples was measured with a Mettler-Toledo HS153 halogen moisture analyzer (Mettler-Toledo, Columbus, US). Around 0.5 g of each sample was spread onto a fiberglas filter paper and placed in the device. The drying temperature was set to 120 °C with a time ramp of 3 min and the switch-off criterion was 1 mg/180 s of weight change. Each sample was measured at least 3 times.

3.2.5 CARS Microscopy

Coherent Anti-Stokes Raman scattering (CARS) microscopy characterization was performed using a Leica SP8 CARS microscope (Leica Microsystems GmbH, Mannheim, Germany) equipped with a picoEmerald (APE, Berlin, Germany) multi-photon laser

as the light source. The Stokes beam was fixed at $\lambda = 1064.5\,\text{nm}$, whereas the pump beam was tuned to $\lambda = 817\,\text{nm}$ to excite symmetric -CH_2 stretching ($2845\,\text{cm}^{-1}$) for visualization of fat in the samples. Epi-mode detection was performed using a non-descanned photo-multiplier tube (PMT) detector. A filter cube was placed in the detection path with a laser-blocking short-pass filter at 750 nm, a dichroic mirror at 560 nm and a broadband filter 650/210 BrightLine HC (AHF analysentechnik AG, Tübingen, Germany). All images were acquired with a 40× HC PL IRAPO 1.10 NA Leica objective at room temperature. The laser power was adjusted for each image to give a signal intensity of about 20 % of the saturation limit. Foie gras and pâté samples were sliced and placed in an 8-well chamber with a #1.5 glass bottom (Ibidi GmbH, Gräfelfing, Germany) immediately before imaging. Images of size 1928x1928 pixel^2 with pixel size = 15 µm were recorded at 5 µm depth into the sample in seven different regions of interest per sample giving a total of 21 images as each of the different sample types (FG1, FG2, and HME) were measured in triplicate.

3.2.6 Image analysis

Images were processed with *Fiji* software.[119] First, an automatic threshold (Huang algorithm)[120] was applied to obtain binary images that allowed for identification of individual fat particles. Particles below the resolution limit were considered as noise and excluded from further analysis, while clusters with boundaries not entirely included in the image frame were also excluded. Analysis of fat particles included the following parameters: mean particle number per image, particle area, total area occupied by particles as well as their perimeter, aspect ratio, circularity and Feret's diameter. *Aspect ratio* (AR) is the ratio between the longest and shortest axis of an ellipsoid fitted in the particle area. By definition, AR=1 is a perfect circle, while increasing values account for deviation from this shape. *Circularity* relates area and perimeter of the particle and accounts for the edge sharpness. It ranges between 0 and 1, where the maximum value corresponds to a smooth circle and decreasing circularity correlates with surface roughness. Feret's diameter is defined as the maximum distance between two points within the particle (also known as maximum caliper). For the characterization of large interconnected clusters, the size threshold was defined considering the 90^{th} percentile (P90) of the cumulative frequency of particle size for each sample, which represents the 10 % largest particles of the total population. The size threshold to compare the three P90 was calculated as the mean between maximum and minimum P90, which yielded a size threshold of $4500\,\mu\text{m}^2$.

3.2.7 Statistical Analysis

All significant differences between pâté and each FG sample were calculated using t-test with a significance level of 5% ($\alpha = 0.05$) (Minitab 19, State College, PA, USA). Data for each meat emulsion was collected from a total of 21 images obtained from three independent samples (n=3). To assess the correlation between microscopic features

TABLE 3.1: Physicochemical characterization of foie gras and pâté samples.

	Rheological parameters		
Sample	**G'** (Pa)	**LVR**[1] (% strain)	**Cross-point** (% strain)
HME	31,418±8,957	0.95±0.22	56.05±9.22
FG1	199,010±79,859	0.21±0.09	30.44±14.80
FG2	357,801±31,528	0.19±0.005	45.24±14.89

	Texture Profile Analysis		
Sample	**Hardness** (N)[2]	**Initial slope of compression curve**[3]	**Water content** (%)
HME	1.99±0.46	0.24±0.07	44.26±0.85
FG1	6.68±0.87	0.64±0.02	42.23±0.29
FG2	11.35±0.18	0.35±0.09	33.03±1.63

[1]Linear Viscoelastic Region: region where applied stress is insufficient to cause structural breakdown (yielding) and hence microstructural properties are being measured. This corresponds to the point at which G' becomes stress or strain dependent.
[2]Maximum peak force during compression.
[3]Fitted slope of the first data points.

and rheological parameters, Pearson correlation coefficients were determined. The Pearson correlation coefficient is a measure of the degree of linear correlation between two data sets, calculated as the ratio between the co-variance of the two variables and the product of their standard deviations. This gives values between -1 and 1, and the extreme values corresponds to perfect negative and positive linear correlation, while 0 corresponds to no linear correlation at all.

3.3 Results

3.3.1 Rheological and textural assessment of foie gras and pâté emulsions

Mechanical properties of two commercial brands of foie gras *bloc*, FG1 and FG2, and a homemade duck liver pâté, HME, were studied through amplitude sweeps, in a rheometer determining the storage modulus, G', and loss modulus, G", as a function of strain% (Fig. 3.1), and by compression deformation in a texture analyzer determining the force vs. strain relation (Fig. 3.2). Main parameters from these analyses are summarized in Table 3.1.

As seen from Fig. 3.1, in the linear viscoelastic region, LVR, for all three samples, G' > G" meaning that the samples display more gel-like behavior than liquid behavior. As expected for gel structures, increasing strain results in a non-linear regime, where the structure yield, and G' decrease. Initially, samples still predominantly display gel-like properties, where also G" decrease with increasing strain%, but after the cross-point G" > G', and the samples predominantly behave as fluids indicating complete fracture of the gel structure.

Clear differences in the mechanical response to shear strain can be seen between foie gras samples and the pâté sample. For FG1 and FG2, both G' and G" are roughly

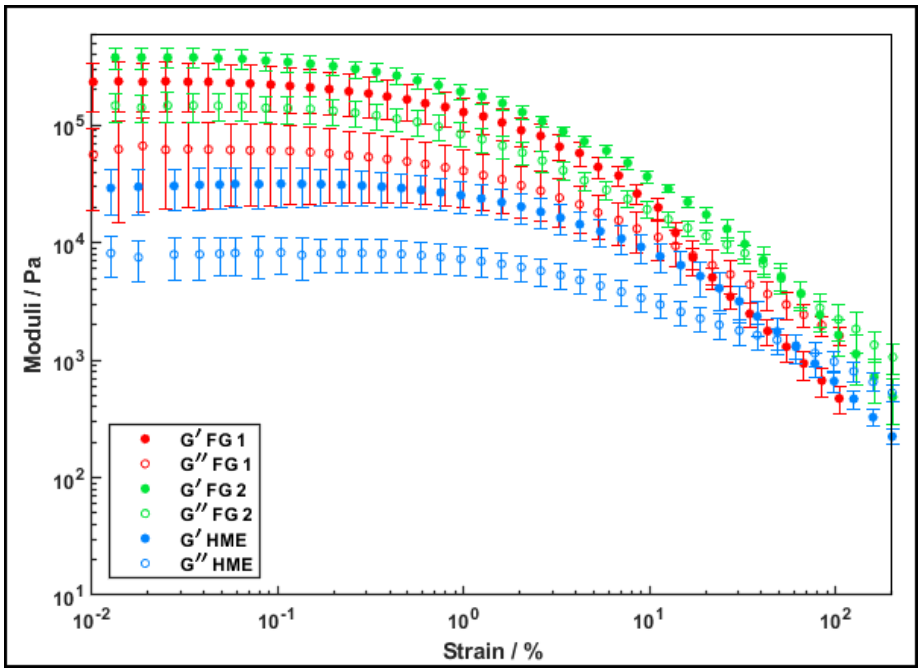

FIGURE 3.1: Amplitude sweep measurements. Storage modulus G' (filled circles) and loss modulus G" (open circles) are displayed for FG1 (red), FG2 (green) and HME (blue).

an order of magnitude larger than that of the HME, with FG2 having a higher G' than FG1, denoting a stronger gel strength in these samples. While all three samples show a rather short range of viscoelastic deformation, HME displays a longer LVR, and also a larger strain value at the cross-point reflecting a structure that is more resistant to fracture and flow. Moreover, HME is also less brittle than either of FG samples.

The large-scale compression-force deformation measurements support the previous results of the foie gras samples being stronger but more prone to fracture. As seen from Fig. 3.2, the hardness (maximum peak force) of FG1 and FG2 are much larger than that of HME. For FG1 and FG2, after the peak is reached, the force rapidly decreases again showing structural breakdown of the sample, while for HME the force is kept at a constant, although lower, level. The initial slope of the deformation (see inset in Fig. 3.2) also confirms a much more elastic response to deformation in FG1 and FG2 as compared to HME.

3.3.2 Microscopic characterization

To get insight into the microstructures that underlie the observed differences in mechanical properties between foie gras and pâté, CARS microscopy was used to visualize the distribution of fat in the samples by probing the $-CH_2$ stretch (Fig. 3.3). A clear contrast between a particulate lipid phase (red) and a continuous water/protein phase (black) was observed for all samples. Qualitative inspection suggest that the overall area covered by lipid is similar between samples reflecting their compositional similarities. In all samples the fat particles occur as clusters that are heterogeneously distributed within samples with varying size and morphological features. Closer

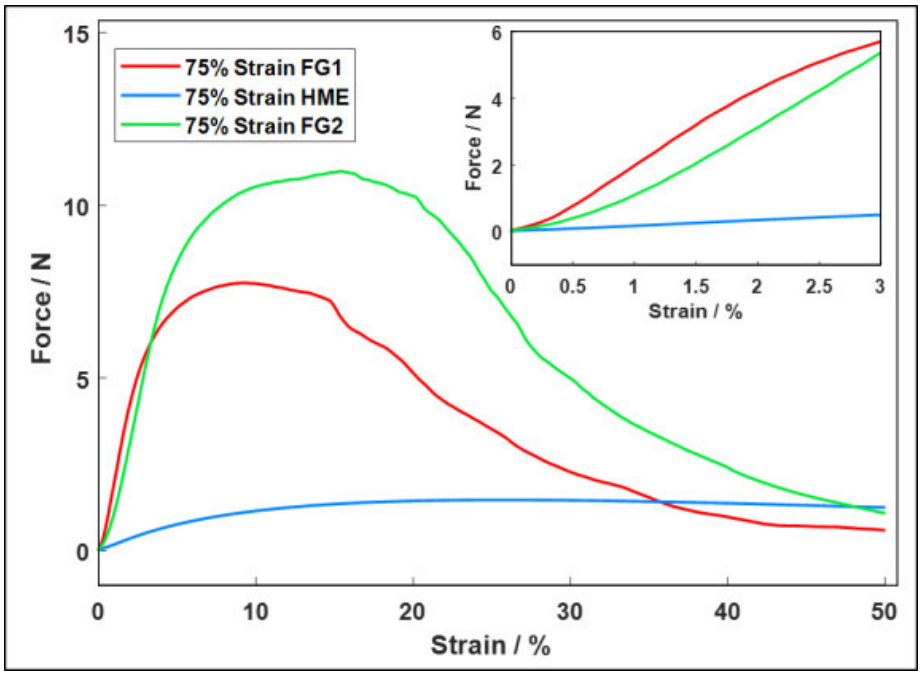

FIGURE 3.2: Texture analysis. Compression curves for FG1 (red line), FG2 (green line) and HME (blue line). The inset shows a zoom-in of the initial part of the compression until 3% strain.

inspection of these fat particles suggests that the shape for FG1 and FG2 is more irregular than for HME, which has more round particles with smoother surfaces. It is further observed that fat particles are generally larger for FG1 and FG2 than HME, and that these large particles in many cases contain links between different parts of the particle as indicated with arrows in Fig. 3.3. These intra-cluster links are more frequently occurring in FG1 and FG2 samples as compared to HME.

In order to systematically compare the liver pâtés, we proceeded to quantify the number of fat particles along with the shape descriptors of each individual particle i.e. area, aspect ratio, circularity, perimeter and Feret's diameter.

3.3.3 Quantitative image analysis

The qualitative description of the microscopy images and fat particles in the foie gras and liver pâté was followed by quantitative image analysis to parameterize fat particle number and sizes (Fig. 3.4) and morphology (Fig. 3.5), as well as their correlation (Fig. 3.6). Image quantification further allows for directly relating microscopic features to the mechanical properties.

Quantification of the total area covered by fat confirms the overall compositional similarities between the samples, as it was FG1 = 43.3 %, FG2 = 51.3 %, and HME = 43.7 %. As seen from the analysis of individual fat particles shown in Fig. 3.4, all samples have a large mean number of fat particles and a polydisperse size distribution in a range from approximately 1 µm^2 to 10.000 µm^2 with about 50 % of all particles being in the intermediate size range of 100 µm^2 to 2.000 µm^2 (corresponding to circular

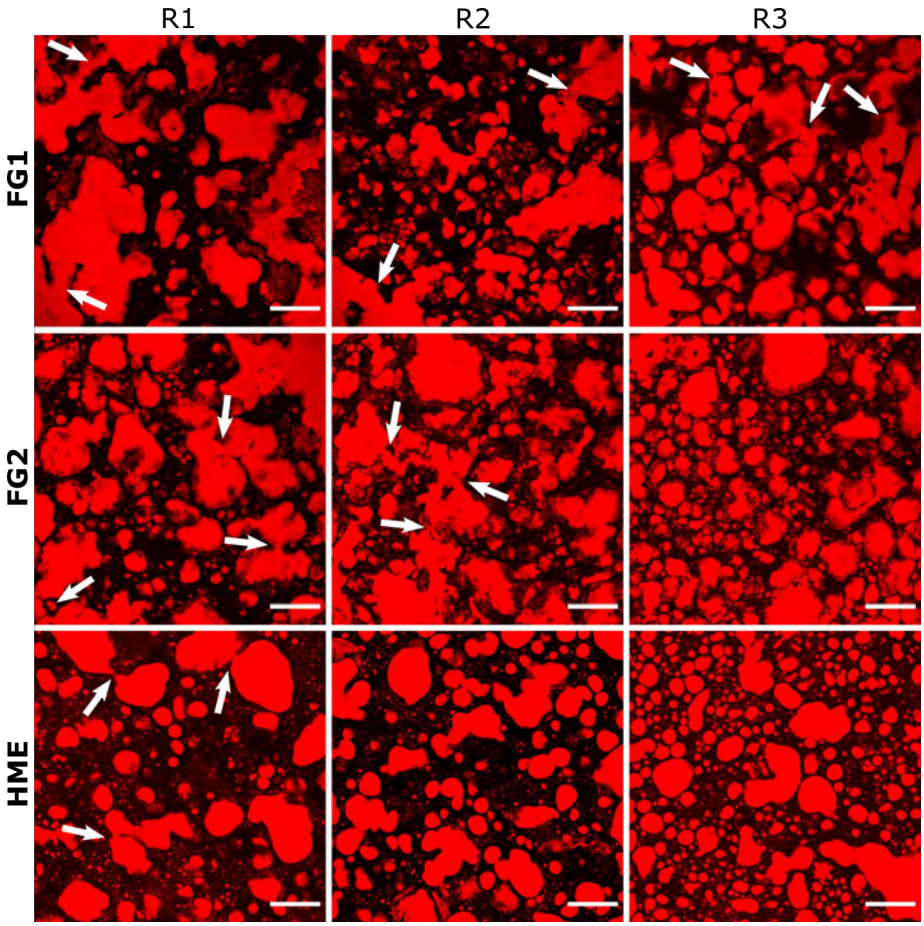

FIGURE 3.3: CARS microscopy of fat distribution. Representative raw images of FG1 (first row), FG2 (second row) and HME (third row) from three replicates (columns R1, R2, R3). White arrows indicate intra-cluster links. Image contrast was enhanced for the purpose of visually accentuating the lipid features. Scale bar = 50 μm.

particles of ⌀ 6 µm to 30 µm). Clear differences are seen in the mean number of particles per image between FG samples (FG1 and FG2) and HME, with the latter having about twice as many particles as compared to FG1 and FG2 (Fig. 3.4.a), which results in a significantly higher density of particles. The standard deviation of the mean particle number reflects differences between different regions of interest within each sample. This standard deviation was found to be significantly larger for HME as compared to FG1 and FG2, suggesting that the FG1 and FG2 samples are more self-similar in terms of particle distribution per unit area.

The size distribution of individual particles (Fig. 3.4.b) reveals that the observed difference in total number of particles between FG1 and FG2 compared to HME mainly originates from the smallest size groups (<1 µm^2 and 1 µm^2 to 10 µm^2), where HME has considerably more particles that FG1 and FG2. Conversely, FG1 and FG2 samples both display higher counts of the larger fat clusters (>4.000 µm^2) compared to HME. If the particle distributions are weighed by area (Fig. S1), these large particles account for ∼13% of the total area in both FG samples against 4 % for pâté.

Not only particle number and size will influence the mechanical properties of foie

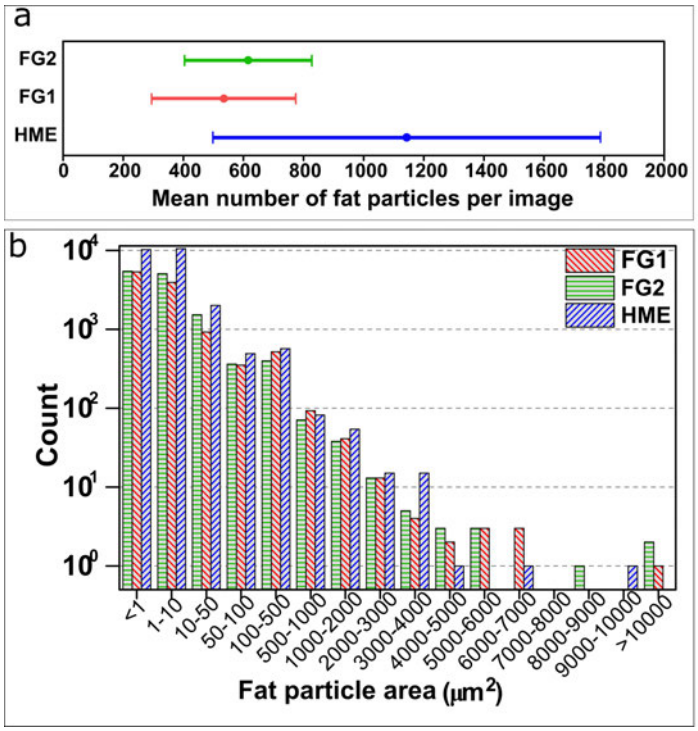

FIGURE 3.4: Fat particle number and size. The mean number of fat particles (a), and fat particle size distribution (b) of FG1 (red), FG2 (green), and HME (blue).

gras and pâté, so will particle morphology. As seen from Fig. 3.5, all samples have a wide distribution of aspect ratio and circularity, but clear differences are also seen between samples, and again, FG1 and FG2 show similar features to each other but differ from HME. In terms of roundness, the aspect ratio measures the shape elongation of the fat particles, and this is much closer to 1 (perfect circle) for HME than for FG1 and FG2, that both have aspect ratio distributions shifted towards higher values (Fig. 3.5.a). Circularity quantifies the surface roughness of the particles, and FG1 and FG2 samples share a left-skewed distribution of circularity towards 0 corresponding to fat particles markedly departing from the smooth surface of a perfect circle (circularity of 1) (Fig. 3.5.b). In contrast, HME has a centrosymmetric distribution of circularity indicating that particles have a smoother surface, although not perfectly smooth.

Large fat particles can have a major impact on the textural properties of products such as foie gras and pâté. Based on the visual inspection of Fig. 3.3, interconnected clusters display a wide elongation and irregular shapes, while covering large areas. Accordingly, Feret's diameter, perimeter and circularity were calculated as main characterization variables for these connected clusters. The size threshold was set to 4500 µm^2, which corresponds to the on average 10 % largest particles in all samples.

Plotting the Feret's diameter as a function of particle size (Fig. 3.6.a) reveals a positive correlation, showing that the largest clusters in all samples are indeed the most elongated, which coincides with the observed interconnected clusters. Quantification of cluster number above 4500 µm^2 yielded higher counts in FG1 and FG2 samples than

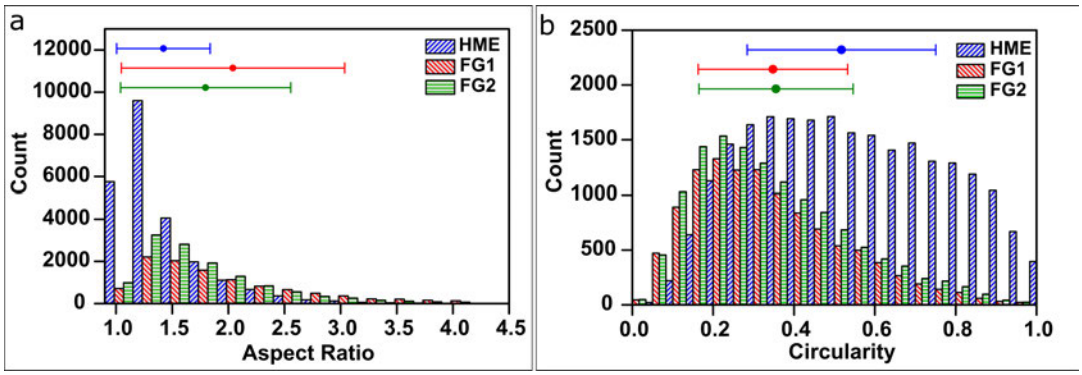

FIGURE 3.5: (a) Aspect ratio distribution and (b) circularity distribution of HME (blue), FG1 (red) and FG2 (green).

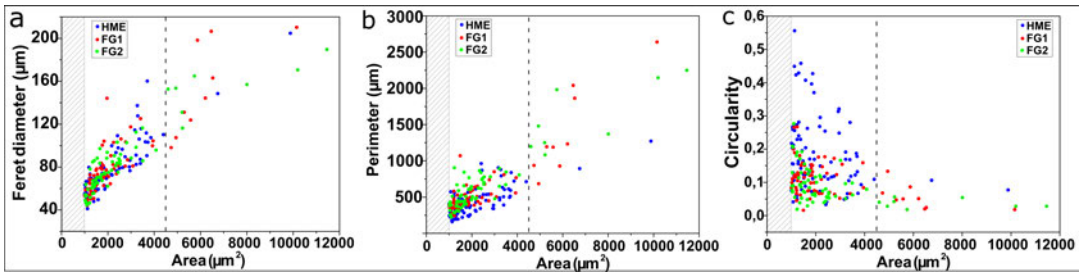

FIGURE 3.6: Relationship between particle size (area) and (a) Feret's diameter, (b) particle perimeter, (c) circularity of HME (blue), FG1 (red) and FG2 (green). The dotted line represents the P90-based size threshold to quantify the largest clusters in each sample. For better visual understanding, only particles above 1000 μ^2 are plotted.

in HME. In turn, there is a higher contribution of these interconnected clusters to the total fat area in FG1 and FG2 than to HME: 12.7 %, 11.3 % and 2.1 %, respectively.

Positive correlation was also found between particle size and perimeter for all samples (Fig. 3.6 b), but interestingly, when comparing clusters of similar size, FG1 and FG2 always have larger perimeter compared to HME, meaning that the large interconnected clusters in FG1 and FG2 have more irregular surfaces. This is well in line with the particle circularity being lower for FG1 and FG2 than for HME (Fig. 3.6.c).

In summary and in agreement with the differences in mechanical properties, the quantitative image analysis also found considerable microstructural differences between foie gras samples and homemade pâté. The average fat particle in the homemade pâté are smaller, rounder, and smoother than in foie gras. Moreover, homemade pâté has more fat particles though this changes throughout the sample given its high spatial heterogeneity. Conversely, foie gras samples presents a more homogeneous spatial distribution of relatively large interconnected fat particles with irregular surface and elongated shape.

TABLE 3.2: Pearson coefficients for the correlation between microscopic and rheological parameters.

	Rheological parameters			
Microscopic descriptors	**G'**	**LVR**	**Flow point**	**Hardness**
Spatial heterogeneity[1]	-0.865	0.999	0.820	-0.895
Feret's diameter	0.945	-0.972	-0.695	0.964
Aspect ratio	0.602	-0.937	-0.978	0.652
Perimeter	0.993	-0.902	-0.528	0.998
Total interfacial surface[2]	-0.575	0.925	0.984	-0.626
Circularity	-0.828	1.00	0.857	-0.862

[1]Defined as the standard deviation of mean particle number.
[2]Perimeter summation of all particles in each sample.

3.3.4 Correlation between microscopic descriptors and textural parameters

To relate the microscopic distribution and morphology of fat particles to the mechanical properties of foie gras and pâté, correlation coefficients between measured microscopic descriptors and mechanical parameters were calculated. This data is summarized in Table 3.2. As can be seen in the table, the initial storage modulus G'_0 and the sample hardness have strong positive correlations with Feret's diameter and particle perimeter, but a strong negative correlation with fat spatial heterogeneity and particle circularity. This suggest that increased gel strength is associated with presence of large, elongated particles of irregular shape, which are distributed evenly throughout the sample.

The initial resistance to deformation as represented by the limit of the LVR correlates strongly and positively with the circularity, total interfacial perimeter, and spatial heterogeneity of fat particles while correlating strongly negative with Feret's diameter, aspect ratio and perimeter, showing that generally matrices with more, rounder, and smaller particles are less prone to fracture.

The cross-point of the systems also correlates strongly and positively with the circularity and total interfacial perimeter, while having a strong and negative correlation with aspect ratio. This suggests that having more, round, and smooth particles renders the matrices more resistant to complete fracture and flow.

3.4 Discussion

The textural properties of different categories of fatty duck liver-based emulsions i.e. commercial foie gras and homemade pâté, were investigated using rheology and texture analysis and found to be similar within product category but differ between. In comparison to duck liver pâté, foie gras samples had a higher gel strength and was more brittle. In contrast, the pâté was comparatively weaker and showed a higher resistance to structural fracture. To uncover the microstructural characteristics that underlie these textural differences, the distribution and structures of the fat in such fatty liver-based products were for the first time visualized using CARS microscopy. Recent

studies have targeted how the microstructure of pâté is affected by fat content and type [11, 15, 16]. These studies used normal light microscopy to image samples that were fixed, stained, and embedded in paraffin. In contrast to this, CARS microscopy did not require any staining, fixation or embedding, but native samples could be imaged directly within the sample matrix to give highly specific signal from the fat and high signal-to-noise. Previously, only a simple quantitative analysis of pâté microstructure has been presented[11] only reporting an average fat particle size. Based on the acquired CARS microscopy images, we were able to perform a thorough quantitative image analysis that take both particle abundance, size, and shape factors into account in order to better uncover a relation between texture and microstructure. This image analysis confirmed that also at the microscopic level, the foie gras samples showed similar characteristics, which differentiate them from those of the homemade pâté. While fat particles in foie gras samples were relatively large, irregular in shape, and linked together to form an interconnected fat network, the homemade pâté was characterized by having more, smaller, and rounder fat particles that were not interconnected.

In foie gras, the fat distribution originates from the natural distribution of fat developed during force feeding. The fat is physiologically deposited in vacuoles inside hepatocytes producing a physical enlargement of these cells, which also result in an increased production of extracellular proteins, mainly different types of collagen[121]. During the preparation of foie gras, only very mild shear rates are required, and therefore most of the fat remains intact within cells during the preparation, as has been shown for liver sausages prepared under higher shear[4]. Even during the final cooking of the foie gras during which a temperature of 65 °C to 70 °C is reached, the fat mainly remains trapped within cells, though fat droplet fusion may occur but in the raw liver cells[31]. Depending on the rate of the subsequent cooling, the polymorphs of the crystalline parts of fats will re-arrange inside the fat particles and introduce deformations in the final fat particle shape. Such deformations are seen in the CARS images (Fig. 3.3). The temperature ramp of preparation also causes denaturation and cross-linking of some liver proteins in the continuous aqueous protein phase. In this way, free non-self cross-linked cysteines from serum albumins and vitelin-1 form a weakly cross-linked gel around the fat clusters.

On the other hand, the preparation of the homemade pâté uses rendered fat and involves a high-shear cutting process, which is performed at low temperatures to prevent thermal denaturation of liver proteins and to maintain the fat in a solid state. Therefore, the structure of the pâté is a result of a highly non-equilibrium process. During the comminution and mixing process, the solid fat is dispersed in the liver water-protein phase, which simultaneously develops into a viscoelastic matrix as globular albumin-type proteins mechanically denature and undergo morphological changes that increase their surface activity. This blocky distribution of hydrophilic and lipophilic amino acids of albumins and other liver proteins ensure a stable emulsion during cooking. At this point, fat droplets with higher circularity are formed by minimizing the interfacial energy. During the cooling process after the heating (cooking) process,

fat particles formed are more likely to retain the highly circular droplet shapes since the distribution of fatty acids is sufficiently broad[108]. This is in agreement with the homemade pâté showing smaller and circular emulsion-type fat droplets (Fig. 3.4 and Fig. 3.5), which do not seem to be able to form networks on larger scales (Fig. 3.3). The CARS micrographs suggest the presence of occasional larger fat particles, but there is no indication that these large particles are interconnected forming a network.

To connect the microscopic morphological differences between foie gras and pâté samples with the corresponding observed differences in mechanical response, Figure 3.7 depicts segmented CARS images that highlight characteristic fat particles features (green and red coloured). The rows in Fig. 3.7 show typical fat distributions of foie gras and pâté under imagined progressive shear deformation from left to right. Large clusters are shown in green color. Foie gras display large connected clusters, which form an irregular fat network, whereas in pâté, the largest clusters remain embedded among small fat droplets. Consequently, the contribution of the fat to the mechanical properties is quite different[122], given that connected fat networks transport mechanical forces/stresses and show characteristic changes of the storage G' and loss G" moduli (Table 3.1)[123, 124].

The storage modulus contains mainly three contributions: (i) the weakly cross-linked protein matrix, (ii) the hydrodynamic part from the isolated fat particles acting as fillers[125], and (iii) the contribution of the solid, crystalline fat network in the samples. The overall modulus remains constant under small shear deformations as long as the structure does not change, as it can be seen in Fig. 3.1 in the range between 0.01 % and 0.1 % of strain. However, the connected clusters in foie gras show "weak links", which break subsequently under shear. The modulus decreases at deformations where the weak links in the largest clusters start to break apart. In addition, further softening by changing the matrix at moderate deformations imposed during the compression experiments are caused by disrupting hydrogen bonds [126] and electrostatic complexes between differently charged amino acids between neighboring protein sequences [127].

The breaking of the fat network at the weak links defines the limit of the LVR range. From Fig. 3.3 and Fig. 3.7, it can be crudely estimated that, e.g., the size of the largest cluster in FG2 is about 250 µm (Feret's diameter), whereas the distance between weak links can be estimated from Fig. 3.3 to be about 50 µm, suggesting a local shear deformation about 0.2 % for breaking the weak links towards the end of the linear viscoelastic regime. Assuming a fine deformation processes before the break down of the particle network, this estimate agrees with the measured values.

The situation in the pâté is quite different. The contribution from the solid fat network to the storage modulus is missing, thus remaining mainly assigned to the weakly cross-linked protein network and the hydrodynamic reinforcement by the crystalline fat particles[125]. Not surprisingly the hardness is lower, the storage modulus is lower, and the LVR is longer, as it is summarized in Table 3.1.

These ideas are underlined by the results from the compression measurements

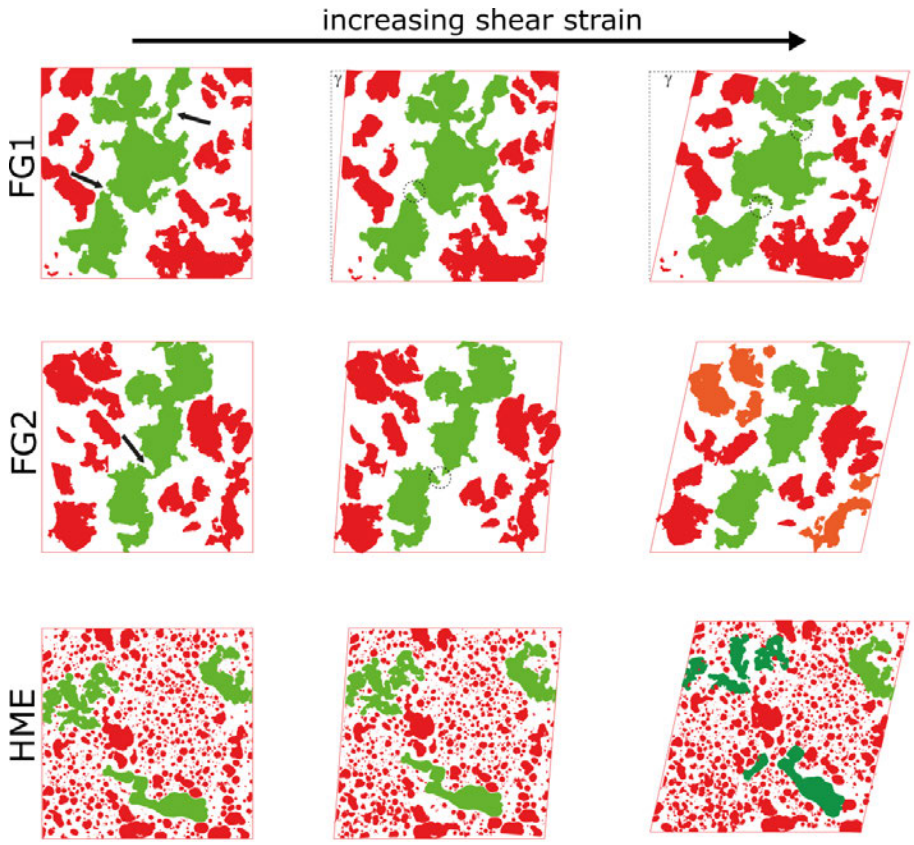

FIGURE 3.7: The different pâtés show significantly distinct fat distributions. The fat droplets of HME are more spherical and well separated, whereas the natural pâtés show larger irregular shaped fat clusters, which form fat particle networks on larger scales. The arrows show the weak links in FG1 and FG2, which break at corresponding shear amplitudes, indicated by the circles. The fat cluster break further apart at higher shear rates (right). The separated dark green colored larger clusters in HME break apart at corresponding shear rates and contribute mainly to a higher loss modulus G" at high shear deformations compared to FG1 and FG2.

shown in Fig. 3.2. The compression force increases steeply for foie gras samples and show a maximum force indicating the fracture of the matrix. These observations are in accordance with results from rheology. At small compression deformations ($< 4\,\%$) the solid fat network resists the compression force until it breaks at the weak links. When the large fat clusters are broken, the deformations enter the plastic regime at strains larger than $40\,\%$. For pâté, the initial compression force is an order of magnitude lower, and this sample does not show a maximum force during compression, but instead the force linearly rises up to strains $\sim 3\,\%$, as can be seen in the inset of Fig. 3.2, before entering the plastic regime, starting at strains larger than $20\,\%$. The compression force is transmitted mainly by the protein matrix, whereas the fat droplets contribute to a simple hydrodynamic reinforcement. The extended linear increment of the force for HME in the compression experiments corresponds thus to the extended LVR in the oscillatory amplitude sweep shown in Table 3.1. Additionally, the distinguished initial force increments during compression (see inset of Fig. 3.2)

reflects the overall difference in structure between foie gras and pâté. The foie gras show a slight strain hardening and an inflection point and supports the contribution of a large-scale fat network in the solid emulsion. Differences in the mechanical behavior of the FG samples can be explained by the differences in fat content and distribution as well as water content, as has also been observed for pâté samples[11]. With less water content (Table 3.1), higher total fat area and interconnected fat clusters, FG2 has a stronger fat network and stronger gel structure. This leads to an increase of G'_0 and the hardness. In opposition to both FG samples, HME does not have the fat network structuring component although a similar content of water and fat as FG1.

The correlation parameters presented in Table 3.2 provide a neat summary of the relationship between fat microstructure and mechanical properties of fatty liver-based emulsions. This analysis suggests that having smaller, rounder and smoother fat particles renders a softer gel-like emulsion, whereas the homogeneous distribution of larger, interconnected fat clusters provides a stronger structure.

3.5 Conclusions

Here, a comparative study on the texture and microstructure of fatty liver-based emulsions products was performed between two commercial brands of foie gras *bloc* and a homemade duck liver pâté. In terms of textural properties, the pâté prepared using spontaneously-fattened duck liver and rendered fat yielded a much softer texture compared to both commercial foie gras *bloc* products. This was evidenced by a significantly smaller hardness and initial storage modulus G'_0 of the pâté compared to the foie gras samples.

CARS microscopy was used as a robust, label-free tool to characterize fat distribution in these fatty liver-based emulsions. Comparatively, the pâté lacked an interconnected network of large fat clusters present in foie gras samples. On the contrary, pâté had a higher concentration of small, round particles. These differences at the microscopic level between liver-based emulsions strongly correlated with mechanical differences. Stronger, more brittle gel correlated with larger, connected clusters with irregular shape. Conversely, smaller, and smoother particles correlated with a softer texture.

The microstructural characterization performed on fatty liver-based emulsions provided deeper insight into the causes of the textural differences observed. Furthermore, the correlation established between fat distribution and mechanical properties will allow for improvement of pâté texture by tuning the microstructure to resemble that of foie gras. This can be achieved by adding, e.g., industrially-used food emulsifiers and/or liver-occurring proteins such as collagen, into the liver batter.

Supplementary Material

See supplementary material for the fat particle size distribution weighed by area of the foie gras *bloc* samples and homemade pâté.

Acknowledgments

The authors acknowledge the support from the Danish Molecular Biomedical Imaging Center (DaMBIC, University of Southern Denmark), where all imaging was performed. This work has been supported by the Villum Foundation, (Denmark) through its Villum Young Investigator Programme (M.P. Clausen, grant #00025414). M. Bächle was gratefully funded by VAN HEES GmBH, Walluf, Germany.

Authors contribution

M.A.V.: CARS imaging, image analysis, statistical analysis, manuscript draft; M.B.: sample preparation, texture analysis, rheology measurements; A.S.: supervision, providing materials and funding; T.A.V.: project idea, interpretation, model development, supervision, writing, manuscript review; M.P.C.: experimental design, interpretation, supervision, writing, manuscript review.

Data Availability Statement

Data available on request from the authors. The data that support the findings of this study are available from the corresponding author upon reasonable request.

Chapter 4

Function of different emulsifiers in spreadable meat emulsions: A systematic study of physical properties

Baechle, M.; Via, M. A.; Clausen, M. P.; Vilgis, T. A.

This chapter is a version of the manuscript published in *Food Biophysics* 20, 57 (2025) https://doi.org/10.1007/s11483-025-09941-2

Abstract

Emulsifiers are often used in the processing of pâtés based on various spreadable and solid meat products to maintain physical properties during production and to maintain the quality of the final product when key components, such as fat composition, are changed. Emulsifiers have been proven as useful tools to control and achieve desired properties in pâté-like products by modifying the product composition. This paper examines the impact of three distinct emulsifiers and stabilizers, namely collagen, sodium stearate and mono- and diglycerides (MDG), on the texture and microstructure of a range of duck liver pâtés. Samples with different emulsifier concentrations were analysed using methods such as rheology and texture analysis to gain insight into their mechanical properties. To visualize the microstructure of the emulsion, Coherent Antistokes Raman Scattering, together with image and statistical analysis, is used. Collagen increases the elastic properties, while sodium stearate significantly increases the hardness in compression tests. MDG only affects the microscopic properties. All emulsifiers exert discernible effects on the microscopic emulsion structure, fat particle sizes and shapes, as well as on mechanical properties. This allows for strategic use of these agents in order to enhance the quality and stability of meat emulsions.

4.1 Introduction

Spreadable meat products, for example liver sausages or pâtés, are protein-based emulsions [4]. The fat is dispersed in a protein matrix [10], with certain components demonstrating a high emulsifying capacity to maintain their stability under shear and temperature [6]. In many cases, this minimal number of ingredients is sufficient to guarantee their stability and spreading properties at a given protein to fat ratio. Together with salt and seasoning, high palatability of the final spreads can be achieved. Their sensory properties and the mouthfeel during oral processing are strongly influenced by physical properties, such as the low elastic response of the proteins involved, combined with the pastiness of the protein matrix, and most importantly by the size and distribution of the fat particles [128, 129].

In contrast, large-scale or industrial production requires well-defined processes for production and standardized and reproducible qualities. However, it should be noted that fat and liver are natural products which can vary significantly in composition, for example in terms of the fatty acids and/or the protein profile of the livers, see e.g.[130, 131]. This necessitates the use of additives to control and maintain the texture and physical properties, especially when animal fats are reduced or even replaced by plant-based oils. Consequently, processed meat products often contain technical additives such as various stabilizers emulsifiers, gelatin, or surfactants to control and adjust mechanical properties, including mouthfeel during oral processing [1, 132].

However, from a physical point of view, some ingredients in recipes of commercial processed meat products appear to be contradictory because of their competing interactions between different components and molecules. Even recent publications on products such as scalded sausages (Frankfurter) and meat-based spreads (liver sausage) lack systematic studies of the effect of different emulsifiers or other additives. Consequently, it is challenging to provide clearer insights regarding their impact on the structure and resulting properties. Examples of commonly used functional emulsifiers such as proteins, including those derived from connective tissue, sodium stearates and mono- and diglycerides. [132–143]. Nevertheless, it is not easily feasible to ascertain their direct physical impact, given the complexity of the systems described in the scientific literature. Colmenero [144] for example summarized, the impact of proteins of various sources, starch, cellulose or hydrocolloids of various meat products in view of fat reduction, to ensure empirically the emulsion stability and textural properties.

The endeavour to comprehend the molecular interplay through the application of fundamental principles of soft matter physics has been demonstrated to be advantageous. This has been evidenced by the consideration of meat alternatives for scaled sausages [145]. Such conceptual frameworks elucidated herein facilitates not only a comprehensive understanding of the molecular interplay, but also the proposition of practical modifications.

Indeed, pâtés composed of liver fat have proven useful in facilitating a more profound comprehension of the impact of stabilizers and surfactant additives. In this

particular instance, the formation of a "mean field" pâté composed of pure liver fat enables the examination of the effects of individually added additives on mechanical and structural properties.

Therefore, a systematic study of three different emulsifiers commonly used in food products is presented. The emulsifiers used in this study are collagen, sodium stearate and mono- and diglycerides of fatty acids (MDGs). These additives have been deliberately selected because of their distinctive physical, structural, and chemical properties. This permits the examination of model systems by focusing on the results at the molecular level. The substances in question were chosen to be water-soluble collagen [146], a long-chained protein; the charged sodium stearate, and polar MDG [147]. This choice ensures that the resulting physical properties are fundamentally distinct, including the ability to gel in a long-chain-like manner, and to provide elasticity at lengths scales between the fat droplets. Additionally, long-range electrostatic repulsions, and short-range polar interactions [134, 147, 148], from the two surfactants / emulsifiers provide different droplet distributions and droplet sizes.

The main idea for this investigation is to gain insight into the function and stability of each emulsifier in a well-defined model system, based on an identical matrix for all samples and experiments. The model system was a spreadable meat emulsion containing duck liver, rendered duck fat, salt, emulsifier and water. To facilitate a comparative analysis of the impact that distinct emulsifiers exert on the textural properties of pâtés, a range of physical parameters were estimated using methods that were systematically different.

To do so, the model pâtés are characterized macroscopically by rheology and compression experiments[1, 84, 149, 150]. In addition, it has been shown that it is useful to relate the textural properties to the meso- and microstructure, Ray et al. [151] imaged the microstructure of laboratory constructed and commercial liver paté using scanning electron microscopy. An attempt to image the emulsion structure of liver-based products with light microscopy was made by Tiensa et al. [11]. However, these techniques need invasive sample preparations. On the contrary, Coherent Anti-Stokes Raman Scattering microscopy (CARS-Microscopy) [152–155] has been proven to be non-invasive and provides clear information of the microscopic structure. Consequently, macroscopic properties can be more effectively integrated with microscopic structures by utilizing appropriate data derived from image analysis of the CARS results.

4.2 Materials and Methods

4.2.1 Materials

The liver-fat-matrix, common to all samples used from duck liver (supplied by Leon Dupont, Notre Dame de Riez, France) and rendered duck fat (supplied by Bruno Siebert, Ergersheim, France), NaCl (AnalaR NORMAPUR, VWR Chemicals, Darmstadt, Germany). Food grade collagen, mono- and diglycerides, and sodium stearate (provided by VANHEES GmbH, Walluf, Germany) have been added accordingly.

4.2.2 Meat emulsions preparation

The general process for preparing pâté emulsions has been outlined in a prior study [155]. For clarity and convenience, a concise overview is provided below. The emulsifiers, listed in Table 4.1 were soaked in 90 g of the water used for the preparation, and the mixtures were heated to 60 °C in a controlled water bath before emulsion preparation. All ingredients, duck liver, rendered duck fat, emulsifier, water and sodium chloride

Table 4.1: Used emulsifiers concentrations for each sample with identical matix.

Emulsifier	Concentration		
Collagen	5 g/kg	10 g/kg	15 g/kg
Mono/Diglycerides	5 g/kg	10 g/kg	15 g/kg
Sodium Stearate	10 g/kg	20 g/kg	30 g/kg

in the amounts listed in the table 4.2 to produce the emulsion. The liver was minced in two stages using a Hallde VCB-62 food processor (AB Hallde Maskiner, Kista, Sweden). The initial mincing stage operated for 5 s at 1500 rpm, following a 10 s stage at 3000 rpm. The resulting liver paste was then salted. Afterwards, Liver, fat, water-emulsifier mixture and remaining water were emulsified in two steps: a) at 1500 rpm for 15 s, and b) at 3000 rpm for 30 s. These steps were repeated once, and Liquid nitrogen (50 mL to 100 mL) was introduced between steps to regulate the temperature.

Table 4.2: Quantities of components used to prepare the sample matrix.

	Concentration					
Components	0 %	0.5 %	1.0 %	1.5 %	2.0 %	3.0 %
Emulsifier/g/kg	0	5	10	15	20	30
Liver/g/kg	490.0	487.5	485.0	482.5	480.0 g	475.0
Fat/g/kg	392	390	388	386	384	380
Water/g/kg	98.0	97.5	97.0	96.5	96.0	95.0
Salt/g/kg	20	20	20	20	20 g	20

After degassing, the emulsion was transferred to plastic containers and cooked in a preheated water bath (Julabo ME 4, JULABO GmbH, Seelbach, Germany) at 80 °C for 120 min. The cooked samples were then cooled and stored at 5 °C in a refrigerator. Each emulsifier series was prepared 3 times including a control sample (Control: n=9; each concentration: n=3).

4.2.3 Rheological experiments

Rheological testing was carried out on a Gemini 200 rheometer (Bohlin Instruments, Malvern Panalytical Ltd., Malvern, UK) as detailed in [155]. To minimize slippage, the parallel-plate setup was lined with 60-grit sandpaper. Samples were prepared using a circular cutter (25 mm diameter), sliced to a uniform thickness, and positioned under the rheometer plates. Gap sizes have been adapted until detecting the value 2 N for

the normal force, which corresponds to gap heights between 1150 µm and 1750 µm. The unheated samples were spread into a 1000 µm thick mould and gap size was set accordingly. After an equilibration time for 5 min, amplitude sweeps were carried out (strain: 0.01 % to 200 %; frequency: 1 Hz; temperature: 5 °C). Measurements were repeated at least three times per sample. The strain at which G' deviated 10 % from its initial value (G'_0) was set as the linear elastic regime (LVR), while the flow point was identified where G' equaled G''.

4.2.4 Texture Analysis

The samples were evaluated through the utilization of a ZwickRoell AllroundLine Z005 Universal Testing Machine (ZwickRoell GmbH, Ulm, Germany), in accordance with the methodology delineated by Bourne [156]. The cylindrical samples (diameter: 25 mm; height: 20 mm) were subjected to compression tests conducted in two cycles utilizing a 75 mm aluminum disc probe. The compression speed was set to 1 mm/s until it reached 75 % deformation (relative to the sample height). Each specimen, cooled to 5 °C, was tested six times at room temperature. Hardness was determined as the maximum force recorded, whereas the initial slope was quantified by applying linear regression to the compression curve (5 points after 0.01 % strain threshold).

4.2.5 CARS Microscopy and image analysis

Imaging was carried out in combination with a Leica SP8 Coherent Anti-Stokes Raman Scattering (CARS) microscope (Leica Microsystems GmbH, Mannheim, Germany) by using a picoEmerald multi-photon laser (APE, Berlin, Germany) as luminous source and Epi-mode detection (non-descanned photomultiplier tube (PMT) detector; 650/210 BrightLine HC filter (AHF Analysentechnik AG, Tübingen, Germany)). Imaging was conducted at room temperature with a Leica 40× HC PL IRAPO objective (NA 1.10). To excite the symmetric -CH_2 stretching mode (2845/cm), which allows fat visualization in the samples, the wave lengths of the lasers were tuned (Stokes: $\lambda_{\omega 2}$ =1064.5 nm; Pump: $\lambda_{\omega 1}$ =817 nm) and with the laser intensity adjusted to keep signal levels approximately 20 % below signal saturation. For imaging, sectioned pâté samples were transformed in a suitable 8-well #1.5 glass bottom chamber (Ibidi GmbH, Gräfelfing, Germany). 1928 × 1928 image pixels with a 0.15 µm pixel resolution, were captured at a depth of 5 µm. 5 regions of interest per sample were imaged, yielding 15 images in total, as triplicates were prepared for each sample type, similar to the approach used in [155].

Image analysis was conducted using *Fiji* software.[119] Binary images were created by applying the Huang thresholding algorithm.[120] Particles smaller than the resolution limit were excluded from the analysis as noise, and particles with incomplete edges within the frame were omitted. Key parameters analysed included the individual particle areas, the total area occupied by particles, particle perimeter, aspect ratio, and circularity. The *aspect ratio* (AR) represents the ratio of an ellipse's major axis to

its minor axis fitted to each particle, where AR=1 indicates a perfect circle, and larger values signify increasing deviations. *Circularity*, a measure of smoothness, compares the particle's area to its perimeter, with values ranging from 0 (high surface roughness) to 1 (a perfect circle).

4.2.6 Statistical Analysis

Each measured value of an emulsifier test series was tested separately for statistical significance, performing an analysis of variance (ANOVA) using DATAtab (DATAtab: Online Statistics Calculator. DATAtab e.U. Graz, Austria. URL https://datatab.de). Each sample in a series was tested for statistical significance against other samples using Bonferroni post-hoc tests based on ANOVA. Corresponding values of unheated and heated samples were tested for statistical significance using the t-test. A significance level of 5 % ($\alpha = 0.05$) was employed for all tests.

4.3 Results

4.3.1 Mechanical properties

Mechanical data for the various pâtés were evaluated and comparing by amplitude sweeps providing storage, loss moduli (G', G''), linear viscoelastic ranges (LVR), and the flow points. The plots of amplitude sweeps of unheated and heated samples for the different stabilizers and emulsifiers are shown in Fig. 4.1. All unheated emulsions appear very soft and viscous, as indicated by the gradual decrease of G' and G'' at higher deformations >1 %. This suggests that the application of heat to the samples results in the formation of a solidified material, achieved through the cross-linking of proteins present in the liver matrix [155]. This will be discussed later in more detail.

The initial storage modulus G' appears for all samples higher as the loss modulus G''. This can be addressed to the highly viscoelastic nature of the matrix. However, since the experiments are carried out at temperatures $T = 5\,°\mathrm{C}$, the solid nature at low deformations can be addressed to the contribution of the fat particles with high solid fat content, as the partially crystalline fats acts as solid filler particles, which enhance the modulus in general [11, 125].

The soft and viscous nature expresses itself at the very low flow points, where $G' = G''$, which are, in general, lower as the flow points of the heated sample. In addition, all initial moduli (G' at low deformation amplitudes) are at least on order of magnitude lower as the heated emulsions, which can be addressed to the cross-linking of the liver and sarcoplasmic proteins forming the matrix. The change of the low deformation modulus (G'_0) during heating is shown in Fig. 4.2 for convenience. Compression tests for heated samples are shown in the top row of Fig. 4.3. All parameters for the measurements with different emulsifier concentrations are given in Table 4.3.

Control Pâté without additive

To investigate the influence of the different emulsifiers systemically, a pâté without additives was prepared and analysed as well. For the raw samples the initial G' value was estimated and is 8.666 ± 11.266 Pa and the LVR of the unheated samples is 0.24 ± 0.16 % (see Fig 4.1). For the heated pâté the initial G' increases to 117.959 ± 16.248 Pa (Fig. 4.1) and the LVR raises to 0.41 ± 0.05 %. In addition, for the heated samples also the flow point with 39.59 ± 3.65 % strain were estimated as shown in Table 4.3. In the texture analysis measurements, the plain pâté reached a hardness of 13.18 ± 3.57 N at a compression strain of 32.44 ± 3.67 %. The curves showed an initial slope of 0.43 ± 0.16 (Fig. 4.3 and Table 4.3).

TABLE 4.3: Mechanical properties of pâté preparations with collagen, sodium stearate and MDG (n=3) and control (n=9). Superscript letters: a: **Statistically significant due to ANOVA**; b-l: Statistically significant pair based on Bonferroni Post-hoc-Tests; m: Outliers removed based on Grubbs-Test; n: Values statistically significant due to t-test.

Sample	**Conc.**	**G′**(heated)^{d}/Pa	**G′**(unh.)^{d}/Pa	**LVR**(heated)/%	**LVR**(unh.)/%	**Flow point**/%	**Force**/N	**Compression**/%	**Initial slope**
Control	0.0 %	117,959 ± 16,248	8,666 ± 11,266^{a}	0.41 ± 0.05^{a,c,m,n}	0.24 ± 0.16^{n}	39.59 ± 3.65	13.18 ± 3.57$^{a,d,f-h,m}$	32.44 ± 3.67$^{a,e,j-l}$	0.43 ± 0.16
	0.5%	133,266 ± 8,050	13,717 ± 15,809^{a}	0.44 ± 0.06^{a,n}	0.18 ± 0.09^{n}	43.32 ± 3.33	33.75 ± 13.43^{a}	40.67 ± 4.74^{a}	0.54 ± 0.24
Collagen	1.0%	123,543 + 11,577	26,361 ± 15,169^{a}	0.50 ± 0.03^{a,n}	0.17 ± 0.00^{n}	39.06 ± 7.02	34.54 ± 11.89^{a}	42.05 ± 4.55^{a}	0.36 ± 0.07
	1.5%	125,357 ± 4,114	35,612 ± 3,296^{a,c}	0.72 ± 0.15^{a,b,n}	0.20 ± 0.03^{n}	39.30 ± 9.10	39.60 ± 12.24^{a,d}	44.68 ± 2,07^{a,e}	0.38 ± 0.11
	1.0%	148,462 ± 13,274	18,711 ± 11,349	0.43 ± 0.01	0.32 ± 0.13	40.51 ± 8.86	29.64 ± 5.54^{a,f,i}	41.67 ± 3.71^{a,j}	0.43 ± 0.05
Stearate	2.0%	136,586 + 5569	19,154 ± 10,400	0.43 ± 0.01^{n}	0.26 ± 0.04^{n}	46.30 ± 4.77	39.53 ± 8.09^{a,g}	42.84 ± 2.90^{a,k}	0.51 ± 0.07
	3.0%	131,784 ± 3,053	25,526 ± 10,166	0.47 ± 0.04	0.32 ± 0.12	41.40 ± 4.74	53.75 ± 10.41^{a,h,i}	50.27 ± 2.72^{a,l}	0.49 ± 0.10
	0.5%	130,128 ± 7,245	21,883 ± 7,946	0.34 ± 0.01^{n}	0.18 ± 0.03^{n}	40.04 ± 3.72	15.78 ± 2.08	33.38 ± 0.79	0.49 ± 0.02
MDG	1.0%	133,964 + 15,872	16,069 ± 9,584	0.34 ± 0.09	0.21 ± 0.08	42.55 ± 1.46	13.84 ± 1.90	30.04 ± 1.33	0.44 ± 0.13
	1.5%	140,109 ± 9,433	12,115 ± 2,782	0.36 ± 0.07	0.39 ± 0.18	44.37 ± 7.14	14.58 ± 1.19	31.63 ± 0.92	0.38 ± 0.03

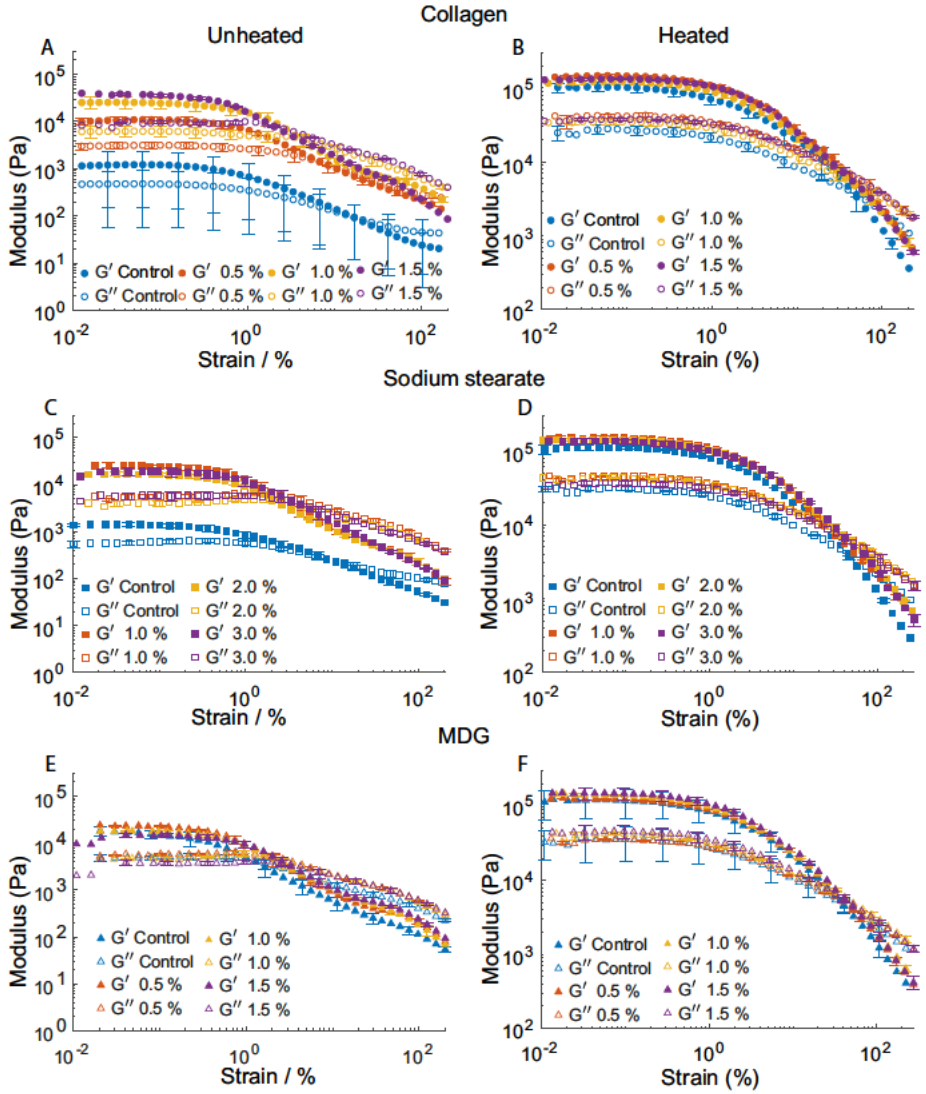

FIGURE 4.1: Results of amplitude sweeps of unheated (left side; Panel A: collagen; Panel C: sodium stearate; Panel E: MDG) and heated Pâtés (right side; Panel B: collagen; Panel D: sodium stearate; Panel F: MDG) with different emulsifiers and concentrations(blue: Control; red: collagen, MDG: 0.5 %, stearate: 1.0 %; yellow: collagen, MDG: 1.0 %, stearate:2.0 %; purple: collagen, MDG: 1.5 %, stearate: 1.0 %). The mean curves of an example measurements are shown.

Mechanical behaviour of pâté samples prepared with collagen

Unheated samples supplemented with collagen showed a statistically significant increase in G', from 8.666 ± 11.266 Pa for the control sample to 35.612 ± 3.296 Pa for samples prepared with 1.5 % collagen. The LVR-Values are not significantly different to each other and compared to the control sample, and scatter from 0.17 % to 0.20 %, as shown in Fig 4.1 and Table 4.3. The increase of the storage modulus of unheated emulsions

with increasing collagen concentration can be addressed to the increasing interaction between all thermodynamically compatible proteins.

The initial modulus of heated samples imply an increase to 133.266 ± 8.050 Pa with 0.5 % collagen concentration, and remained then relatively constant with increasing concentration, but it is not statistically significant. The LVR increased significant with higher collagen concentrations in the pâté samples, peaking at 0.72 ± 0.15 % strain and showing an overall increase, which is statistically significant, when compared to the unheated samples (see Table 4.3). The flow point, where G'' surpasses G', are not changing significant as well as the G' values. The sample with 0.5 % collagen showed the highest value of 43.32 ± 3.33 %. For the other pâtés the values were slightly lower, hovering around 39%. Force measurements for collagen-prepared samples showed a significant steep increase in measured compressive force, from 13.18 ± 3.57 N for the control sample to 33.75 ± 13.43 N for samples containing 0.5 % collagen. Higher collagen concentrations resulted in only a slight increase in the force required, reaching a maximum of 39.60 ± 12.24 N for a 1.5 % collagen concentration. A similar statistically significant trend was observed in the compression strain at maximum force, with a steep increase from 32.44 ± 3.67 % for the control samples to 40.67 ± 4.74 % for 0.5 % collagen concentration, a peak at 44.68 ± 2.07 % for samples containing 1.5 % collagen (see Table 4.3).

Mechanical properties of pâté samples with sodium stearate

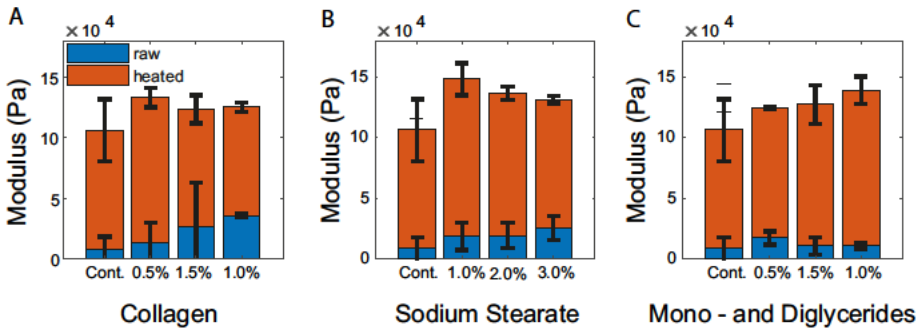

FIGURE 4.2: Initial shear modulus, G'_0, of the unheated (blue) and heated (red) emulsions for the three different types of emulsifiers (Panel A: Collagen; Panel B: Sodium stearate; Panel C: MDG).

For the unheated samples, G' increased with the sodium stearate concentration, ranging from 8.666 ± 11.266 Pa for control pâté to 25.526 ± 10.166 Pa for the highest concentration of sodium stearate is implied, but is not statistically significant. The LVR of the unheated samples is with max. 0.32 % (1 % and 3 % stearate) not significant affected (see Fig. 4.1).

In contrast, the heated samples showed an overall increase with addition of stearate, reaching a maximum G' of 148.462 ± 13.274 Pa at 1.0% sodium stearate. With a subsequent decrease in G' to higher concentrations, reaching 131.784 ± 3.053 Pa for 3 % sodium stearate, as shown in Fig 4.2. For all concentrations, the LVR remained

almost constant, with differences of only 0.43 % (1 % and 2 % sodium stearate) to 0.47 % observed for pâté prepared with 3 % emulsifier (see Table 4.3). Regarding the flow point, an increase was observed with the emulsifier concentration, ranging from 39.59 ± 3.65 % to 46.30 ± 4.77 % for the first three samples. However, for the pâté prepared with 3 % sodium stearate, the value was lower at 41.40 ± 4.74 % compared to the other samples. Though, none of the values show a statistically significant trend. A significant increase in the measured force with increasing sodium stearate concentration was observed. The lowest force values were recorded at 13.18 ± 3.57 N for the control pâté, while the highest force, reaching 53.75 ± 10.41 N, was observed for samples containing 3.0 % sodium stearate. This trend was paralleled by the compression strain values, which increased statistically significant in accordance with the force values. These ranged from 32.44 ± 3.67 % for the control sample to 50.27 ± 2.72 % for the highest concentration of 3.0 % (see Table 4.3 and Fig 4.3).

Mechanical properties of pâté samples with mono- di- and triglycerides

In contrast to the unheated systems with added collagen and sodium stearate, the dynamic storage modulus (G') of unheated samples imply a decrease with increasing MDG concentration, starting at 21.883 ± 7.946 Pa for 0.5 % MDG and decreasing to 12.115 ± 2.782 Pa for 1.5 % MDG. The LVR values of the unheated samples are in the range of the control, except the 1.5 % concentration value, which is 0.39 ± 0.18 % (see Table 4.3). Conversely, for heated samples, G' showed only little variations with increasing MDG concentration. The maximum G' was reached at 1.5 % MDG and measured 140.109 ± 9.433 Pa, with a minimum value of approximately 130.000 Pa observed for the samples containing 0.5 % MDG. Similar to the sodium stearate samples, the LVR remained relatively constant over the entire concentration range, ranging from 0.33 ± 0.08 % to 0.36 ± 0.07 % and increased slightly during heating.

As shown in Table 4.3, rheological properties, such as amplitude sweeps, demonstrate certain trends in the behaviour of the various emulsifiers. However, the statistical significance of these trends is limited according to the tests. It is therefore necessary to conduct further experiments with larger amplitudes. Consequently, compression tests were conducted. These experiments indicated that the force and strain values are within a similar range for all measurements, ranging from 13.84 ± 1.90 N to 15.78 ± 2.08 N for maximum force and from 30.04 % to 33.38 % strain, with no apparent order (see Table 4.3). All values show no significant trend for this type of emulsifier.

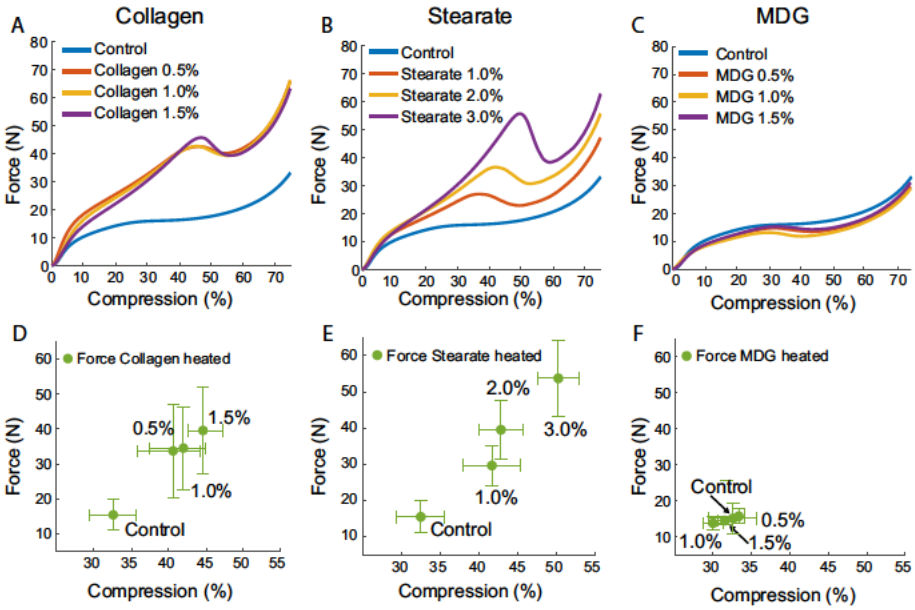

FIGURE 4.3: Force measurements of the cooked pâté samples with different emulsifiers. The first row shows the mean of an example measurement of the different series (Panel A: Collagen; Panel B: Sodium stearate; Panel C: MDG) (blue: Control; red: collagen, MDG: 0.5 %, stearate: 1.0 %; yellow: collagen, MDG: 1.0 %, stearate: 2.0 %; purple: collagen, MDG: 1.5 %, stearate: 3.0 %). The second row shows the mean force values plotted against the strain values of the heated samples (Panel D: Collagen; Panel E: Sodium stearate; Panel F: MDG).

4.3.2 Comparison of mechanical properties between the emulsifiers

The results of the texture analysis measurement (Fig. 4.3) show a similar behaviour, although the maximum force and strain is different for each sample. In the first 10 % of deformation, the slope of the curve is much steeper for all samples. Subsequently, the force increases with a reduced gradient until the maximum force is attained. The fat particles move in relation to one another, and the network undergoes tensile strain until the samples begin to fracture and disintegrate at the maximum force. The second increase in force is accompanied by plastic deformation of the samples between the plate and the probe. For the sodium stearate samples, the maximum force had the largest increase (29.6 N to 53.8 N) of all samples in combination with the largest shift of the maximum from 41.7 % to 50.3 %. For the MDG samples behaviour is not so pronounced, the maximum force and peak position in the same range for all samples: 15 N to 20 N and 30 % to 35 % (see Fig. 4.3).

The observations concerning the collagen / gelatin enriched samples support the conclusions obtained from the amplitude sweeps. The 0.5 % sample shows the highest low deformation modulus, the 1.5 % the lowest, apart from the control sample. Low collagen concentration increase are less disturbed by the protein cross-linking of the matrix, whereas large concentrations of collagen gel need to compete with the permanently cross-linked liver protein network which forms under heating. Local phase separations of collagen network under cooling lower the modulus at smaller

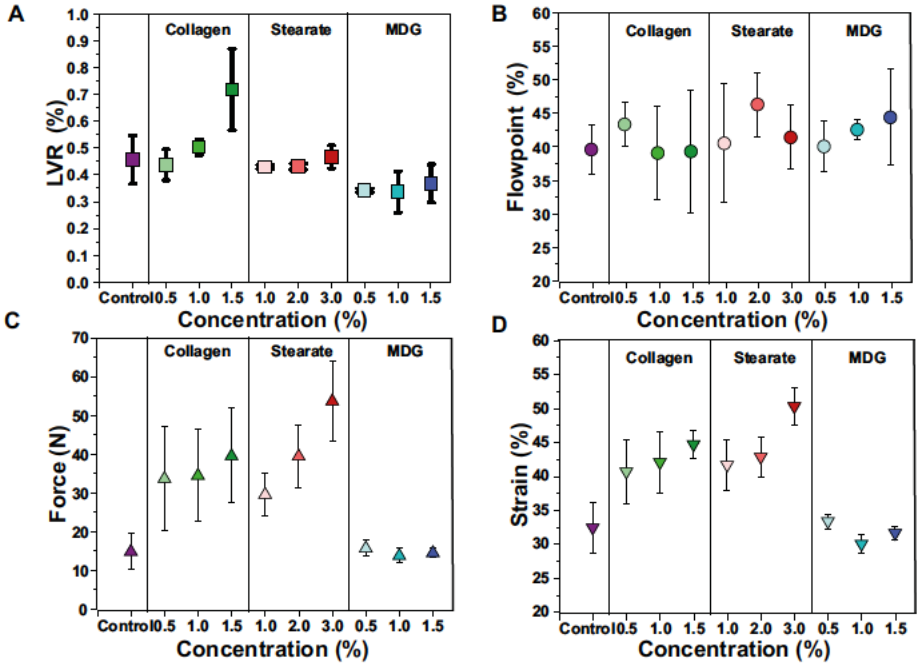

FIGURE 4.4: LVR against concentration shown in squares, (A); flow point against concentration (circles), (B); force against concentration shown in upwards triangles, (C); strain at maximum force against concentration (downwards triangles) (D). Control: purple; collagen: 0.5 %: light green, 1.0 % medium green, 1.5 %: dark green; sodium stearate: 1.0 %: light red, 2.0 %: medium red, 3.0 %: dark red; MDG: 0.5 %: light blue, 1.0 % medium blue, 1.5 %: dark blue.

deformations. At deformations about 40 45% collagen networks "squeeze" out from the matrix, which is indicated by the "peak" in the force, which is pronounced more at higher gelatin concentrations. The shift of this peak is small, and it mainly remains roughly at similar deformations (see Fig. 4.4).

4.3.3 CARS microscopy and image analysis

In this section, we investigate the correlation between the mechanical differences and the microstructure of emulsified fat in samples containing varying emulsifiers. The aim is to obtain a better understanding of the relationship using CARS microscopy for visualizing the fat particles and their distribution as shown in Fig. 4.5. Several images were collected from both unheated and heated samples at various locations, all exhibiting a distinct contrast between the fat phase (red) and the continuous water and continuous protein phases (black).

A preliminary observation suggests that the samples exhibit a comparable distribution of fat particles; however, upon closer examination, substantial differences in the size, shape, and quantity of fat particles are apparent. To facilitate a systematic comparison of the samples, image analysis of the particles was conducted. The analysis obtained the size of each particle in the images, including area and perimeter. The box plots in Fig. 4.6 show the mean and median particle sizes of the unheated and heated samples. To facilitate comparisons between the samples, we calculated the

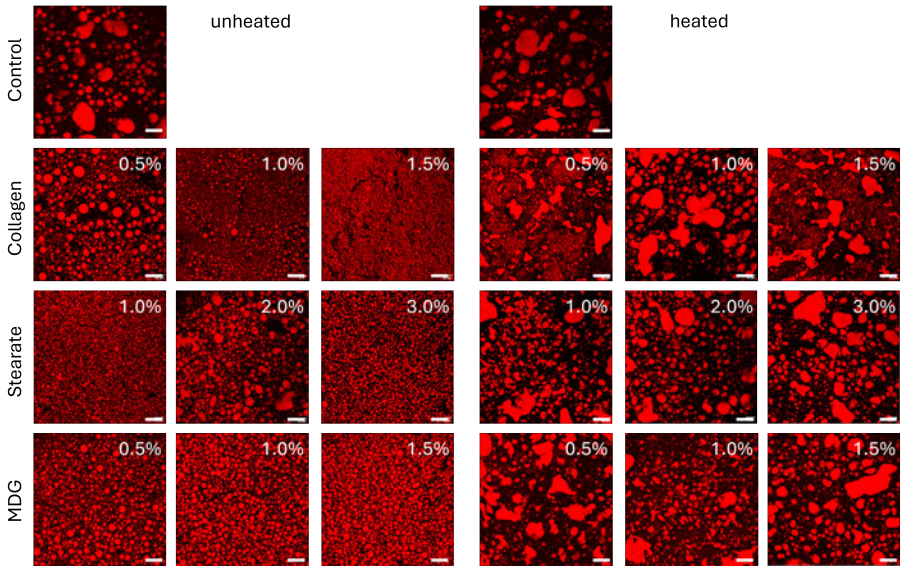

FIGURE 4.5: Images of the emulsion structure of unheated (left side) and heated samples (right side) obtained by CARS microscopy. Each row shows a different emulsifier in increasing concentration. The pictures are only shown as an example and do not reflect any statistical significant. The scale bar in each image is equal to 50 µm

relative frequency of each group by dividing the area covered by particles in a given size range by the total area covered by fat in the samples, the results are shown in Fig. 4.7. Morphological descriptors as circularity and aspect ratio are calculated as well. Below are the results of each series found in Fig. 4.8 and Table 4.5.

Pâté without any additives

Overall, the particles in the unheated control sample have a mean size of $35.90 \pm 225.46\,\mu m^2$ and the median size is at $1.2\,\mu m^2$. For the heated sample, the mean size decreases to $25.3 \pm 384.1\,\mu m^2$ and the median increases slightly to $1.5\,\mu m^2$ (see Table 4.4). For the heated control pâté a broad distribution is found over almost all size ranges, which causes the high standard deviation of the mean area. The distribution is dominated by particles with a surface area greater than $10.000\,\mu m^2$, which account for approximately 25 % of the total fat area. However, this is only due to a few relatively large particles. Furthermore, the distribution ranges from particles smaller than $1\,\mu m^2$ up to $8000\,\mu m^2$ with coverage of 3 % to 10 % in each case. Exceptions are particles with a size between $100\,\mu m^2$ and $500\,\mu m^2$ covering 16 % of the total fat area (Fig. 4.7 A). The mean aspect ratio for the heated and unheated samples were determined to 1.47 ± 0.51 and 1.49 ± 0.61. The circularity of the heated and unheated values are 0.84 ± 0.20 and 0.84 ± 0.19 (see Table 4.5 and Fig. 4.8). The average interparticle distance for the control sample remained practically constant during heating, with a small increase from $3.2 \pm 2.4\,\mu m$ to $3.5 \pm 2.4\,\mu m$ (see Table 4.4).

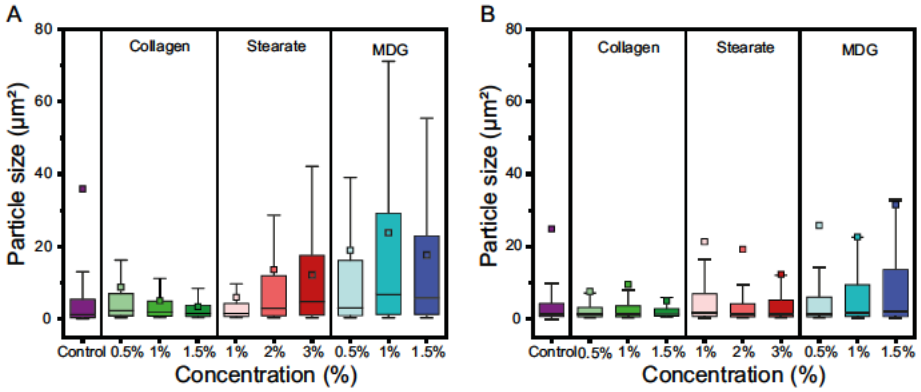

FIGURE 4.6: Box plots of the particle sizes for each sample. The boxes indicate the sizes of particles between the first and third quartile (25 % to 75 %) and the corresponding median is drawn as a line in the boxes. The whiskers indicate 1.5 times the quartil distance. The mean particle sizes are indicated by squares. Panel A shows unheatead, B heated samples with the following colors: Control: purple; collagen: 0.5 %: light green, 1.0 % medium green, 1.5 %: dark green; sodium stearate: 1.0 %: light red, 2.0 %: medium red, 3.0 %: dark red; MDG: 0.5 %: light blue, 1.0 % medium blue, 1.5 %: dark blue.

TABLE 4.4: Mean particle sizes, median of particle area, and average distances between fat particles in heated and unheated samples.

Sample	**Conc.**	**Mean area/µm²**		**Median area/µm²**		**Average distance/µm**	
		heated	unheated	heated	unheated	heated	unheated
Control	0.0 %	25.3 ± 384.1^{b}	35.9 ± 225.46	1.5	1.2	3.5 ± 2.4	3.2 ± 2.4
Collagen	0.5 %	7.6 ± 86.2^{d}	8.8 ± 24.8	1.3	2.3	1.9 ± 1.2^{m}	1.8 ± 1.0^{m}
	1.0 %	9.5 ± 108.1^{d}	5.0 ± 11.5	1.4	1.8	1.5 ± 0.8	1.1 ± 0.6^{j}
	1.5 %	4.8 ± 45.28	3.4 ± 7.05	1.1	1.5	1.2 ± 1.1	1.0 ± 0.6^{j}
Stearate	1.0 %	$21.3 \pm 98.7^{c,b}$	6.0 ± 21.7	1.7	1.5	2.8 ± 1.9^{f}	2.0 ± 1.2^{k}
	2.0 %	19.2 ± 166.2^{c}	13.6 ± 31.4	1.3	3.0	2.5 ± 1.6^{f}	2.2 ± 1.3^{k}
	3.0 %	12.3 ± 60.9^{m}	12.1 ± 18.1^{m}	1.4	4.8	2.0 ± 1.0	1.6 ± 1.0
MDG	0.5 %	25.8 ± 121.2^{a}	19.0 ± 40.8^{e}	1.5	3.0	$2.7 \pm 1.9^{g,h}$	2.0 ± 1.3^{l}
	1.0 %	$22.7 \pm 97.8^{a,m}$	23.8 ± 48.13^{m}	1.8	6.7	$2.8 \pm 1.9^{g,i}$	2.1 ± 1.4^{l}
	1.5 %	31.6 ± 149.7^{a}	17.7 ± 31.3^{e}	2.1	5.8	$2.6 \pm 2.1^{h,i}$	1.6 ± 1.2

[a] **Series shows no statistically significant differences according ANOVA**
[b–l] Values pairs are not statistically significant different, due to Bonferroni-Post-Hoc-tests
[m]: Value pairs of heated and unheated samples are not statistically signifanct different due to t-test.

Collagen

The analysis of the collagen samples exhibited a significant decrease in the mean particle size for the unheated samples with increasing collagen concentration, from $8.8 \pm 24.8\,\mu m^2$ to $3.40 \pm 7.05\,\mu m^2$. The median for the unheated and also the heated samples is between $1.1\,\mu m^2$ and $2.3\,\mu m^2$ as shown in Table 4.4. No trend in particle size with increasing concentration is observed for the heated samples. However, a general statistically significant reduction in mean particle size is evident (see Fig. 4.6).

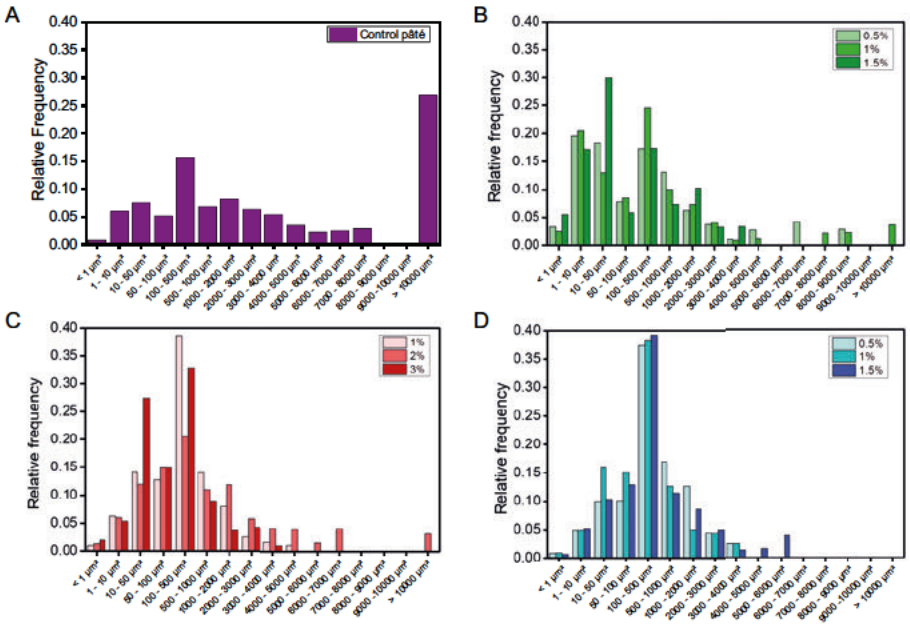

FIGURE 4.7: Illustration of the particle size distribution of distinct emulsifier series. The graphs present the area-weighted distribution of particle sizes, which is the fraction of the total fat area occupied by particles within a specific size group. The distribution for the control sample is shown in Panel A. Part B presents the relative frequencies of different particle sizes for varying collagen concentrations. 0.5 % collagen is shown in light green. Medium green shows 1.0 % collagen samples, and dark green shows 1.5 % collagen samples. Part C shows the relative frequencies of different sodium stearate samples. Concentrations from 1.0 % to 3.0 % are marked in light, medium and dark red. Panel D shows analogous relative frequencies of particle sizes for MDG samples and different concentrations are marked in light (0.5 %), medium (1.0 %) and dark blue (1.0 %).

The heated samples, revealed a broad distribution of particle sizes across all concentrations. The largest size groups over all samples are $1\,\mu m^2$ to $10\,\mu m^2$, $10\,\mu m^2$ to $50\,\mu m^2$ and $100\,\mu m^2$ to $500\,\mu m^2$. In the 0.5 % sample, the greatest area occupied by particles with dimensions between $1\,\mu m^2$ and $10\,\mu m^2$. The greatest area in the 1.0 % collagen sample is covered by particles with a size between $100\,\mu m^2$ and $500\,\mu m^2$. In the sample with 1.5 % collagen, particles with a size of $10\,\mu m^2$ to $50\,\mu m^2$ covers an area of 30 %. The 1.5 % sample shows the narrowest distribution of the collagen samples with a maximum particle size of $4000\,\mu m^2$. The remaining collagen samples exhibits particle sizes larger than $8000\,\mu m^2$, as shown in Fig. 4.7 B. An overview of the impact

of heating is provided in the Fig. A.2 of the supplementary information. All measured shape descriptors for the collagen series undergo a significant change. The aspect ratio of the unheated samples increases with concentration from 1.41 ± 0.45 to 1.46 ± 0.46 and remains below the control. The aspect ratio increases slightly with heating to 1.6 for all samples and exceeds that of the control (see Table 4.5). The circularity of the particles shows an upward trend with increasing collagen concentration for both heated and unheated samples, ranging from 0.63 ± 0.21 to 0.69 ± 0.21 (Fig. 4.8). The mean distances between particles decrease with increasing collagen content for both heated and unheated state (approximately 1.9 µm to 1.2 µm, Table 4.4). Except for the 0.5 % collagen sample, the average distance between particles increases significant during heating.

Sodium stearate

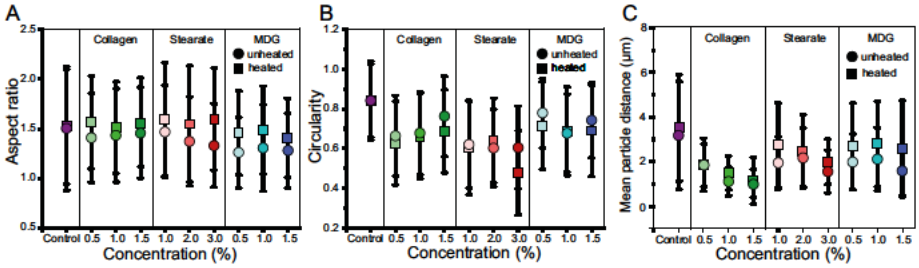

FIGURE 4.8: In panel A are the aspect ratio values from all samples shown. Circles show the values for unheated samples, and squares show the values for heated samples. In the same way are the circularity values displayed in panel B and the average distances of the heated and unheated samples in Panel C. (Control: purple; collagen: 0.5 %: light green, 1.0 % medium green, 1.5 %: dark green; sodium stearate: 1.0 %: light red, 2.0 %: medium red, 3.0 %: dark red; MDG: 0.5 %: light blue, 1.0 % medium blue, 1.5 %: dark blue.).

An analysis of the stearate samples revealed an significant increase in the mean particle sizes of the unheated samples with a further addition of stearate from $6.0 \pm 21.7\,\mu m^2$ for 1.0 % stearate concentration to $13.6 \pm 31.4\,\mu m^2$ for 2.0 % respectively $12.1 \pm 18.1\,\mu m^2$ for 3.0 % stearate concentration. The median size of the unheated samples increases accordingly to the stearate concentration, from $1.1\,\mu m^2$ to $4.8\,\mu m^2$. During heating, the mean particle sizes increase significant, compared to the unheated samples, for the lower concentrated samples, with $21.3 \pm 98.7\,\mu m^2$ for 1 % and $19.2 \pm 166.2\,\mu m^2$ for 2.0 % stearate but not for the 3.0 % sample. The mean area decreases for the heated samples with increasing concentration, but only the highest concentrations are significant different to the control. Whereas, the median remains by approximately $1.3\,\mu m^2$ to $1.7\,\mu m^2$ after heating and experiences a slight decrease (Table 4.4 and Fig. 4.6).

Consistent with previous observations, we found a broad distribution of particle sizes for the heated samples across the range of concentrations. The most prominent size groups over all concentrations are $10\,\mu m^2$ to $50\,\mu m^2$, $50\,\mu m^2$ to $100\,\mu m^2$ and $100\,\mu m^2$

TABLE 4.5: Aspect ratio and circularity of heated and unheated samples. **All series are statistically significant according ANOVA.** Heated and unheated values are significant different due to t-test.

Sample	**Conc.**	**Aspect ratio**		**Circularity**	
		heated	unheated	heated	unheated
Control	0.0 %	1.47 ± 0.54^{a}	1.49 ± 0.61	0.84 ± 0.20	0.84 ± 0.19
Collagen	0.5 %	1.57 ± 0.47^{b}	1.41 ± 0.45	0.63 ± 0.21	0.66 ± 0.20
	1.0 %	1.51 ± 0.46	1.43 ± 0.47	0.66 ± 0.22	0.68 ± 0.21
	1.5 %	1.57 ± 0.45^{b}	1.46 ± 0.46	0.69 ± 0.21	0.76 ± 0.20
Stearate	1.0 %	1.59 ± 0.57^{c}	1.47 ± 0.46	0.60 ± 0.24	0.62 ± 0.22
	2.0 %	1.55 ± 0.58	1.37 ± 0.45	0.64 ± 0.21	0.60 ± 0.19^{e}
	3.0 %	1.60 ± 0.51^{c}	1.33 ± 0.42	0.48 ± 0.21	0.60 ± 0.21^{e}
MDG	0.5 %	1.47 ± 0.42^{a}	1.26 ± 0.36	0.71 ± 0.22	0.78 ± 0.22
	1.0 %	1.46 ± 0.44	1.31 ± 0.43	0.69 ± 0.22^{d}	0.68 ± 0.20
	1.5 %	1.41 ± 0.40	1.28 ± 0.38	0.69 ± 0.23^{d}	0.74 ± 0.19

$^{a-e}$ Values with the same superscript letter are not statistically significant different, due to Bonferroni-Post-Hoc-tests.

to 500 µm^2. Whereas the most area is covered in all samples by particles between 100 µm^2 and 500 µm^2. A difference is noticed for the sample with 2.0 % stearate, since the second-largest area coverage is by fat particles between 50 µm^2 and 100 µm^2. In contrast to the other two samples, where particles between 10 µm^2 and 50 µm^2 cover the second-largest area. Similarly, the overall distribution is broadened for the 2.0 % sample comprising particles with sizes exceeding 10 000 µm^2 in comparison to approximately 4000 µm^2 for the remaining samples (compare Fig 4.7 C). A comprehensive illustration of the alterations in particle distribution during the heating process is presented in Fig. A.3 of the supplementary information. The aspect ratio of the particles showed a statistically significant elongation during the cooking process in all samples. In their unheated form, the particles exhibited a significant more rounded shape, with increasing concentrations leading to a shift from 1.47 ± 0.46 to 1.33 ± 0.42. For the case of the heated samples, the aspect ratio remained constant with around 1.6 for all concentrations (see Table 4.5), showing a significant elongation of the particles compared to the control. In general, the sodium stearate samples showed the highest aspect ratio values among the cooked samples, as shown in Fig 4.8.

The circularity of the unheated samples remains practically constant at 0.60 for all concentrations of stearate, and remains constant for the two lower concentrations after heating. The circularity of the 3.0 % stearate solution decreases significant during the heating process to 0.48 ± 0.21. The average particle distance in the heated samples decreases significant with higher concentrations of stearate from 2.8 µm to 2.0 µm. The heating process is observed to increase the average distance between particles, with the average distances being approximately 2 µm for 1.0 % and 2.0 % stearate, which have no significant difference, and 1.6 µm for the 3 % unheated sample (compare Table 4.4 and Fig 4.8)

MDG

For the mean particle size, no statistically significant trend is noticeable in the overall MDG samples. The mean particle size of the 0.5 and 1.5% MDG samples increase during heating significant (0.5 %: $19.0 \pm 40.8\,\mu m^2$ to $25.8 \pm 121.2\,\mu m^2$, 1.5 %: $17.7 \pm 31.3\,\mu m^2$ to $31.6 \pm 149.7\,\mu m^2$), whereas it remains constant for the 1.0 % sample. During heating, the median decreases for all MDG concentrations. For the unheated samples, the median is in the range of $3.0\,\mu m^2$ to $6.7\,\mu m^2$ and for the heated samples it increases with the concentration from $1.5\,\mu m^2$ to $2.1\,\mu m^2$ (compare to Table 4.4).

Notably, the particle distribution for MDG showed less variation over concentration compared to the previous emulsifiers. The dominant size group over all concentrations is from $100\,\mu m^2$ to $500\,\mu m^2$ which covers between 35 % and 40 % of the total fat area. However, for the 0.5 % MDG sample the most area is covered with particles between $100\,\mu m^2$ to $2000\,\mu m^2$. In contrast, the 1.0 % sample fat area is mostly covered by particles from $10\,\mu m^2$ to $500\,\mu m^2$. In both samples, the largest particles extend to $4000\,\mu m^2$. The fat filled area of the highest MDG concentration is mostly covered with particles from $50\,\mu m^2$ to $1000\,\mu m^2$ and the biggest particles have an area of up to $6000\,\mu m^2$ (Fig. 4.7 D).

Detailed information for the change of particle sizes during heating is provided in Fig. A.4 in the supplementary information. Examining the aspect ratio (AR) during the heating process, this series showed the most marked variations between the three different emulsifiers. However, the AR values were generally lower compared to other emulsifiers. In their unheated state, the particles exhibited AR significant different values around 1.3 compared to the control, which then shifted significant from 1.41 ± 0.40 to 1.47 ± 0.42 for the heated samples (see Table 4.5). Similarly, the circularity analysis indicated that MDG gave the smoothest particles of all the emulsifiers. Circularity values ranged from 0.68 ± 0.20 to 0.78 ± 0.22 for the unheated samples, and although they experienced a slight reduction, they still maintained a circular morphology, of around 0.70 for the heated samples, and do not change significant for higher MDG concentrations. Similar to the stearate samples, the average distances increase significant during the heating process from roughly 2.0 µm to around 2.7 µm and are significant closer to each other compared to the control. Only the unheated sample with 1.5 % MDG has a significant lower average particle distance from 1.6 µm (see Table 4.4 and 4.5) compared to the other concentrations, whereas the distances of all concentrations decrease significant compared to the control.

4.3.4 Comparison of particle analysis between emulsifiers

All emulsifiers reduce the mean particle size of the unheated samples. The effect is more pronounced for collagen than for stearate and MDG. During heating, the mean particle sizes increase slightly for almost all emulsifiers and concentrations. Only the mean particle size of collagen 0.5 % and MDG 1.0 % is slightly lower, while that of stearate 3.0 % is about the same. For stearate, the heated mean area values decrease

with increasing concentration, whereas the values for MDG are comparable to the control mean area, as shown in Fig. 4.6 and Table 4.4. The influence on the area-weighted size distribution is the same for all emulsifiers, while they form a narrower distribution around smaller particle sizes and reduce the area covered by large particles above 10.000 µm^2 compared to the control. The distribution becomes narrower with collagen and stearate at all concentrations. In particular, MDG provides the narrowest distribution, around 100 µm^2 to 500 µm^2 for all samples, covering an area up to 40 % of the total fat area (see Fig. 4.7). Although there is no statistically significant trend in average particle size and spacing for the MDG samples. From the aspect ratio of MDG shows slightly rounder particles compared to the other emulsifiers, which is also seen in the circularity of the MDG samples and applies to both heated and unheated samples. For the average distance, the heated samples for collagen and stearate show a decrease with increasing concentration (see Table 4.4). However, no trend is shown for the MDG values. Heating increases the average distance of all samples, including the control. Compared to the control, the average interparticle distance decreases for each emulsifier sample (see Table 4.4 and Fig. 4.8).

4.4 Discussion

The most crucial inquiry is how these disparate outcomes can be synthesized and what insight can be derived from it. The basic matrix is composed of fat, liver and water, and the corresponding emulsion is based on the interface activity of the liver and sarcoplasm proteins [5, 56, 151, 155]. Furthermore, phospholipids released from cells during blending [157] interact with their polar heads and hydrophobic tails (fatty acids) in a manner consistent with the function of standard emulsifiers.

This basis provides already a semi-solid protein-fat emulsion. The fat is embedded in the hydrophobic matrix with irregular, but well separated droplets of different size as seen in Fig. 4.7, and in Fig. 4.5. Liver and sarcoplasmic proteins crosslink via disulphide bridges from cysteine to form elastic networks with sufficiently high elastic modulae G' as can be seen in Fig 4.1. The components, collagen, sodium stearate, mono- and diglycerides, now function in a systematic manner on this intricate matrix, as evidenced by CARS and mechanical experiments.

Collagen (respective gelatin) is a principal component of connective tissue, constructed from three protein strands that coil together in triple helices[158, 159]. During the process of heating, these strands separate and subsequently reform networks during the cooling phase [160]. Sodium stearate is an ionic emulsifier that carries a negative charge after dissociation of a positive sodium ion, see for example Fig. 2 in [147]. In contrast, mono- and diglycerides possess a polar head group only[134, 161]. These physical properties allow a better interpretation of the mechanical data from Fig. 4.3. For convenience, the LVR, the flow point, the maximum force and the initial slope are re-plotted in Fig. 4.4, which allows interpreting the difference in structure and properties better.

To support our discussion Fig. 4.9 provides a summary of the basic models for the diverse range of emulsifying agents, accompanied by a synopsis of the fat particle distribution as determined by the CARS experiments and an in-depth examination of the surface interaction between the fat particles and the different stabilizer and emulsifiers.

To be more specific, Fig. 4.9 A shows the bare control sample, where the fat particles are emulsified by liver proteins only. The elastic network is also formed by liver proteins. Fig. 4.9 B shows the competing liver protein network formed under heat and the collagen gel which is formed under cooling in the restricted phase space. This competition effect shows itself also in the non-monotonic behaviour of the initial shear modulus (see e.g. Fig. 4.2). In Fig. 4.9 C the additional effects of the electrostatic repulsion of the sodium stearate are depicted. Possible interactions between charged amino acids from the liver proteins and the charged head group of the emulsifiers are ignored. Fig. 4.9 D shows the polar MDG which has only less significant effects on the mechanical and textural properties

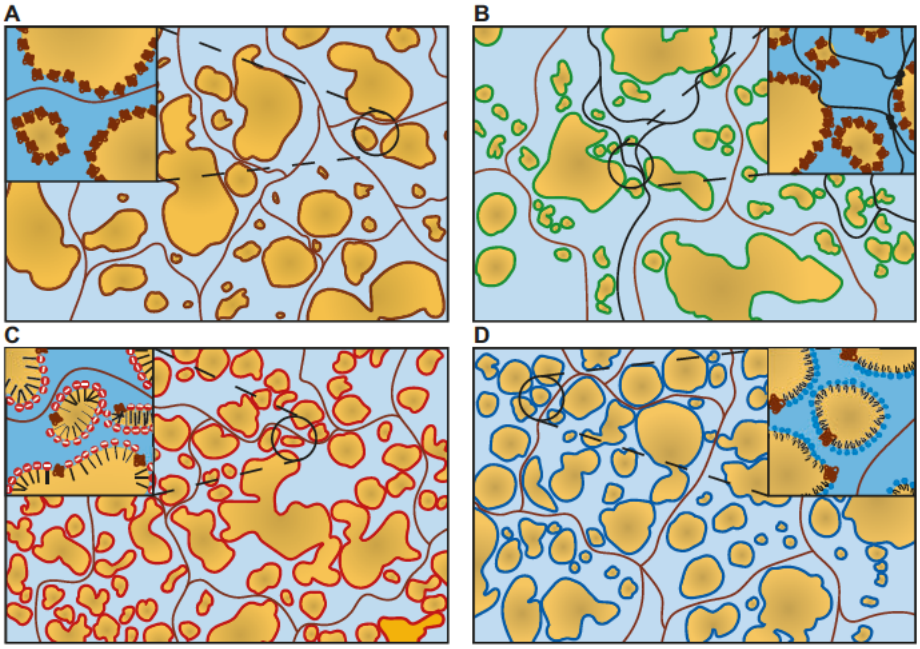

FIGURE 4.9: Simple models of the different systems discussed. A: Basic control system of emulsions without any emulsifier. The emulsion is only formed by the natural emulsifiers contained in the duck liver, such as proteins (drawn in brown) and phospholipids (not explicitly shown). The proteins emulsify the fat droplets and from a weak gel under heating. B: Added collagen (black lines) contributes additionally to the emulsification and forms a competing interpenetrating gel after cooling, which might compete with the weak surface activity of collagen. C: Charged sodium stearate placed at the interface between the fat and water phase and leads to an electrostatic repulsion of the fat particles which is noticeable in the force measurements. D: Mono- and Diglycerides as a polar emulsifier covers the surface of the fat droplets and only weakly affects the physical properties or the elastic properties of the gel.

4.4.1 Collagen / Gelatin

The primary structure of gelatin proteins indicates that these chains exhibit only relatively weak interface activities, and as a consequence, are only partially involved in the emulsion stability [162]. Following the soaking of collagen, heating in water and subsequent mixing into the liver-fat matrix, the connective tissue proteins are observed to dissolve primarily within the continuous hydrophilic matrix, with weak interfacial interactions at the surfaces of the fat particles.

Gelatin increases mainly the viscosity of the hot batter and forms a gel upon cooling. It is therefore reasonable to anticipate somewhat higher moduli. However, it is important to consider a number of factors. During heating, liver proteins cross-link comparably fast by forming disulphide bridges via cysteine [163], while collagen forms slowly triple helices during cooling [164]. Since the disulphide networks restrict space and phase space for the collagen network formation, local phase separations are likely, the networks become spatially heterogeneous, since they can no longer interpenetrate freely [145, 165, 166]. The collagen (micro)gels may act as soft plasticizer [145, 167], as can be associated with the increase of the LVR with increasing collagen concentration in Fig. 4.1 and 4.4 and Table 4.3.

On macroscopic scales, these effects are also visible in the behaviour of the texture compression results in Fig. 4.3 and 4.4, where the maximum force which is necessary to break the structure of the heated pâté increases with the collagen concentration. For heated pâtés, the modulus increases only between 0.0 % and 0.5 %, whereas it decreases again for the higher concentrations 1.0 % and 1.5 %. This effect shows the two competing network formations mentioned earlier.

The result shown in Fig. 4.1 and Fig. 4.3 indicate clearly the contribution of the collagen network to the elasticity on top of the cross-linked liver protein matrix. As the collagen was hydrated prior to addition, the collagen network resembles a gelatin gel when cooled and allowed to rest, forming triple helices as cross-links, which enhance the matrix modulus defined by disulphide bridges [155], electrostatic complexes, and hydrophobic interactions [39, 166]. However, the liver protein set their permanently cross-linked network under heating. It follows that the collagen gel is compelled to arrange itself in accordance with the protein network within the phase space. The formation of a coherent gel is contingent upon the concentration; instead, interpenetrating networks are formed. This phenomenon elucidates the elevated LVR, the augmented modulus, and the flow point, which is evident at diminished deformations in comparison to the other emulsifiers. This picture manifests itself with the measurements of the compression force.

Additionally, the distribution of the fat particles needs to be considered. Accordingly, the compression strain until the maximum force is reached correlates with the increasing concentration. The comparison of the texture parameters indicates that an increase in the collagen does not lead to stiffer and firm but in a more rubber like product. The fat particle sizes are for the collagen samples distributed over a wider size range. However, the bigger particles are not connecting to a fat cluster network,

as described in a previous publication in detail[155], to give the pate a stiffer texture. As already discussed, the overall physical behaviour is only partially contributed by the gel network and another part is contributed by the filler particles.

4.4.2 Sodium stearate

Sodium stearate is an ionic emulsifier, as mentioned earlier. The negatively charged hydrophilic carboxyl head tends towards the hydrophilic continuous phase, while the hydrophobic C 18 fatty acid chain assembles into the fat droplets [147]. The fat particles become smaller and more regular, compared to the control samples free of any added emulsifiers.

In addition, the dissociated sodium ions contribute to the Debye-Hückel screening of the Coulomb potential between the electrostatic interactions throughout the sample[168–170], including repulsion between the charged surfaces of the fat droplets, the charged amino acids in the matrix and interactions between the fat droplet matrix proteins.

Various scenarios are imaginable: By dissolving the emulsifiers in hot water for a long time, the sodium is completely dissociated from the hydroxyl stearate. During mixing, the emulsifiers coat the fat particles, which become charged. It is possible that the large negatively charged fat particles bind ionically to some of the charged amino acids, forming larger clusters which slightly increase the shear modulus, as suggested in Fig. 4.1. At the same time, the LVR does not change significantly (Fig. 4.4 A), so an additional network effect on deformation seems unlikely.

On the contrary, in compression tests the effect of the charges is more pronounced (see Fig. 4.4 C). The maximum force increases with increasing concentration of sodium stearate and increasing ionic strength. It is therefore likely that the surface of the fat particles become higher charged with increasing concentration. This implies higher resistance to compression when the fat particles are pushed together. Moreover, Table 4.4 indicates that the average distance between the fat particles decreases with increasing sodium stearate concentration, which increases the electrostatic repulsion further. Therefore, the maximum force increases significantly with concentration, as well as the maximum deformation, which indicates the breakdown of the structure, as seen in Fig. 4.4.

The distribution of the fat particles of the sodium stearate enriched specimens has a maximum around $100\,\mu m^2$ to $500\,\mu m^2$. Only a few particles have a greater size than $4000\,\mu m^2$ in total. The number of particles with a small area is lower than for samples with collagen. The stability of the emulsion during heating, respectively the change of the particle size, is for all sample quite high, as the changes in the mean and median particle sizes indicates in Fig. 4.6 and as well as the change in area coverage from different size groups indicates in Fig. A.3 in the supplementary information.

4.4.3 MDG

As previously described for sodium stearate, the polar MDG does not contribute to the mechanical properties. In comparison to the previous two series, G' for the raw samples, decreases with an increasing amount of emulsifier. The reduction in particle size of the raw samples results in a decrease in G'. The hardness of the samples remains unaffected for all concentrations, and the maximum force reached in the strain test is also independent of concentration. This behaviour can be drawn back to the molecular structure and the polar nature of head hydroxyl head groups of the MDG In comparison to the electrostatic interactions of the sodium stearate, the dipole interactions between OH-groups are very short ranged [171]. This indicates, that the interactions between MDG and the liver matrix is just too weak to change the mechanical behaviour in a similar way as ionic sodium stearate, where the charge repulsion and between the fat droplets contributes strongly to the force-strain behaviour as demonstrated in Fig. 4.3 and Fig. 4.4D.

The particle size distribution of the MDG-experiments shows to be the narrowest of the different additives. Additionally, up to 40 % of the particles have a size of 100 µm^2 to 500 µm^2. Also, the maximum particle size is the lowest of all series with up to 4000 µm^2 for 0.5 % and 1.0 % respectively 6000 µm^2 for the 1.5 % sample. During the heating process, the particles undergo a moderate change in the case of the lower two concentrations, with the highest MDG concentration exhibiting a higher coalescence rate (see Fig 4.6 and A.4). The particle size of the raw samples is even smaller, resulting in a decrease in the value of G' for higher concentrations. Therefore, MDG can influence properties that are important for production without significantly influencing the final properties. As expected, MDG proofs to improve the emulsion structure, but does not ameliorate the textural properties.

4.5 Conclusion

This investigation shows the specific influence of different physical properties of the emulsifiers and stabilizers in a clear way. These model system studies demonstrate further the importance of distinct differences in additive molecular structure. The systematic combination of different types of experiments, examining different length scales, reveals their influence on macroscopic properties and provides the first steps towards a systematic approach to their use in intricate food systems. As demonstrated here, the intrinsic physical properties of the additives change macro- and microscopic properties in a clear way. Consequently, the strategic employment of these agents can induce systematic alterations in the physical characteristics. This denotes an exercise in control, encompassing a better controlled manipulation of texture, mouthfeel, and, in essence, the release of flavour, which is invariably associated with the molecular composition [172].

Supplementary information

See supplementary information for area changes of fat particles during heating for the different additives.

Acknowledgments

The project was gratefully funded by VAN HEES GmbH, Walluf, Germany and we acknowledge the materials supply and many discussions with Dr. Alexander Stephan. The work was supported by the Villum Foundataion (Denmark), grant no. 00025414. We acknowledge the use of Danish Molecular Bio-Imaging Center, supported by the Novo Nordisk Foundation, grant no. NNF18SA0032928

Author Contributions

M.B.: sample preparation, texture analysis, rheology measurements, manuscript draft; M.A.V.: CARS imaging, image analysis, statistical analysis; M.P.C.: experimental design, interpretation, manuscript review; T.A.V.: project idea, interpretation, model development, supervision, writing, manuscript review

Funding

Open Access funding enabled and organized by Projekt DEAL.

Data Availability

The data that support the findings of this study are available from the corresponding author upon reasonable request.

Declarations

Conflict of interest The authors declare no Conflict of interest.

Chapter 5

Foie Gras Pâté without Force Feeding

Baechle, M.; Marques, A. M. L.; Via, M. A.; Clausen, M. P.; Vilgis, T. A.

This chapter is a version of the manuscript published in *Physics of Fluids* 37, 037196 (2025) https://doi.org/10.1063/5.0255813

Abstract

Foie gras (pâté) is regarded as an exceptional delicacy with a distinctive sensory profile. However, to obtain the fatty liver, animals, primarily ducks and geese, are force-fed a high-caloric cereals-based diet. With increasing awareness of the ethical conditions and animal welfare, products that mimic the unique textural characteristics of foie gras pâté are entering the market. The present work shows a way to produce a foie gras-like pâté based on the same raw materials as a convenient homemade liver pâté by enzymatic treatment of fat with *Candida rugosa type VII* lipase. The distribution of mono-, di- and triglycerides is altered, which affects the melting profile measured by dynamic scanning calorimetry (DSC). Nuclear magnetic resonance (NMR) spectroscopy and X-ray diffractometry (XRD) were used to compare the solid fat content and the crystalline part of the fat samples, showing an increase in both values compared to the untreated fat. The pâté samples were analyzed by rheological methods and force measurements to determine physical properties such as storage modulus and hardness. The emulsion structure was evaluated by coherent anti-Stokes Raman scattering (CARS) microscopy, and fat droplet size and shape were assessed. When the textural properties of the pâtés are compared, the treated fat pâtés behave more like real foie gras pâtés than their untreated counterparts

5.1 Introduction

Force-fed goose or duck livers, foie gras (fatty liver, literally from French) have high reputation in restaurants offering fine dining. Indeed their flavor, texture and mouthfeel is appreciated to be exceptional, and can be hardly imitated by other products, not matter foie gras is served fried, poached, or is for more convenient cases transformed to paté [21] by careful mixing, which preserves the fat distribution of the fatty liver. This process is followed by heating at maximum to 70 °C , which ensures pasteurization, but also permanently cross-links the protein matrix by forming disulfide bridges between cysteine[173].

Foie gras pâté is considered to be a semi-solid emulsion-type preparation with a spreadable consistency. It is characterized by a soft and melting mouthfeel, a prolonged release of flavor, and a persistent oral coating[23, 174]. From a culinary perspective, foie gras pâté is a food product with a smooth and rich texture, which is highly regarded as a delicacy in many countries.

In contrast, the production of foie gras is prohibited in numerous countries due to the fact that it is produced through the force-feeding of geese for several weeks prior to slaughter[24, 26, 29]. Therefore, it is imperative to identify alternative methods for producing analogous products based on liver and fat that do not involve products from force-feeding by gavage.

It is evident that an effort to emulate the properties of foie gras pâté entails a deliberate augmentation of the collagen content. To accomplish this objective, collagen-rich tissues, such as skin, undergo extensive cooking to produce a gel. The gel is subsequently integrated with liver and fat to form a pâté.[34]. The gelatin obtained from this process forms a network that, when dissolved in the oral cavity between 25 °C and 30 °C , leaves a melting impression. However, due to enhanced gel-like elasticity and the slow dissolution by unwinding of the gelatin tripelhelices[175], the resulting mouthfeel exhibits clear sensory differences when compared to foie gras pâté [65]. The composition of other products involves the incorporation of ingredients from disparate sources, including but not limited to butter, eggs, powdered milk, coconut fat, and agarose. The purpose of this amalgamation of ingredients is to achieve the desired textural characteristics [33]. Such preparations show in many cases unsatisfactory melting behavior during oral processing, which leads to enhanced friction[176].

From a technological standpoint, pâtés made with upgraded liver bases and additives will never match the quality and oral sensations of foie gras. Typical additives, such as collagen, gelatin, or emulsifiers with different physical properties, are incapable of enhancing the physical and textural characteristics of liver-fat-based emulsions to the extent of achieving the mouthfeel of foie gras pâtés, as demonstrated in specially designed experiments with similar matrices[177].

However, a neat way to avoid force-feeding and gavage is, to use the liver of slaughtered animals and their natural, subcutaneous rendered fat and transform them into a product, which resembles foie gras, without adding any proteins, emulsifiers or

fats from other sources[155]. The primary outcome of this study was the successful production of pure duck liver pâtés. However, significant deficiencies in the mechanical and thermal properties of the pâtés were also observed, which resulted in a diminished sensory experience during consumption. The underlying physical reasons are evident. Firstly, the melting behavior of rendered fat differs from that of foie gras fat. Secondly, the large-scale structure of the fat distribution cannot be replicated by simple emulsion processes when fat and protein concentrations are adjusted to the proportions found in foie gras.

Indeed, the secret behind its extraordinary properties is mainly defined by its high fat content and, more specifically, by the microscopic distribution of the fat and protein phases. However, it was shown already by Via et al. [155], that pure liver-fat-emulsions cannot satisfy simultaneously two basic requirements to resemble the microscopic structure of foie gras, namely emulsion stability and the distribution of fat. An essential contribution to texture and mouthfeel is determined by large, irregular fat clusters, which form percolating particle networks in the protein matrix. Such fat networks contribute to the elastic modulus, as is the case with many food materials[39, 124], including non-food systems as reinforced elastomers in materials science[122, 123, 125]. In the case of foie gras pâté, it is of particular importance to understand that the elastic nature of the fat network is based on the random (fractal) nature of the large clusters. These clusters demonstrate different responses to deformations as elastic matrices based on cross-linked proteins or polymer chains[178].

The occurrence of a large-scale fat cluster network and its spatial distribution in ducks and geese fatty livers is presumably a consequence of gavage and force-feeding[30]. The challenge for reconstructing "foie gras" from liver and rendered fat is thus, to find biophysical mechanism which leads to build up large, percolating fat clusters in a controlled way. A crude look into the fat of living ducks or geese offers a simple idea for reconstructing foie gras: treat the rendered fat to some extent with lipase. The outcome of this procedure is the generation of free fatty acids, mono- and diglycerols, and a concurrent reduction in triacylglycerols, without altering the overall composition of the duck or goose fat. Consequently, the polymorphism of the fat crystals can be expected to change, and the melting point can be expected to become shifted[35, 65, 179]. Indeed, the melting regime of rendered duck and goose fat with 24 °C to 34 °C appears slightly too low [180] compared to the fat from foie gras.

The fat metabolism in ducks and geese suggests, however, to treat the fat enzymatically by lipase. Specifically, lipase catalyzes the hydrolysis of triglycerides, resulting in the production of free fatty acids and mono- and diglycerides. The activity and reaction time of lipase influence the specific products of this process[74, 181]. Consequently, alterations in the melting and crystallization processes are anticipated. The central premise of this study is to utilize a lipase treatment that has been meticulously designed to modify the physical characteristics of the rendered fat, thereby aligning it with the properties of foie gras.

From these considerations strategies and hypothesis for developing foie gras from liver and rendered fat, both from non gavage animals :

1. Lipase treatment increases the solid fat content. The different polymorphism of the lipase treated fat provides higher melting regimes, relevant for the mouthfeel and oral processing.

2. Lipase treatment of the rendered fat enables the formation of large fat clusters, which percolate to form a particle network within the matrix as in pâtés from force-fed ducks or geese.

3. Lipase treatment does not change the overall fatty acid distribution of the duck fat, but alters the crystallization behavior significantly and thus the large-scale structure of the emulsion.

This hypothesis will be examined by various experiments and joining their results. A detailed analysis of alteration of the fat components will provide the basis for interpretation[35]. Their thermal behavior of the different fats will be studied by differential scanning calorimetry (DSC)[182].

The mechanical properties will be examined through the implementation of amplitude sweeps, a methodological approach that will facilitate the acquisition of pertinent information regarding the linear viscoelastic properties. This encompasses the storage and loss moduli, in addition to the linear viscoelastic range (LVR) at small amplitudes. At intermediate and large amplitudes, flow points and decrease of the moduli can be used as measures for breakdown of the structures[124, 155, 183, 184]. Compression tests examine the samples at alternative stress - deformation paths, and will provide complementary structural information in the context of the present research. [177, 185, 186].

A considerable proportion of the mouthfeel of foie gras during oral processing can be attributed to the thermal characteristics of the fat[32]. Any (duck) fat consists of liquid and solid parts, depending on the temperature. Temperature increase in the mouth decreases the solid fat content in the emulsions. It is therefore inevitable to control the solid fat content in the lipase treated samples. This is usually done by solid state nuclear magnetic resonance (NMR) techniques[187–189].

Apart from these, further insights can be gleaned from wide-angle X-ray scattering (WAXS) experiments, which facilitate a more nuanced perspective on the residual solids at a specific temperature[190], which support thermal DSC and NMR experiments.

The utilization of CARS (Coherent Anti-Stokes Raman Spectroscopy)-Microscopy has been demonstrated to facilitate the acquisition of a more profound comprehension of emulsion structures, while circumventing the utilization of mechanical destruction and staining of the samples by fluorescent dyes.[152, 153, 191, 192].

5.2 Materials and Methods

5.2.1 Materials

The following Materials are used for sample preparation: Lipase *Candida rugosa type VII* with an activity of 1071 U/mg (Sigma Aldrich, Merck KGaA, Darmstadt, Germany), NaOH (GPR RECTAPUR, VWR Chemicals, Darmstadt, Germnay), duck liver (Leon Dupont, Notre Dame de Riez, France), duck fat (Bruno Siebert, Ergersheim, France), NaCl (AnalaR NORMAPUR, VWR Chemicals, Darmstadt, Germany), Foie gras pâté sample (FGP): (Domaine de Langlardie, Piegut Dordogne, France),

5.2.2 Sample preparation

Lipase treatment

The lipase treatment was adapted from Sharma et al.[74]. 250 g of fat and reaction vessel with water (ratio 4:1 to the amount of fat) were preheated in a water bath (Julabo ME 4, JULABO GmbH, Seelbach, Germany) to 40 °C. Afterwards, the pH value of the water was adjusted to pH 7 with 1 M NaOH solution and the fat was added. The Lipase was added to the duck fat in a rate of 5 mg/g. The vessel was placed into a water bath heated to 40 °C and stirred with a lab stirrer (IKA T25 EC C 5000, IKA Werke GmbH & Co. KG, Staufen, Germany) at 350 rpm for 2 h respectively 4 h. To stop the reaction, 1 L of boiling water was added to the reaction mixture. The fat was separated from the water with a separation funnel. After cooling in a fridge at 5 °C, it was reheated to 80 °C for a complete water separation.

Pâté-preparation

The precise process for preparing pâté emulsions has been already outlined in a previous paper[155]. The following is a reiteration of the primary steps in the procedure, which were designed to enhance the clarity and comprehensibility of the subsequent description. The creation of the emulsions necessitated the incorporation of duck liver (490 g/kg), rendered duck fat respectively lipase-treated duck fat (392 g/kg), water (98 g/kg), and sodium chloride (20 g/kg). The liver was minced in two stages using a Hallde VCB-62 vertical cutter-blender (AB Hallde Maskiner, Kista, Sweden). The initial mincing stage operated at a speed of 1500 rpm for 5 s and was followed by a second stage at a speed of 3000 rpm for 10 s. Sodium chloride was then incorporated into the minced liver with brief stirring. Subsequently, fat and water were introduced, and the mixture underwent emulsification in two distinct steps. The first step involved a 15 s period of emulsification at 1500 rpm, followed by the second step, which involved a 30 s period of emulsification at 3000 rpm. To maintain a consistent temperature throughout the process, liquid nitrogen (50 mL to 100 mL) was added between each emulsification step. Following the degassing process, the batter was transferred into plastic containers and subsequently subjected to cooking in a preheated water bath (Julabo ME 4, JULABO GmbH, Seelbach, Germany) at a temperature of 80 °C for a

duration of 120 min. Thereafter, the cooked samples were allowed to cool and then stored at a temperature of 5 °C in a refrigerator.

Fat extraction

For fat extraction of the bought foie gras pâté samples, they were dried for at least 48 h in a Christ freeze dryer Alpha 1-2 LD plus (Martin Christ freeze dryers GmbH, Osterode am Harz, Germany) and then placed in a soxlet extractor. The extraction was performed with cyclohexane until it remained clear. The solvent was removed by a rotary evaporator.

5.2.3 Lipid analytics

Fatty acid distribution and content of mono-, di- and triglycerides

The fatty acid distribution was determined by gas chromatography with flame ionization detection (GC/FID) using the ISO 12966-2 Method[193] and the content of mono- di- and triglycerides was estimated by ISO 18395 Method[194] using high-performance size-exclusion chromatography (HPSEC). All measurements were performed by the external Company SGS Germany GmbH. Each sample was shipped in two 100 mL containers. The commercially bought Foie gras pâtés were sent in, whereas for others the pure fat was analyzed.

Differential scanning calorimetry - DSC

The temperature profile of the duck fat samples were acquired with a Mettler Toledo DSC3+/700/453 (Mettler Toledo, Columbus, Ohio). 20 µL of heated liquid fat were placed into a 100 µL aluminum crucible and an empty crucible was used as a reference. The sample was measured in 5 segments with a heating rate of 2 K/min using a nitrogen flow of 30 mL/min: 1. 25 °C to 75 °C 2. hold 3 min at 75 °C, 3. 75 °C to −100 °C 4. −100 °C to 75 °C 5. 75 °C to 25 °C From this melting or crystallization profile and the peak forms, the fusion enthalpy H_{fus} is calculated by the area of the melting peaks.

Solid fat content - NMR

For detecting the solid fat content (SFC) a Bruker Avance III console operating at 500.22 MHz 1H Larmor frequency at a Bruker superconducting 11.9 T wide bore magnet system using a commercial static 1H/X static solid-state NMR probe was used. Spherical sample shape was chosen by using 4 mm HR-MAS rotors as a sample holder. The 1H rf nutation frequency was adjusted to 62.5 kHz, corresponding to a 90° pulse length of 4 µs. The temperature was adjusted using a Bruker BSVT temperature controller. The fat was transferred to a 4 mm HR-MAS rotor sample holder. The samples were placed in the NMR and cooled to −20 °C and kept for 30 min and a spectrum was recorded. Then the temperature of the sample was increased by 5 °C and the process was repeated until a temperature of 50 °C was reached. To obtain

the SFC the spectra for each temperature were analyzed with the Bruker Top Spin Software. The full spectrum was integrated and set to 1 as a reference. Then the baseline was adjusted to the base of the sharp peak. The integration of the peak based on the full spectrum reference yield the liquid fat content (LFC). The SFC was calculated by $SFC(\%) = 1 - LFC * 100$ %. The supplementary information contains exemplary data illustrating the method by which the SFC was determined from the NMR spectra A.5.

Crystalline fat content (CFC) - XRD measurements

The measurements were performed with a Rigaku SmartLab X-ray diffractometer, therefore a thin layer of fat was spread on a glass slide and placed in the sample holder. The samples were measured at 5 °C and 37 °C with a Cu K-alpha x-ray beam with a wavelength of 1.5406 Å scanning from 1° to 35° with 0.3 °/min. The scattering slit was set to 0.5° and the receiving slit to 0.3°. To estimate the crystalline fat content from the diffraction measurements the area underneath the total diffractogram and the area of the amorphous phase was integrated. Thereafter, the crystalline fat content was calculated by this equation $CFC(\%) = (1 - A_{\text{amorphous}}/A_{\text{total}}) * 100$ %.

5.2.4 Physical Properties

Rheology

As already outlined by Via et al. [155] rheology experiments were conducted using a Gemini 200 rheometer (Bohlin Instruments, Malvern Panalytical Ltd., Malvern, UK), equipped with a parallel plate geometry of 25 mm diameter. To minimize sample slippage, 60-grit sandpaper was affixed to both plates. Circular samples, prepared using a 25 mm template and sliced to appropriate thickness, were positioned between the plates. The gap size was adjusted based on the sample thickness until a normal force increase of 2 N was observed, yielding gap dimensions between 1300 µm and 1950 µm. Measurements commenced after a 5 min equilibrating period, during which the storage modulus (G') and loss modulus (G'') were recorded. Oscillatory amplitude sweeps were performed with strains ranging from 0.01 % to 200 % at a frequency of 1 Hz and a temperature of 5 °C. Each sample underwent at least three measurements. Temperature sweeps were performed at 0.1 % strain and 1 Hz at a rate of 1 K/min starting at 5 °C until 40 °C was reached. The start and end temperatures were held for 5 min. The linear viscoelastic region (LVR) limit was identified as the strain at which G' deviated by 10 % from its initial value (G'_0), while the flow point was determined where G' equaled G''.

Texture Analysis

The hardness of the pâté samples was investigated using a ZwickRoell Universal Testing Machine AllroundLine Z005 (ZwickRoell GmbH, Ulm, Germany) as describedVia et al. [155]. Cylindrical samples with a diameter of 25 mm and a height of 20 mm were

prepared for the tests. Compression testing was conducted over two cycles[82] using a 75 mm diameter aluminum disc probe, operating at a speed of 1 mm/s, until the samples were compressed to 75 % of their original height. Measurements were performed at room temperature, with the samples maintained at 5 °C prior to testing. Each sample was tested at least six times. Hardness was defined as the maximum peak force recorded during compression, while elasticity was estimated by applying linear regression to the initial slope of the compression curve, using the first five data points exceeding a 0.01 % strain threshold.

5.2.5 Microscopic characterization

CARS Microscopy

As outlined by Via et al.[155] Coherent Anti-Stokes Raman Scattering (CARS) microscopy was conducted using the following setup: Leica SP8 CARS microscope (Leica Microsystems GmbH, Mannheim, Germany), picoEmerald multi-photon laser (APE, Berlin, Germany) light source, 650/210 BrightLine HC broadband filter (AHF analysentechnik AG, Tübingen, Germany) and a Leica 40× HC PL IRAPO objective (NA = 1.10). With the Stokes beam wavelength fixed at 1064.5 nm and the pump beam adjusted to 817 nm the symmetric -CH_2 stretching mode (2845 cm^{-1}) was excited to image the fat droplets. Detection was performed in epi-mode with a non-descanned photomultiplier tube (PMT) detector at room temperature. Laser power was optimized for each image to ensure signal intensity remained approximately 20 % below saturation. For imaging, pâté samples were sectioned and placed into 8-well chambers with #1.5 glass bottoms (Ibidi GmbH, Gräfelfing, Germany) shortly before acquisition. Images with dimensions of 1928 × 1928 pixels and a pixel size of 0.15 µm were captured at a depth of 5 µm within the sample. Each sample type was measured in triplicate.

Image analysis

Image processing was performed using *Fiji* software[119, 155]. Binary images were generated by applying the Huang algorithm for automatic thresholding[120]. Particles below the resolution limit were excluded as noise, and clusters with incomplete boundaries within the image frame were also disregarded. The analysis of fat particles included several parameters: particle area, aspect ratio and circularity. The *aspect ratio* (AR) represents the ratio of the longest to shortest axes of an ellipse fitted to the particle area, with AR=1 indicating a perfect circle and higher values reflecting increasing deviation from circularity. *Circularity*, which measures the relationship between particle area and perimeter, captures edge smoothness. Circularity values range from 0 to 1, with 1 corresponding to a perfect smooth circle and lower values indicating greater surface roughness.

5.2.6 Statistical Analysis

To evaluate the statistical significance of all data values, they were tested with DATAtab (DATAtab: Online Statistics Calculator. DATAtab e.U. Graz, Austria. URL https://datatab.de). Analysis of variance (ANOVA) was used for testing the series, whereas each sample was evaluated against other samples, using Bonferroni post-hoc tests based on ANOVA. With t-tests value pairs of a unheated vs. heated sample were tested for significance. All test were performed with a significance level of 5 % ($\alpha = 0.05$).

5.2.7 Abbreviations

In the following the abbreviations for the different samples will be used
Fats: LTF0 untreated rendered duck fat, FGF: fat extracted from force-fed foie gras pâté, LTF2: lipase treatment obtained from LTF0 after two hours, LTF4: lipase treated fat obtained from LTF0 after four hours.
Pâtés: FGP, foie gras pâté. LTP0 pâté composed of liver and untreated fat, LTF0, LTP2,4 pâtés composed of liver and LTF2 and FTF4, respectively.

5.3 Results

5.3.1 Comparison of the different fats

Lipase catalyses the cleavage of fatty acids from the glycerol backbone of triglycerides and is highly time-dependent[74]. Increasing the lipase treatment time to 4 hours results (LTF4) in an fat composition, which is almost broken down and consists mainly of free fatty acids. Triglycerides remained and diglycerides were also found for the 2 h shorter treatment (LTF2). The rate of cleavage depends on the number and length of the fatty acids bound to the glycerol[195]. In comparison, the untreated native duck fat, LTF0, consists mainly of triglycerides.

The fatty acid profile of the native and treated samples is nearly identical, as LTF0 serves as the substrate for the lipase treatment. This finding suggests that there has been no loss of fatty acids during the treatment process and that the samples contain a substantial amount of free fatty acids[64].

Fatty acid distribution and mono-, di- and triglyceride content

In order to understand the thermal, mechanical and structural behavior, it is important to consider the fat and lipid composition. The fatty acid distributions of the native duck fat and lipase treated fat (LTF) samples differ only slightly, as shown in Fig. 5.1. Therefore, the profile of the FGF sample is different for some specific fatty acids. Palmitoleic acid is about half as abundant in the foie gras fat (FGF) sample (1.89 ± 0.02 %). Conversely, the content of stearic acid in the foie gras fat, FGF, samples is twice as high (16.25 ± 1.57 %). The content of oleic acid (50.89 ± 3.22 %) is about 8 % higher than in the other samples. The content of linolenic acid in the FG

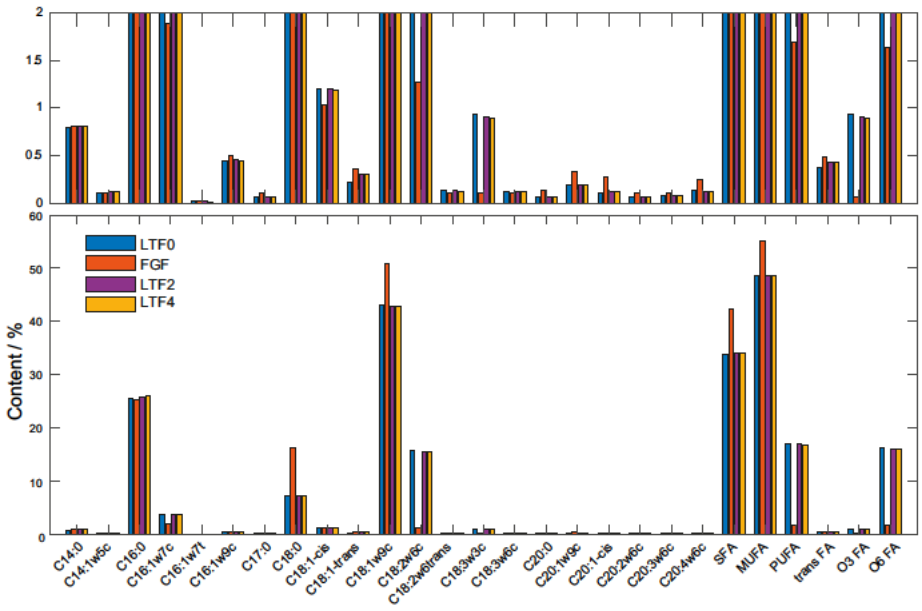

FIGURE 5.1: Fatty acid composition of the different fat samples. The native duck fat (LTF0) is shown as blue bars, the red bars show the results of the foie gras fat (FGF) fat and 2 h lipase treated (LTF2) fat is shown in purple and 4 h lipase treated (LTF4) fat in yellow. The upper panel is a zoom in for better comparison.

samples is 10 times lower than in the native and LT fat samples with about 15 % to 1.3 %.

Overall, the content of saturated fatty acids is higher in the FGF sample (42.43 ± 3.23 % compared to about 34.00 %), as is the content of monosaturated fatty acids (55.0 to 48.5 %). In contrast, the content of polyunsaturated fatty acids is an order of magnitude higher in the native and LT-treated samples (about 17.0 % compared to 1.7 %). The detailed values are given in table 5.1.

The content of mono-, di-triglycerides differs for all samples as shown in Figure 5.2. The monoglyceride content is close to zero for all samples, except for sample LTF2, which reaches a monoglyceride content of 1.05 ± 0.05 %. The same behavior is observed for the diglycerides, where all the samples, with the exception of sample LTF2 with 7.10 ± 1.30 %, have a content of around 1 % diglycerides. The greatest differences are found in the triglycerides and free fatty acids. The untreated fat sample (LTF0) has a triglyceride content of 97.90 % and a free fatty acid content of 0.6 %. The FGF sample has a triglyceride and free fatty acid content of 90.05 ± 4.55 % and 8.80 ± 4.70 % respectively. For the lipase treated samples the triglyceride content is quite low with 13.85 ± 3.45 % and 2.15 ± 0.05 % and they have the highest free fatty acid content with 78.00 ± 4.80 % (LTF2) and 96.60 ± 0.10 % (LTF4) as shown in table 5.2.

TABLE 5.1: Fatty acid distribution of the untreated duck fat (LTF0), extracted foie gras fat (FGF) fat and lipase treated fat 2 h (LTF2) and 4 h (LTF4).

	Samples			
Fatty acid/%	**LTF0**	**LTF2**	**LTF4**	**FGF**[1]
Myristic acid (C14:0)	0.79 ± 0.00	0.81 ± 0.01	0.81 ± 0.01	0.81 ± 0.04
Myristoleinic acid (C14:1w5c)	0.11 ± 0.00	0.12 ± 0.00	0.12 ± 0.00	< 0.10 ± 0.01
Palmitic acid (C16:0)	25.56 ± 0.00	25.81 ± 0.01	25.92 ± 0.00	25.23 ± 1.72
Palmitoleic acid (C16:1w7c)	3.56 ± 0.00	3.59 ± 0.00	3.58 ± 0.00	1.89 ± 0.02
Palmitelaidic acid (C16:1w7t)	0.02 ± 0.00	0.02 ± 0.00	0.02 ± 0.01	< 0.02 ± 0.0
cis-7-Hexadocenoic acid (C16:1w9c)	0.45 ± 0.00	0.46 ± 0.01	0.45 ± 0.00	0.50 ± 0.10
Heptadecenoic acid (C17:0)	0.07 ± 0.00	0.07 ± 0.01	0.06 ± 0.00	< 0.01 ± 0.01
Stearic acid (C18:0)	7.21 ± 0.00	7.19 ± 0.01	7.21 ± 0.00	16.25 ± 1.57
Octadecenoic acid, cis-isomers excl. (C18:1-cis)	1.21 ± 0.00	1.20 ± 0.00	1.19 ± 0.00	1.04 ± 0.11
Octadecenoic acid, trans-isomers (C18:1-trans)	0.22 ± 0.00	0.30 ± 0.01	0.30 ± 0.00	0.36 ± 0.00
Oleic acid (C18:1w9c)	42.99 ± 0.00	42.89 ± 0.06	42.83 ± 0.04	50.89 ± 3.22
Linoleic acid (C18:2w6c)	15.77 ± 0.00	15.58 ± 0.06	15.54 ± 0.02	1.28 ± 0.06
Octadecadienoic acid, trans-isomers (C18:2w6trans)	0.13 ± 0.00	0.13 ± 0.00	0.12 ± 0.00	0.11 ± 0.03
alpha Linolenic acid (C18:3w3c)	0.93 ± 0.00	0.91 ± 0.01	0.90 ± 0.00	< 0.10 ± 0.01
gamma Linolenic acid (C18:3w6c)	0.12 ± 0.00	0.12 ± 0.00	0.12 ± 0.00	0.10 ± 0.01
Arachidic acid (C20:0)	0.06 ± 0.00	0.06 ± 0.00	0.06 ± 0.00	0.14 ± 0.01
cis-11-Eicosenoic acid (C20:1w9c)	0.19 ± 0.00	0.19 ± 0.00	0.19 ± 0.00	0.33 ± 0.04
Eicosenoic acid, cis-isomers excl. (C20:1-cis)	0.11 ± 0.00	0.12 ± 0.00	0.12 ± 0.00	0.28 ± 0.01
cis-11,14-Eicosadienoic acid (C20:2w6c)	0.07 ± 0.00	0.06 ± 0.00	0.06 ± 0.00	< 0.10 ± 0.01
cis-8,11,14-Eicosatrienoic acid (C20:3w6c)	0.08 ± 0.00	0.08 ± 0.00	0.08 ± 0.00	0.11 ± 0.01
Arachidonic acid (C20:4w6c)	0.13 ± 0.00	0.12 ± 0.00	0.12 ± 0.00	0.25 ± 0.02
Saturated fatty acids	33.69 ± 0.00	33.93 ± 0.00	34.06 ± 0.00	42.43 ± 3.23
Monounsaturated fatty acids	48.62 ± 0.00	48.56 ± 0.07	48.48 ± 0.04	54.99 + 3.32
Polyunsaturated fatty acids	17.10 ± 0.00	16.87 ± 0.06	16.82 ± 0.01	1.69 ± 0.07
trans fatty acids	0.37 ± 0.00	0.44 ± 0.01	0.44 ± 0.01	0.48 ± 0.04
Omega-3 fatty acids	0.93 ± 0.00	0.91 ± 0.01	0.90 ± 0.00	0.06 ± 0.01
Omega-6 fatty acids	16.17 ± 0.00	15.96 ± 0.06	15.92 ± 0.01	1.64 ± 0.07

[1]extrapolated to 100 %. The Results of the analysis were based on the total amount of pâté sample.

TABLE 5.2: Content of mono-, di- and triglycerides of treated (LTF2,LTF4) and untreated Fat (LTF0) samples and extracted foie gras fat (FGF)

	Samples			
	LTF0	**LTF2**	**LTF4**	**FGF**
Monoglycerids/%	0.10 ± 0.00	1.05 ± 0.05	0.20 ± 0.00	0.10 ± 0.00
Diglycerides/%	1.40 ± 0.00	7.10 ± 1.30	1.05 ± 0.05	1.05 ± 0.15
Triglycerides/%	97.90 ± 0.00	13.85 ± 3.45	2.15 ± 0.05	90.05 ± 4.55
Free fatty acids/%[1]	0.60 ± 0.00	78.00 ± 4.80	96.60 ± 0.10	8.80 ± 4.70

[1]Calculated by subtraction of MDG content from total 100 %.

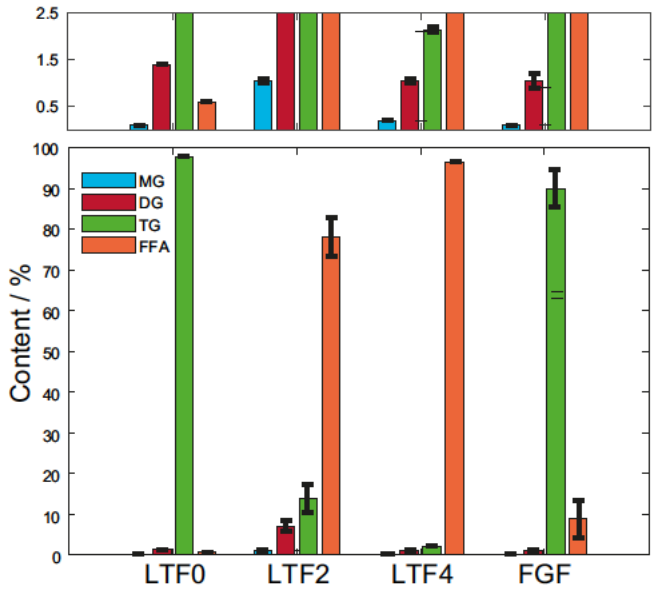

FIGURE 5.2: Distribution of monoglycerides (MG: light blue bars), diglycerides (DG: dark red bars) and triglycerides (TG: green bars) and free fatty acids (FFA: orange bars) of the different fat samples used in the emulsions. Above the main graph is a zoom to show the detailed distribution of the mono- and diglycerides.

DSC measurements

The DSC experiments (see Fig. 5.3) indicate a notable distinction in the melting and crystallization behavior between the native (rendered) duck fat (LTF0) and the foie gras fat (FGF). In the context of this investigation, melting is imperative for the oral process in the mouth; consequently, the melting process is the primary focus of the subsequent discussion. However, interested readers can find the complete analysis of the DSC results in the Supplementary Information.

Initially, it is evident that both FGF and the rendered fat LTP0 exhibit no significant melting peaks within the temperature range from $-60\,^{\circ}\mathrm{C}$ to $-20\,^{\circ}\mathrm{C}$. In contrast, both lipase-treated fats, LPF2,4, demonstrate clear melting peaks no. 1, 2, and no. 3,4. These two lower melting peaks appear around $-37\,^{\circ}\mathrm{C}$ and around $-19\,^{\circ}\mathrm{C}$ (see Fig. 5.3 B). For the melting in the mouth these melting processes are of little importance, but they indicate the cleavage process. The peaks for both LTP2 and LTP4, can be addressed to the melting points of short chain fatty acids or poly unsaturated fatty acids. The melting ranges of the unsaturated linolenic acid (C18:3) and arachidonic acid (C20:4) are determined $-21.0\,^{\circ}\mathrm{C}$ to $-10.4\,^{\circ}\mathrm{C}$ and $-43.4\,^{\circ}\mathrm{C}$ to $-38.4\,^{\circ}\mathrm{C}$ [196]. These fatty acids are part of the native duck fat and listed in Fig. 5.3. Table 5.1 shows, that these fatty acids have been cleaved by the lipase from rendered duck fat, since the corresponding much broader crystallization peak shows at about $10\,^{\circ}\mathrm{C}$ higher temperatures. However, these fractions do not play a significant role in the mouthfeel but serve merely as a useful check, as the rendered fat shows a tiny peak at a similar temperature as peaks no. 3 and 4.

FGF shows a very broad and pronounced peak no. 5, foie gras fat first underwent

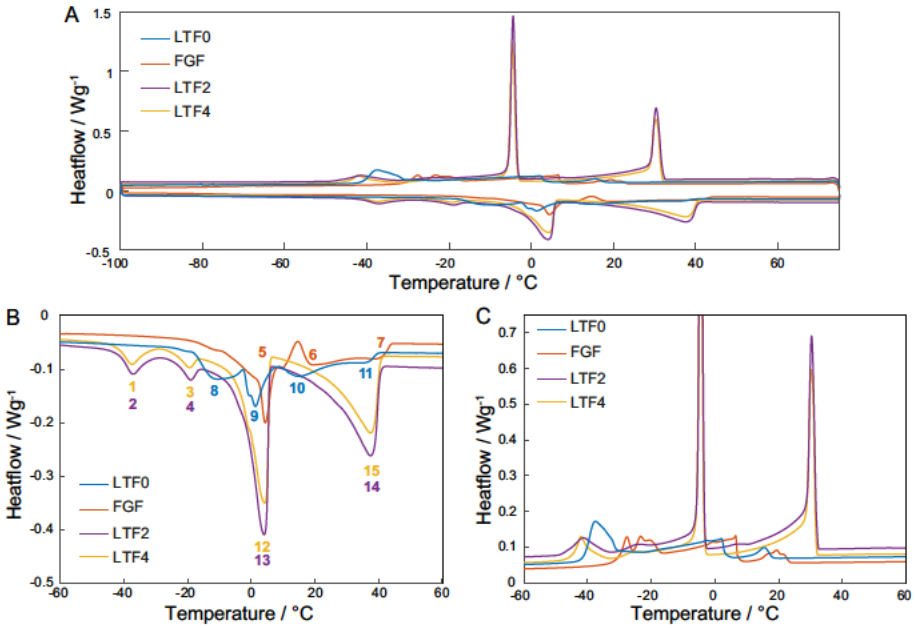

FIGURE 5.3: Panel A displays the mean DSC curve for each fat sample for an overview. Panel B provides a magnified view of the melting process of the DSC measurements. Panel C illustrates the crystallization profile during the heating of the fat samples. The untreated duck fat (LTF0) is shown in blue, the fat extracted from the foie gras pâté is marked in red (FGF). The two different lipase treated fat samples are plotted in purple (2 h: LTF2) and yellow (4 h: LTF4).

a broad and pronounced melting regime, commencing at −20.5 °C and concluding at 14.6 °C, with a sharper peak at 4.4 °C and a small shoulder at about 7 °C. Immediately it is followed by a second melting regime between 14.7 °C and 44.2 °C, with two peaks at 19.4 °C (peak no. 6) and 38.5 °C (peak no. 7), which can be considered as most important for the typical foie gras mouthfeel, because this melting regime is definitely felt in the mouth by texture (and friction) changes.

In contrast, native, rendered duck fat exhibits melting already at temperatures between −23.2 °C and −2.6 °C with a peak at −10.8 °C, peak no. 8 in Fig. 5.3 B, a distinct melting between −2.3 °C and 7.5 °C (peak no. 9 at 1.3 °C), followed by another broad melting regime between 8.9 °C and 40.2 °C with peaks at 14.9 °C and 35.9 °C (peak nos. 10 and 11). These peaks appear at lower temperatures as those of the FGF. Obviously both fats exhibit a different mouthfeel during melting in the oral cavity with about 37 °C. Thus, the comparison of the melting profile shows, that pure rendered duck fat will not be able to imitate the melting behavior of foie gras fat, especially in the temperature range between 0 °C and 37 °C, relevant for oral processing, where their melting profiles are different. Rendered (native) duck fat melts at lower temperatures, and thus the long-lasting melting effect known from foie gras is missing.

However, lipase treatment shows for both exposure times, 2 h and 4 h, an equalization of the melting curves compared to rendered duck and foie gras fat. The multiple melting peaks and regimes between −23.2 °C and 8.9 °C are blurred and joined on

a more pronounced broader peak (LTF2: no. 12, LTF4: no. 13) ranging between −16.1 °C to about 6.7 °C.

The pronounced melting peaks 12 and 13 in Fig.5.3 A and B within the range −5 °C and 15 °C after lipase treatments are most likely generated from oleic acid, C18:1 dominated crystals, which takes a large fraction in the duck fat, as can be seen in Table 5.1. The corresponding crystallization peaks and can be located at about −5 °C and −10 °C. Thus suggests again, that a sufficient number of the C18:1 fatty acids are cleaved from the triglycerides in the rendered fat to form reversible melting in crystallization.

In foie gras fat samples these low-temperature peaks do appear in the melting, despite their presence, because these fatty acids are mostly bound in triglycerides and cannot form larger crystals among themselves. However, signatures of triglycerides containing polyunsaturated fatty acids can be detected in the crystallization profile Fig.5.3 C in the temperature range −30 °C to −18 °C.

It is evident that the melting peaks are considerably broader in width and thus encompass a more extensive temperature range than the crystallization peaks. Most important for the texture and the mouthfeel are the pronounced melting regimes between −8.9 °C to 6.6 °C and the broad regime between 6.7 °C and 42.4 °C, which are induced by the lipase treatment. These melting peaks (LTF2: peak nos 12 and 14, LTF4: peak nos. 13 and 15) show a broad distribution starting with a shoulder to lower temperatures, leading to a peak temperature of 4.1 °C and 37.6 °C.

A comparison between the foie gras fat (FGF) shows immediately, that this lipase treatment induced melting region is similar with the melting regime of the foie gras. In other words, the broad melting regime of the LTF0 (native duck fat) between peaks nos. 10 and 11 becomes shifted to higher temperature ranges, and thus close to those of FGF. This is quite intriguing, since the lipase action under given time and activity increases the number of free fatty acids in such a way the higher effect of the higher amount of C18:0 lipids in foie gras becomes compensated.

Table 5.1 shows the molecular origin of the differences in the melting properties. Foie gras fat contains more saturated fatty acids than rendered duck fat, especially stearic acid, C18:0, which is about the double in concentration. Furthermore, oleic acid, C18:1, is found to be significantly more prevalent at 51 % than in rendered fat at 43 %. On the other hand, more linoleic acid, C18:2, appears in rendered fat than in foie gras fat. Only the concentration of palmitic acid, C16:0, is about the same in both fats.

The peaks of the lipase treated samples indicate a higher heat flux than the native and FGF samples. Integration of the peaks shows that the enthalpy of melting is, with around −146 J/g, two times higher in total in the lipase treated samples (see table 5.3) compared to the native duck fat and foie gras fat. The three peaks of the native duck fat contribute with −22.0 J/g (peak no. 8), −21.7 J/g (peak no. 9) and −28.2 J/g for the regime of peak nos. 10 and 11 to a total heat of fusion of −71.9 J/g. For the foie gras fat the two broad regimes have a total melting enthalpy of −40.7 J/g (peak no. 5)

TABLE 5.3: Enthalpy of melting ΔH_m and peak temperatures of the melting profile for untreated duck fat (LTF0), extracted foie gras fat (FGF) fat and 2 h and 4 h lipase treated fat (LTF2,4) samples. In Fig. 5.3 the corresponding melting peaks are numbered in part B

Sample		**Peak no.**				**Total ΔH_m**
		8	9	10	11	
LTF0	T/°C	-10.8 ± 0.1	1.3 ± 0.1	14.9 ± 0.6	35.9 ± 0.4	
	ΔH_m/J/g	-22.0 ± 0.7	-21.7 ± 0.6	-28.2 ± 0.7		-71.9 ± 1.9
		2	4	13	14	
LTF2	T/°C	-40.2 ± 2.31	-19.4 ± 0.9	4.0 ± 0.1	37.5 ± 0.1	
	ΔH_m/J/g	-9.7 ± 0.1	-8.5 ± 1.5	-66.5 ± 1.5	-61.9 ± 1.2	-146.6 ± 4.3
		1	3	12	15	
LTF4	T/°C	-37.5 ± 0.1	-19.4 ± 0.5	4.2 ± 0.1	37.4 ± 0.1	
	ΔH_m/J/g	-9.1 ± 0.2	-8.2 ± 0.7	-67.5 ± 0.5	-61.04 ± 0.3	-145.9 ± 1.7
		5	6	7		
FGF	T/°C	4.4 ± 0.1	19.4 ± 0.1	38.5		
	ΔH_m/J/g	-40.7 ± 4.1	-24.5 ± 2.3			-65.1 ± 6.5

and −24.7 J/g (sum of peak no. 10 and 11). Both lipase treated samples differ only marginal in the release of heat during melting. Whereas the more pronounced peaks in both samples (nos. 12,13 and 14,15 in panel B of fig. 5.3) release around −67 J/g and −61 J/g heat, leading to a total heat of fusion of around −146 J/g (see Table 5.3).

These differences are also manifested by the crystallization behavior. The crystallization of different fractions of the foie gras fat (FGF) start about 3.8 °C to 13.8 °C earlier as those of the rendered duck fat. Three different crystallization peaks are visible for both samples and the first starting at 23.9 °C and transition into the next peak at 9.0 °C for the foie gras fat respectively 4.8 °C for the native duck fat. The peak temperature is at 6.6 °C for the foie gras fat and 2.1 for the native duck fat, and both show a shoulder to lower temperatures. For the foie gras fat, the last peak ranges from −16.4 °C to −36.8 °C and for the native duck fat from −29.7 °C to −44.7 °C. On the reverse, the corresponding crystallization process starts at 32 °C for both lipase treated samples, with sharp peaks at 30.4 °C. They both have a shoulder to lower temperatures ending at −2.3 °C and with a transition into the next peaks at −2.4 °C. The peak maximum of the peaks at −4.5 °C and also has a broader shoulder to lower temperatures, which transition into two peaks at −24.9 °C and −41.5 °C, as shown in Fig. 5.3 Panel C and Table A.1).

As for the melting, the energy released by crystallization is with around 140 J/g for the lipase treated samples as twice as high as for the native duck fat and foie gras fat samples with 70.0 J/g respectively 74.1 J/g (see Table A.1). A further detailed description of the melting and crystallization behavior is shown in the supplementary information.

Consequently, the differently shaped peaks resulting from lipase treatment (nos. 12, 13) require a significantly higher latent heat for melting in this temperature regime as FGF in the relevant mouthfeel temperature range between 5 °C to 37 °C. Physically higher enthalpies point to more crystals with less defects[197, 198] after

lipase treatment, which is explained by the increase of concentrations fatty acids, which form stably crystals, as will be confirmed by the WAXS and CARS experiments below.

Solid and crystalline fat content

The solid fat content (SFC) as a function of temperature is shown in figure 5.4 A. As expected, at low temperatures, −20 °C , the solid fat content is the highest for each sample, ranging from 68.1 ± 3.0 % (LTF0) to 89.5 ± 1.0 % for the LTF4 sample. With increasing temperature, the solid fat content decreases due to selective and partial melting, as already seen by the distinct broader melting regimes in Fig. 5.3. At 5 °C , where all mechanical experiments are carried out, the SFC is located between 26.4 ± 4.2 % (LTF2) and 57.9 ± 3.1 % (FGF). The native fat has a slightly higher SFC of around 29.0 ± 4.1 % than the LTF2 sample, as shown fig. 5.4. The LTF4 sample is in between with 41.6 ± 2.4 %.

The curve progression of the various samples with increasing temperature is of particular interest here. The SFC of native, rendered duck fat (LTF0) starts at 20 °C from the lowest value and decreases smoothly and gradually and is almost molten and liquid at the mouth temperature T=37 °C. FGF shows a smooth and gradual decrease as well but shows a higher SFC as native duck fat for all temperatures. At about 40 °C both approach each other. The important point for the present considerations is, that FGF exhibits at 37 °C still a SFC of about 4.4 %.

A visual analysis of the curves reveals significant differences in their shape, with lipase-treated fat samples exhibiting a distinctive pattern. Firstly, the 4 h lipase treatment shows throughout higher values compared to the 2 h treatment. In the temperature range between −20 °C and 10 °C , both LTF2 and LTF4 exhibit a steeper and more monotonous decline in comparison to the native fat and FG. However, both LTF2 and LTF4 display a kink, indicating a slower decrease towards lower SFC values. The melting profiles of both LTF2 and LTF4 indicate an initial melting at lower temperatures, as evidenced by the peaks labeled no. 12 and no. 13 in Fig. 5.3, and a slower melting starting between 20 °C and 40 °C, as seen in the DSC at the broad peaks no. 14 and no. 15, for both treatments.

In addition, both lipase treatments show a finite value for the SFC at 37 °C as FGF. The SFC for the 2 h treatment is with 1.8 % slightly below the LTF0 with 2.2 % and the FGF with 4.4 %, whereas the 4 h treatment is with 5.8 % slightly higher (see Table 5.4). Nevertheless, the values for LTF2,4 compare very well to each other and proof that an appropriate lipase treatment change the melting properties of rendered fats in the targeted direction. For a consistent picture, an overview of the analyzed NMR-spectra for each sample are shown in the supplementary information. Fig A.6 to A.9 provide the measurements at T=−20 °C, T=5 °C and T=35 °C of each sample.

The crystalline fat content (CFC) is estimated from wide angle XRD measurements (WAXS) at 5 °C as shown in Fig 5.5. The native fat sample (LTF0) has the lowest crystalline fat content with 11.0 ± 0.6 %, followed by the foie gras fat sample with 18.3 ± 3.3 %. For the lipase treated samples a crystalline fat content of 32.6 ± 5.1 %

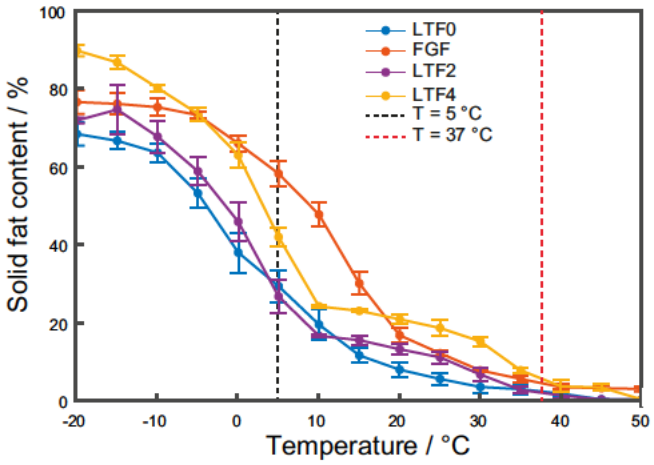

FIGURE 5.4: The temperature dependent solid fat content. The vertical dashed line black indicates T=5 °C , the dashed red line the mouth temperature T=37 °C . The native duck fat (LTF0) is marked blue, the foie gras fat (FGF) red and purple and yellow for 2 h and 4 h lipase treated fat (LTF2, LTF4).

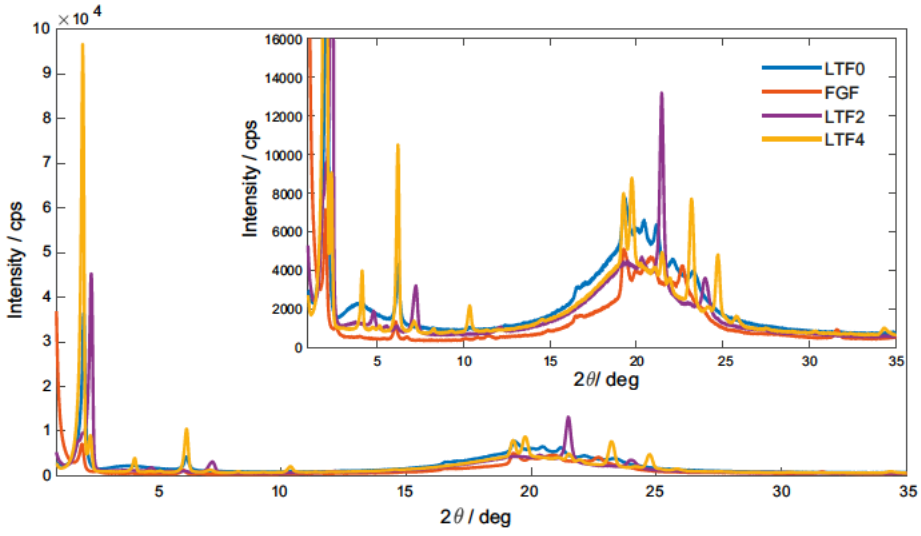

FIGURE 5.5: Wide-angle X-ray profiles measurement of the different samples at 5 °C . The insert shows a zoom of the y-axis to enhance the visibility of the main peak regions. The native duck fat is shown as a blue line, the foie gras fat (FGF) is shown in red. The lipase treated samples are shown as a purple (2 h : LTF2) and yellow (4 h : LTF4) line.

(LTF2) and 39.1 ± 3.3 % (LTF4) was measured (see Fig 5.6 and Table 5.4). In Fig. 5.6 the fat samples are measured with wide-angle x-rays at 37 °C and for native fat barely any crystalline fat content is present. Whereas, for the 2 h lipase treated fat still some peaks are visible in the XRD-measurements. The measurements of foie gras fat, FGF, as well as LTF4 exhibit a pronounced number of X-ray reflexes, more as LTF2. By estimating the peak area of the XRD graphs the crystalline part of the solid fat fraction was determined. This can be seen in Table 5.4, by the systematic differences in the values for the SFC and CFC at 5 °C for the different samples. These discrepancies can be attributed to the fundamental disparities in the measurement techniques employed. Nuclear magnetic resonance (NMR) probes are capable of discerning local (atomistic) scales, while wide-angle X-ray scattering probes are more apt at detecting scales at the lattice distances. However, nuclear magnetic resonance detects immobile, solid parts in amorphous and crystalline parts, whereas wide-angle X-ray scattering only identifies hard crystalline solid parts. Therefore the values for SFC measured by NMR are higher than those for CFC provided by the WAXS experiments. Consequently, the NMR also includes the amorphous and immobile defect rich fraction of the solid fat phase. Similar trends of much larger SFC values compared to CFC have also been found by Arita-Merino et al. [199].

Table 5.4: Solid fat content (SFC) and crystalline fat content (CFC) in % of different fat samples. Statistical significance tested with ANOVA-test.

T/°C	**SFC/%**			
	LTF0	**LTF2**	**LTf4**	**FGF**
-20	68.1 ± 3.0	71.6 ± 0.7	89.5 ± 1.5	76.3 ± 3.3
-15	66.4 ± 2.3	74.4 ± 6.2	86.5 ± 1.8	75.8 ± 2.7
-10	63.3 ± 2.4	67.4 ± 4.1	79.9 ± 0.9	75.0 ± 2.2
-5	52.9 ± 3.7	58.5 ± 3.6	73.3 ± 1.7	72.9 ± 0.8
0	37.7 ± 5.2	45.6 ± 5.0	62.6 ± 3.2	65.7 ± 2.1
5	29.0 ± 4.1	26.4 ± 4.2	41.7 ± 2.4	57.9 ± 3.1
10	19.2 ± 3.9	16.3 ± 0.5	23.9 ± 0.3	47.4 ± 3.2
15	11.3 ± 2.0	15.2 ± 1.2	22.7 ± 0.3	29.8 ± 2.8
20	7.6 ± 1.9	12.9 ± 1.3	20.6 ± 1.2	16.5 ± 1.9
25	5.3 ± 1.5	10.8 ± 1.6	18.3 ± 2.1	11.9 ± 0.6
30	3.2 ± 1.4	6.4 ± 1.6	14.9 ± 1.2	7.4 ± 0.4
35	2.6 ± 1.4	2.4 ± 0.7	7.5 ± 0.6	5.3 ± 0.8
40	1.5 ± 0.7	1.0 ± 0.8	3.3 ± 1.5	3.2 ± 0.7
45	0.0 ± 0.0	0.0 ± 0.0	3.1 ± 0.9	2.9 ± 0.6
50	0.0 ± 0.0	0.0 ± 0.0	0.0 ± 0.0	2.7 ± 0.6
37[1]	2,2	1,9	5,8	4,4
	CFC / %			
5	11.0 ± 0.6	32.6 ± 5.1	39.1 ± 3.3	18.3 ± 3.3
37	2.7 ± 0.6	5.6 ± 1.9	12.9 ± 2.0	23.0 ± 4.3

[1] extrapolated values.

This result indicates that the crystal fraction increases with lipase exposure time

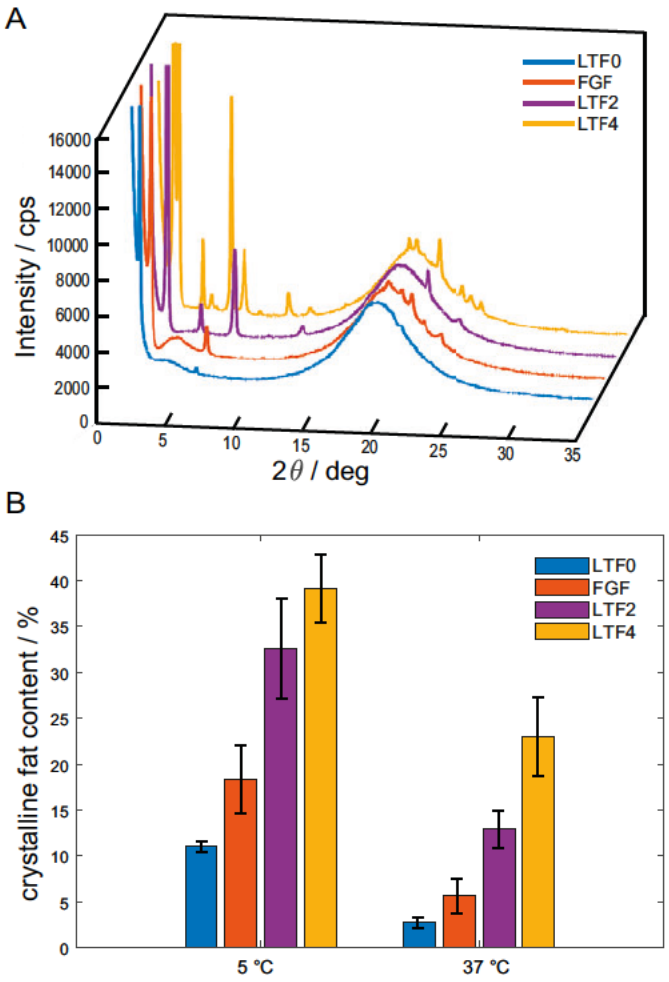

FIGURE 5.6: A shows the WAXS profiles at 37 °C of each fat sample are plotted. B shows the CFC of each sample for 5 °C and 37 °CC in a bar plot. The untreated duck fat (LTF0) is marked blue, the foie gras fat (FGF) red and purple for 2 h lipase treated fat (LTF2) and yellow for 4 h treatment time (LTF4).

between 2 h and 4 h , which is due to still increasing concentrations of free fatty acids by ongoing cleavage, especially from the dominant fraction of C16:0, C18:0 and C18:1 fatty acids. As shown in Fig.5.6, the crystal fraction increases still between 2 h and 4 h lipase treatment, up to the double value compared to rendered duck fat. Consequently larger and more stable crystals may appear. This assumption will be confirmed by the results of the CARS experiments below.

Another point that corroborates this claim is evidenced by WAXS experiments conducted on samples at 37 °C, which is equivalent to the temperature of the oral cavity. These results are shown in Fig.5.6. As shown in Fig. 5.6 B Parts of the fat melts between 5 °C and 37 °C. As suggested by the DSC experiments in Fig. 5.3, LT4 h shows the highest and most stable crystal fraction.

At T=37 °C native, rendered fat shows only one small peak at about $2\theta \simeq 5$deg, which is most likely generated by remaining crystals of of triglycerides containing longer fatty acid chains. Most of the fat is molten and only 2.7 ± 0.6 % remains crystalline.

LTF2 shows already more peaks and a CFC of $12.9 \pm 2.0\,\%$, which become even more pronounced after 4 h treatment and a higher CFC of $18.3 \pm 3.3\,\%$ is measured. It is evident that lipase treatment generates peaks that resemble those of FGP, which shows a crystalline fat content of $5.6 \pm 1.9\,\%$. These peaks are temperature-persistent at temperatures experienced during oral processing.

The comparison of the change of the CFC shows this immediately. The decrease of the CFC for the different fats between 5 °C and 37 °C is quite different, The native duck fat drops by a factor of about 4.4, the FG fat by a much lower factor of 3.3. LTF2 drops decreases only by a factor o f 2.6, whereas LTF4 by the lowest factor 1.7.

5.3.2 Mechanical Methods

Mechanical properties were evaluated by employing rheological and texture analysis methods. The deformation dependent viscoelastic properties were measured by amplitude sweeps and gave the storage modulus (G'_0), loss modulus (G''), flow point and linear viscoelastic range (LVR). Their results are shown in Figure 5.7 with an example plot. The mean values are given in Table 5.5. All samples were measured in the heated and unheated state (except store bought FG samples) at 5 °C.

All heated pâtés (cooled to 5 °C) were examined by texture analysis, to determine maximum force (hardness), strain of maximum force and initial slope. Example plots of the heated samples are shown in Fig. 5.7 and the values are listed in Table 5.5.

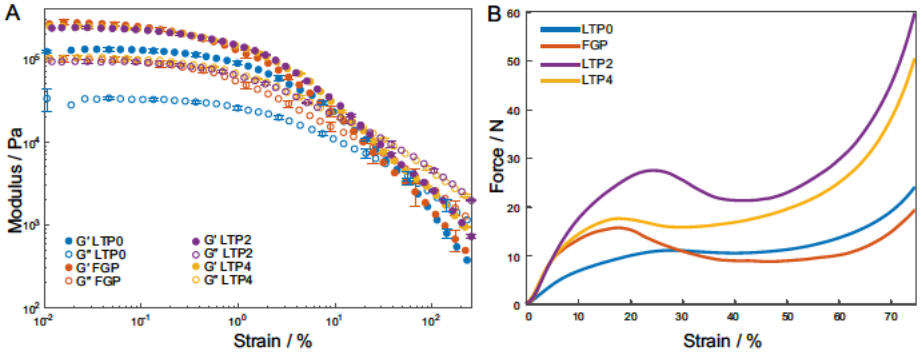

FIGURE 5.7: A: Amplitude sweeps of heated pâté samples. Filled circles for G' and unfilled for G'' The LTP0 is shown in blue and FGP in red. For the LTP2 purple is used and yellow for LTP4. In panel B, the texture measurements are shown as lines with the same color code. Typical curves are shown in this figure.

Rheology

The initial modulus G'_0 of the heated samples is about twice as high for the lipase treated pâtés (LTP2: 216.700 ± 12.300 Pa; LTP4: 247.400 ± 2.400 Pa) and Foie gras pâté (FGP: 256.800 ± 29.400 Pa) as for the LTP0 with 118.000 ± 16.200 Pa. A similar trend was observed for the LVR and the flow point. Starting from $0.46 \pm 0.09\,\%$ and $39.6 \pm 3.7\,\%$ for the LTP0 sample, both values decrease with lipase treated fat (LTP2: $0.25 \pm 0.06\,\%$ and $33.3 \pm 7.8\,\%$; LTP4: $0.14 \pm 0.02\,\%$ and $24.4 \pm 4.7\,\%$) and correspond

TABLE 5.5: Mechanical properties of pâté preparations with native duck fat (LTP0), Lipase treated fat (LTP2 and LTP4) and store bought foie gras pâté (n=3). All values are statistical significant due to ANOVA-test.

	LTP0[1]	**LTP2**	**LTP4**	**FGP**
G′/Pa heated[s]	118,000 ± 16,200	216,700 ± 12,300[c,d]	247,400 ± 2,400 [d,e]	256,800 ± 29,400 [c,e]
G′/Pa unheated[s]	17,400 ± 8,700[f]	28,600 ± 5,000[f]	86,100 ± 15,400	–
LVR/%	0.46 ± 0.09	0.25 ± 0.06[g]	0.14 ± 0.02[g,h]	0.12 ± 0.01[h]
Flow point/%	39.6 ± 3.7[i]	33.3 ± 7.8 [i,j,k]	24.4 ± 4.7 [j,k]	23.2 ± 1.1 [k]
Force/N	13.2 ± 3.6 [l,m]	26.4 ± 2.2[n]	19.6 ± 1.7 [m,n,o]	17.0 ±4.0 [n,o]
Compression/%	32.4 ± 3.7	22.3 ± 1.7[p,q]	20.5 ± 1.9 [q,r]	16.6 ± 0.6 [p,r]
Initial Slope[b]	0.4 ± 0.2	0.5 ± 0.3	0.7 ± 0.2	0.6 ± 0.3

[1]Values are already published in a previous paper[177]
[b]: not statistical significant according to ANOVA-test.
[c−r]: Value pairs not statistical significant due to Bonferroni-Post-hoc-test.

to the FGP values of 0.12 ± 0.01 % and 23.2 ± 1.1 % strain. As well as, the LVR and the flow point are shifted to lower strains, which indicates the same early structural breakup in the emulsion structure[155].

At first sight, the results for the amplitude sweeps expressed by the storage modulus G' appear very similar for FGP, LTP2 and LTP4. Nonetheless, significant distinctions can be identified. First, the increase in the linear modulus G' is for the LTP4 slightly higher than for LTP2, but both are close to the FGP sample, its modulus appears even slightly higher, but not significant. The shorter LVR of the LTP2 and LTP4 indicates a first irreversible breakdown of the emulsion structure comparable to the FGP samples. Whereas the flow point, the point where G'' exceeds G', for the lipase treated samples is also shifted to lower amplitudes and the LTP4 samples is matching the FGP sample. This indicates that the Lipase treated samples are, as well as the FGP samples, more rigid and less elastic and lower shear strains cause irreversible damage of the emulsion structure[155]. If even more shear applied to the samples, the LTP0 and FGP sample have a steeper decrease in moduli as the LTP2 and LTP4 samples.

However, since the fat embedding matrix is the physically same of all samples, the differences are caused by the lipase induced different fat structures, as already seen in the DSC and X-ray experiments. On the other hand, it is known that small structural changes are not always clearly exhibited by rheology[83, 145], therefore alternative methods, as compression tests, are needed. These results are shown in the following.

Texture analysis

As seen in Fig. 5.7 B, the LTP2 and LTP4 samples are significantly stiffer than the pâté with untreated duck fat LTP0. The force-strain curves of the lipase-treated pâtés also demonstrate higher values as the FGP, yet the shapes of the LTP2 and LTP4 curves are more closely aligned with the FGP as LTP0.

The differences of the mechanical properties in the samples are clearly more prominent in Fig.5.7 B as in Fig.5.7 A. The LTP0 samples reach a hardness of

13.2 ± 3.6 N and a strain at maximum force of 32.4 ± 3.7 %. The initial slope is 0.4 ± 0.2. The FGP samples are slightly harder with a maximum force of 17.0 ± 4.0 N, but the maximum force was already reached at 16.6 ± 0.6 % strain and an initial slope of 0.6 ± 0.3. Both lipase treated pâtés exceed the other samples in hardness with 26.4 ± 2.2 N (LTP2) and 19.57 ± 1.70 N (LTP4). The elongation of the maximum forces are closer to the FG pâté with 22.3 ± 1.7 % (LTP2) and 20.5 ± 1.9 % (LTP4) than to the control pâté LTP0.

The results of these compression experiments demonstrate the significant impact of the physical properties of fats following different lipase treatments. LTP0 demonstrates a continuous increase in force with increasing deformation, exhibiting a "plastic" softening between 30 % and 55 % strain. The maxima of LTP2 is even more pronounced compared to LTP4, but both exceed the maximum of FGP. Also, the deformation at the force maximum is shifted to shorter strains. LTP2 shows the highest value for force (hardness), whereas LTP4 shows lower values. The FGP and LTP4 samples tend to break shortly after the compression force is applied, which results in lower force and strain values compared to LTP0. The supplementary information includes photographs of the samples taken during and after the compression tests (see Fig. A.11, A.12 and A.13)

These mechanical results suggest already changes in the mouthfeel for the different pâtés. The LVR indicates the range of elastic recovery at given deformations. Although these values at very small strains appear irrelevant for oral processing they indicate the stability of the large-scale structure before becoming successively destroyed at larger strains, as shown by the stronger decrease in the moduli even above the flow point. Thus, LTP0 has the most linear elastic response, FGP the lowest. These properties correspond to the first contact in between tongue and palate at very small stains. At higher strains, respectively larger (horizontal) movements of the tongue the moduli decrease and the pâtés become more viscous, when $G' < G''$. Again, the flow point of LTP4 is closest to FGP, which means, that the breakdown of the underlying structure can be is similar in the mouth.

Concerning the linear elastic response, LTP4 comes closest to FGP. The hardness, e.g., when the tongue is pressed towards the palate, and expressed by the maximum force in Fig. 5.7 B, is larger for LTP2 and LTP4 as for FGP. The reason for this can be drawn back to the different crystal structure between FGP and LTP0,2,4. Obviously, these mechanical and thermal properties provide first indications for different oral sensations. As a corollary, the disparities in fat arrangement among the samples manifest as variations in fracture properties, as evidenced by the typical photographs provided in the Supplementary Information.

However, these results have to be discussed in the context with the large scale fat structure, which seems to contractive with the results from the fat analysis, the SFC and the WAXS results. Therefore additional information from CARS microscopy and the corresponding image analysis will shed more light on the behavior of the differently prepared pâtés.

5.3.3 CARS and image analysis

A preliminary observation suggests that the LTP2 sample exhibits a more compact particle network compared to the FG and LTP4 samples. Additionally, the pâtés LTP2 and LTP4 show significant differences in the fat structure and distribution, as shown in Fig. 5.8. The LTP2 samples show percolating fat clusters in many regions, in contrast to LTP4 samples. In the LTP2 samples only a few crystals appear in Image 1 (upper left) and 3. It seems that in LTP2 only limited regions show bright crystals. Whereas, for the LTP4 these highly crystalline structures were found distributed in large parts of the sample (Fig. 5.8 LTP4 picture 1-2). However, some fat crystals form larger clusters as well as the fat particles, as could be seen in the middle picture of LTP4 in Fig. 5.8.

LTP4 samples still contain larger clusters, but also connected regions (left and right) and appears less dense. Additionally, the LTP4 samples show very bright needle like crystals, which seem to join a larger amount of free fatty acids. This explains, most likely, the non percolating clusters, since the amorphous part of the fats decreases with the increasing CFC by higher lipase exposure time, as suggested by Fig. 5.5. A more detailed analysis shows the structural properties better. The images Fig. 5.8 and

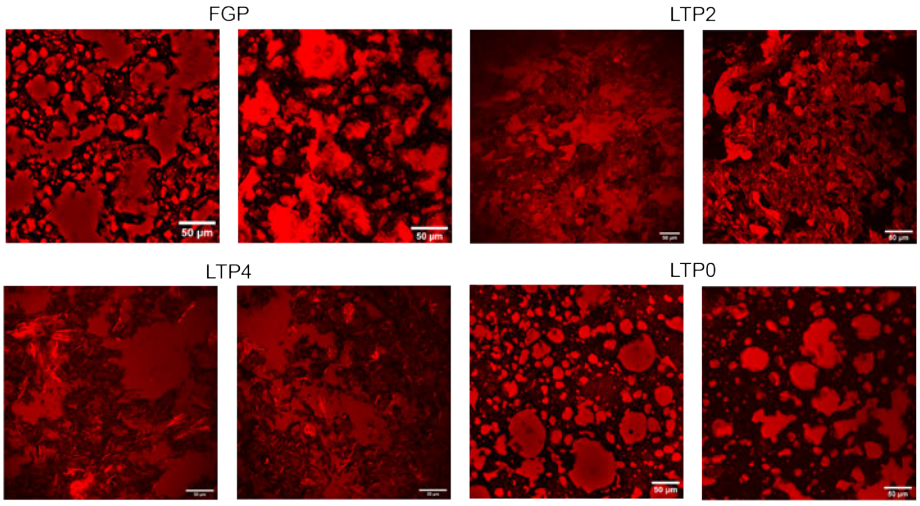

FIGURE 5.8: CARS Microscopy images of the different samples FGP and LTP2 are shown in the upper row. LTP4 and LTP0 are shown in the lower row. Fat particles are shown in red, the dark background is the aqueous phase and the bright red sharp "needles" are fat crystals. Whereas 2 h treatment provides more percolated clusters, 4 h treatment shows less

5.12 were analyzed to obtain the area weighted particle size distribution, shown in Fig. 5.9 and different shape descriptors as aspect ratio and circularity (see Fig. 5.10 and Table 5.6). They reveal differences between the FGP sample and the lipase treated samples. The FGP sample shows the larger fat particle clusters (see Fig. 5.12). The Lipase treated samples also have an emulsion structure made of interconnected fat particles.

The FGP shows a well-defined network of connected fat particles which are greater than 10.000 µm^2, which contribute with around 24 % of the total fat area of the samples. Between these percolating clusters are well separated medium size particles from 100 µm^2 to 10.000 µm^2, which cover most of the fat area. Compared to this, the LTP2 shows a percolating fat network as well. This covers nearly 50 % of the total fat, and is the most pronounced in all the samples, since it exceeds the area percentage for the largest particles of the other samples.

The area covered by particles greater than 10.000 µm^2 in the LTP4 sample is with 25 % close to the FGP sample and in the images similar connected fat clusters are visible (see also Fig. 5.8). The sample has the lowest area coverage with particles between 100 and 10.000 µm^2 and the highest of particles below 100 µm^2. This extended coverage comes from the high amount of small fat crystals, which are mostly present in the LTP4 samples due to the high CFC (see Fig. 5.6).

The increase of the aspect ratio (AR) and decrease in circularity of the LTP2 and LTP4 samples support the described emulsion structure. The extensive percolating network of particles is leading to elongated less round particles in the LTP2 sample (AR: 1.90 ± 0.71 Circ.: 0.63 ± 0.23), additionally the medium size particles are as well more elongated and rougher. For the LTP4 samples additionally, the amount of distinct needle like crystals are increasing the AR up to 2.05 ± 0.97 and decreases the circularity dramatically to 0.14 ± 0.08. Table 5.6 summarized these results.

Table 5.6: Mean area, median area and shape descriptors of LTP0, FG, LTP2 and LTP4 measurements. Statistical significance tested with ANOVA-test.

	LTP0	**FGP**	**LTP2**	**LTP4**
Mean Area/µm^2	118.5 ± 964.4	111.5 ± 876.5	135.9 ± 2161.3	9.10 ± 238.4
Median Area/µm^2	4.7	5.9	3.6	0.9
AR	1.4 ± 0.5	1.7 ± 0.6	1.9 ± 0.7	2.1 ± 0.9
Circ.	0.8 ± 0.2	0.7 ± 0.2	0.6 ± 0.2	0.1 ± 0.1

Particle size distribution

The mean and median particle size were evaluated from the images (Fig. 5.12). For all samples, except for the LTP4 sample, the mean particle size is between 110 µm^2 and 140 µm^2. The LTP4 has a mean particle area of 9.1 ± 238.4 µm^2 and a median of 0.9 µm^2, which indicates that more than half of the measured particles are less than 1 µm^2 in size. For a better comparison of the particle size distribution, the particles were weighted by the total fat area they covered in the samples. This complies to the percentage of the area covered by these respective size groups, as shown in Figure 5.9. The FGP, LTP2 and LTP4 samples show a similar particle size distribution compared to the LTP0 sample. The area covered by particles with a size of 1 µm^2 to 10 µm^2 is 2.6 % for LTP2 and 1.9 % smaller than in the LTP0 sample (5.0 %). However, here the LTP4 sample has with 11.7 % the highest coverage in this size group. In the next

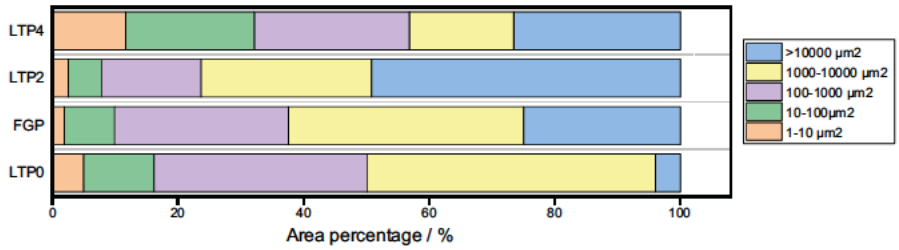

FIGURE 5.9: The figure shows the area weighted distribution of particle sizes for the different pâté samples. This resembles the percentage of area covered by particles of the respective size group.

size group, $10\,\mu m^2$ to $100\,\mu m^2$, the distribution within the samples is relatively close, with the LTP2 samples having the lowest coverage (5.3 %) and the LTP4 the highest (20.5 %). The same can be seen for the size group $100\,\mu m^2$ to $1000\,\mu m^2$, which covers an area of 15.9 % in the LTP2 samples, 24.7 % in the LT4 sample, 17.7 % in the FGP sample and 33.9 % in the LTP0 sample. For the LTP0 and FGP samples, particles between $1.000\,\mu m^2$ and $10.000\,\mu m^2$ have the largest area, covering 45.9 % and 37.4 % of the total area, respectively. Particles larger than $10.000\,\mu m^2$ cover 49.2 % of the fat area of the LTP2, whereas in the LTP0 only 4.0 % is covered by these large particles.

In the FGP and LTP4 samples, about a quarter of the area is covered with particles larger than $10.000\,\mu m^2$. The LTP2 and FG sample overall show similarities in the area weighted size distribution, whereas LTP0 shows a higher number of smaller particles and fewer particles with a size over $10.000\,\mu m^2$. The LTP4 sample distribution is quite different from the other samples because nearly a third of the area is covered with particles up to $100\,\mu m^2$. However, with 26.5 % it shows as many particles greater than $10.000\,\mu m^2$ as the FGP sample. The elevated crystalline fat content, in conjunction with the cleavage within the higher portion of C18:0, C18:1, and C16:0 fatty acids, facilitates the crystallization of more monocline crystals with minimal defects across numerous spatial positions, thereby reducing the intermediate cluster size to a range of $1.000\,\mu m^2$ to $10.000\,\mu m^2$. Consequently, the amorphous and partially molten fat clusters become less prominent as the exposure time to lipase is increased.

The results shown in Fig. 5.9 indicate a systematic decrease in the area covered by the particle group characterized by a particle size of $1.000\,\mu m^2$ to $10.000\,\mu m^2$ as the treatment time increases. In fact, the LTP4 attains a comparable regime at approximately 75 % of that of FGP, yet maintains a considerably more restricted profile. This lends further credence to the hypothesis that the occurrence of substantial crystal formation impedes the proliferation of large clusters and renders percolating structures less probable. Conversely, LPT2 appears to align more closely with the lower coverage regime. Nonetheless, the present analysis delineates methodologies for the implementation of lipase treatment, with consideration for activity and exposure time parameters, thereby ensuring the modulation of mouthfeel and the preservation of fat structure in a prescribed manner. A more detailed analysis of the shape descriptors, aspect ratio (AR) and circularity will underline these results.

Shape descriptors

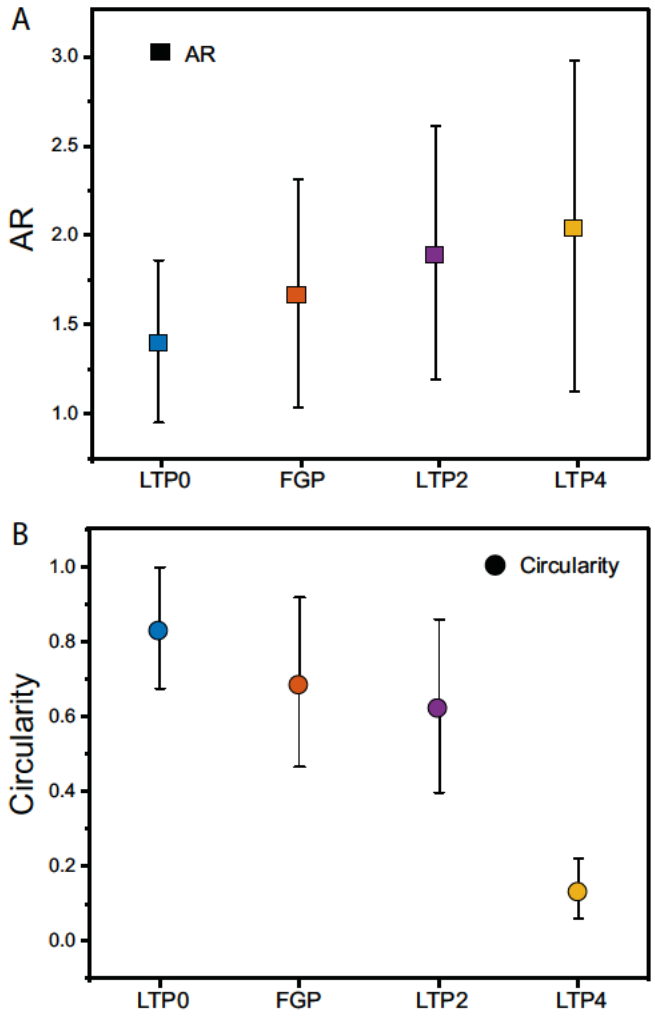

FIGURE 5.10: Shape descriptors derived from the image analysis of the different samples. In all panels the LTP0 sample is shown in blue, the FGP in red and LTP2 in purple and LTP4 in yellow. Panel A shows the aspect ratio, whereas the circularity is displayed in Panel B.

The aspect ratio (Table 5.6) of the samples was 1.7 ± 0.6 for the FGP and 1.9 ± 0.7 for the LTP2 and 2.1 ± 0.9 for LTP4, higher than the LTP0, which had an AR of 1.4 ± 0.5 (Fig. 5.10 A). Circularity showed lower values for the LTP2 and FGP (LTP2: 0.6 ± 0.2; FGP: 0.7 ± 0.2) compared to the control with 0.8 ± 0.2. However, it drastically drops for the LTP4 sample to 0.14 ± 0.08 (Fig 5.10 B). The increase in the aspect ratio is, due to the more irregular shaped particles of the LTP2 and LTP4 samples. For the LTP2 sample, mainly the bigger irregular particles, which build fat clusters, are responsible for the increase in the AR. For the LTP4 sample, the fat crystals also elongate the smaller particles because of the needle like structure. This effect is even more pronounced for the circularity, which is a measure of the particle roughness. In parallel with the AR, the LTP2 and FGP are less smooth due to larger fat clusters. Whereas, the circularity of the LTP4 sample drops by a factor of 4 compared to the

LTP2 sample. Here also the smaller fat crystals cause less round and rougher fat particles.

These results are most striking. As mentioned earlier[155], the formation of large, percolating, random fat clusters is imperative for a typical "foie gras mouthfeel". A shown in Fig. 5.9, this is the case for FGP and LTP2. Pure emulsions, like the LTP0, this cannot be the case for simple physical reasons. However, the samples for LTP4 show still regions with large percolating clusters, but also regions with non-connected clusters. Conversely, the CARS microscopy images manifest a conspicuously elevated concentration of stable crystals, manifest in the bright areas, which have a distinct impact on size distribution and shape descriptors of the LTP4 sample.

5.4 Converging discussion

In essence, it has been shown, how to produce foie gras of ducks or geese without any force-feeding and without using any additional components, such as stabilizers and emulsifier. The only ingredients are animal own rendered fat and their liver, which are side products of every duck or goose farm. Simple emulsions of these two components do not lead to satisfactory properties in texture and mouthfeel[155]. In this publication, the essential contribution of the existence of fat percolating fat network was already demonstrated.

Obviously, the lipase treatment of rendered fat provides by cleaving fatty acids from triglycerides a basis for forming connected fat networks with significant contributions to the mechanical properties, as demonstrated in Table 5.1 and Fig. 5.8.

To comprehensively interpret the underlying physics of these observations, it is imperative to retrace the steps involved in the preparation of the samples, except of FGP because this is based on a natural product and commercially sold. It has been shown, so far, that the fat structure plays the most important role in the mechanical properties and thus the mouthfeel.

This can be easily demonstrated when the mechanical properties of the uncross-linked, i.e. unheated pâtés are compared to those after heating, when the liver matrix becomes cross-linked. In the uncross-linked case, only the viscoelastic contribution and the mechanical impact of the fat is shown, especially, when all matrices are similar from composition and preparation. The corresponding experiments are shown in Fig. 5.11. The presence of differently structure fat networks alone change already the mechanical behavior as can be seen in the rheology of the non-heated, i.e., non cross-linked matrices, Fig. 5.11. The G_0' of the unheated pâtés increases steeply with longer treatment times and reaches $86.101 \pm 15.396\,\mathrm{Pa}$, almost five times that of the pâté with untreated fat (LTP0, see Table 5.5). Indeed, the moduli of the uncooked samples demonstrate a closer resemblance to those of FGP, nearly matching the cooked LTP0 sample. However, these results offer insights that are more profound and less straightforward. It is evident that the amplitude of storage and loss moduli increases in

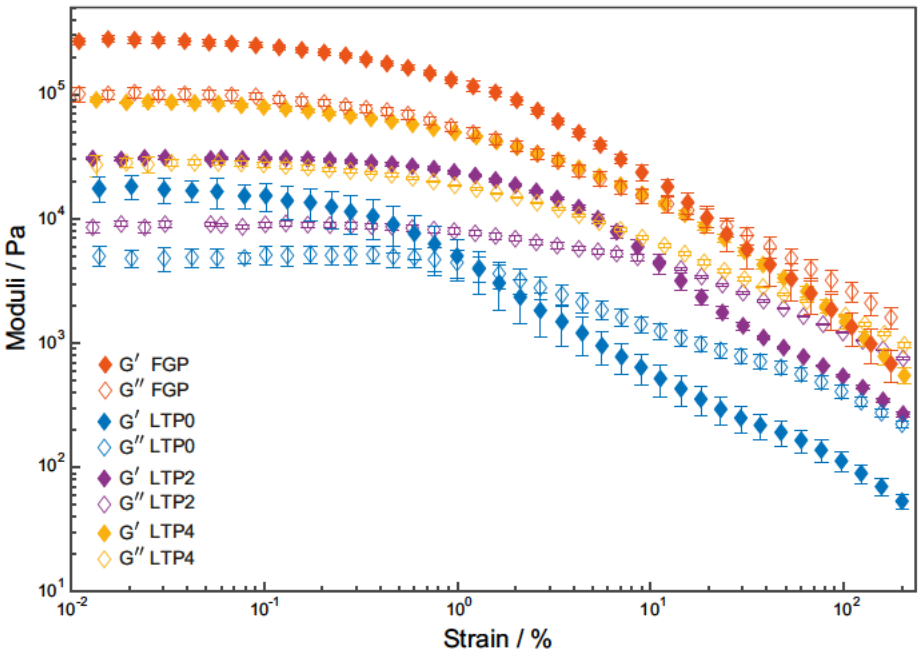

FIGURE 5.11: Amplitude sweep measurements of unheated pâté samples prepared with LTP0 (blue),LTP2, (purple) and LPT4 (yellow). FGP is shown in red for reference. The storage modulus G' is marked with filled and loss modulus G'' is marked with unfilled diamonds.

proportion to the duration of lipase exposure. LTP4 samples show the highest storage modulus, followed by LTP2 and pâte prepared by untreated rendered duck fat, LTP0.

At first sight this seems to contradict, what has been discussed before. However, the hard, stable and larger crystals after 4 h lipase treatment contribute as hard filler particles in the soft matrix strongly to the modulus of the uncross linked liver matrix[125]. The 2 h treatment does not show sufficiently high concentrations of such crystals, solid fat stays amorphous, but forms percolating clusters. Their different behavior indicates itself at different strains, especially at the stronger decrease of G' between 12 % and 110 %, which can be addressed to the successive breaking of the large clusters. The LTP4 pâté, however, shows a smooth decrease, the solid filler particles move within the deforming matrix. Indeed, at strains larger than 10 %, the unheated LTP4 follows already the curve of the cooked and FGP which demonstrates the high impact of the fat network.

Of course, other properties such as LVR, flow points etc, are very different, because of the different fat structures and the lack of cross-links. The heating induced cross-linking increases the modulus by ≈100 kPa for the LTP0. The further increase for LT 2 h and LT 4 h samples must consequently be caused the different large scale fat structures. The importance of those structures in the final pâtés after heating has been discussed already earlier by Via et al. [155]. To visualize the typical different structures in FGP and the lipase treated samples, CARS images were compared directly in Fig. 5.12 The images shown in Fig. 5.12 are directly extracted from typical CARS microscopy pictures shown already in Fig. 5.8, by removing the matrix background to

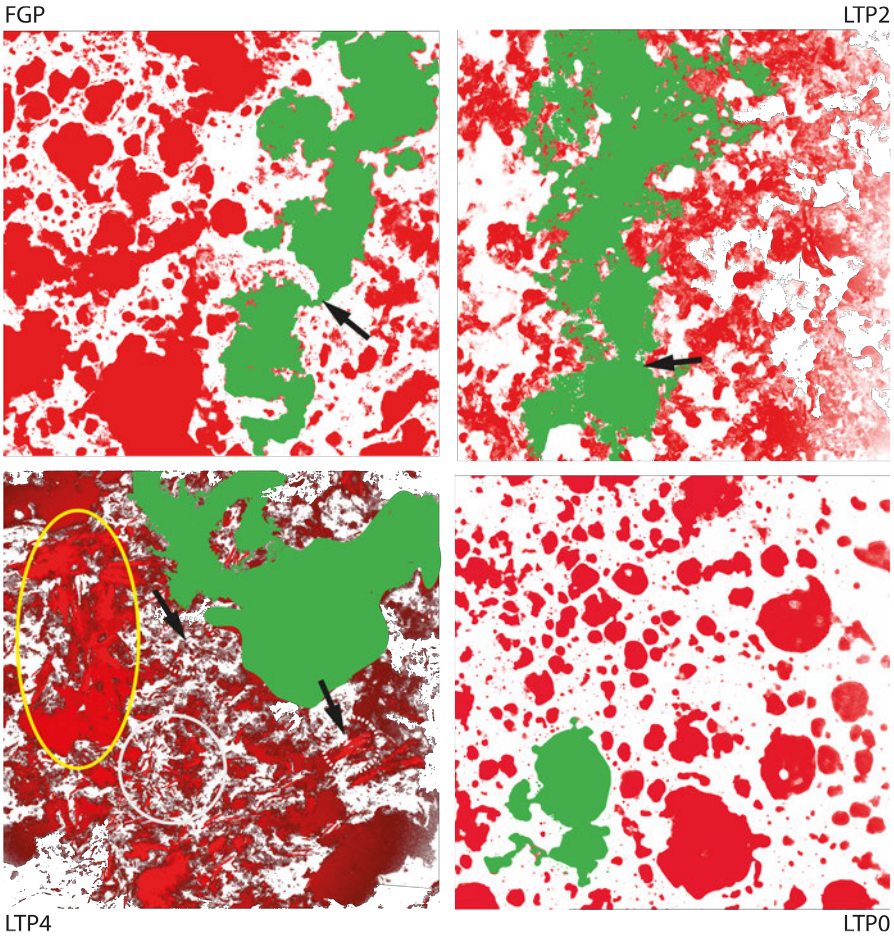

FIGURE 5.12: CARS Graphical visualization of the typical elements of the fats from microscopy images of FGP, LTP2, LTP4, LTP0. Large clusters are shown in green, weak bonds are indicated by black arrows. For LTP4 highly crystalline areas are indicated by gray circles. A highly crystalline cluster is surrounded by the yellow ellipse.

discuss the influence of the fat structure on the mechanical properties. The disparities are evident, yet the fat structures of FGP and LTP2 manifest a striking similarity. Both exhibit continuous, irregular fat aggregates with "weak" connections, designated as "hot bonds," demarcated by black arrows. These bonds undergo a sequential rupture when subjected to mechanical stress. As discussed already earlier[155], these processes are responsible for the texture of foie gras. LTP0 does not have comparable features, and thus the mechanical properties follow the rules of "hydrodynamic reinforcement" elastic matrices[125]. LTP4 has additional features. So called "hot bonds", which carry most of the compression stress [200] can also be found, but these are occasionally cross-linked via crystals, as marked by the arrow in Fig. 5.12. These correspond to the analogous curve progression observed in the mechanical compression data, but higher values for G'. LTP4 shows additional reinforcement by the solid crystals, which act as fiber-like reinforcing particles[201]. Additionally, large highly crystalline clusters, indicated by the yellow ellipse cause further reinforcing, at low strains as suggested in Fig. 5.7 A. Overall, the number of large connected cluster for LTP4 is reduced, since

more cleaved fatty acids crystallize, which suggests the at larger strains the elastic response of LTP4 becomes weaker compared to LTP2 and FGP, as also seen in Fig. 5.7.

Thus, these CARS data support systematically the observations in the mechanical experiment, shown in Fig. 5.7. The LTP2 sample shows the highest compression force of the samples, which is caused by the dense percolating network of the sample. Additional to force, which is needed to break the linked fat aggregates apart, an extensive amount of force is needed to move the particles along each other[155].

The compression of the LTP4 sample is closer to the FGP sample, as the emulsion structure resembles more the connected fat cluster of the FGP. However, the high crystal content of the LTP4 samples is responsible for a further increase in the maximum force, as the crystals act as hard filler particles. The low elastic behavior of the samples LTP4 and FGP (see LVR in Table 5.5) lead to breaking events of the random fat network and clusters after the maximum force is reached.

The influence of the emulsion structure on the amplitude sweeps is contrary to the results of the compression test, as shown in Fig. 5.7 B. Whereas, the short LVR values can be explained by the initial breaking of the fat particles at the connection points at low strains, which can be seen in the images above (see Fig. 5.12) However, in the rheology the FGP has with $G'(0)$ =256.800 ± 29.400 Pa the highest modulus of the samples and LTP2 ($G'(0)$ =216.700 ± 12.300 Pa) the lowest modulus. Considering the fat clusters the LTP2 should exceed the FGP samples. However, if shear stress is applied, the solid fat content contributes to the modulus as well (see Table 5.4)[188]. At 5 °C the solid fat content of the FGF is the highest with 57.9 ± 3.1 % and the lowest for the LTF2 sample (26.4 ± 4.2 %), which is even lower as for the LTF0 sample. However, the initial modulus of the LTF2 is around 100 kPa higher than for the LTP0 (see Table 5.5). This is compensated by the dense fat particle network of the LTP2 sample.

The other important impact of the lipase treatment is given by the restructuring of the rendered fat, which allows polymorphs of fat crystals, that are more stable and shifts the overall melting regime into the direction of the foie gras. This can be seen in the DSC experiments, at the results of WAXS and the persisting X-ray reflexes, which match those of FG at 37 °C, as shown in Fig. 5.6.

Finally, a cursory examination of the alterations in the modules of the rheometer during the process of heating is beneficial as shown in Fig. 5.13. At first sight the curves appear very different from FGP, however, a complete agreements cannot be expected, since the FGP is a natural product with a very different preparation history. Nevertheless useful features can be extracted, especially in the shaded temperature regime, which is most relevant for the mouthfeel. FGP shows a very distinct decrease of the storage modulus $G'(t, T)$ until complete melting of the fat, with a very pronounced shoulder between 35 min and 42 min. Both lipase treated samples exhibit a similar behavior, especially LTP4, which exhibits this pronounced shoulder, too.

The higher moduli of the two pâtés LTP2,4 between at $t \geq 13min$ is a consequence

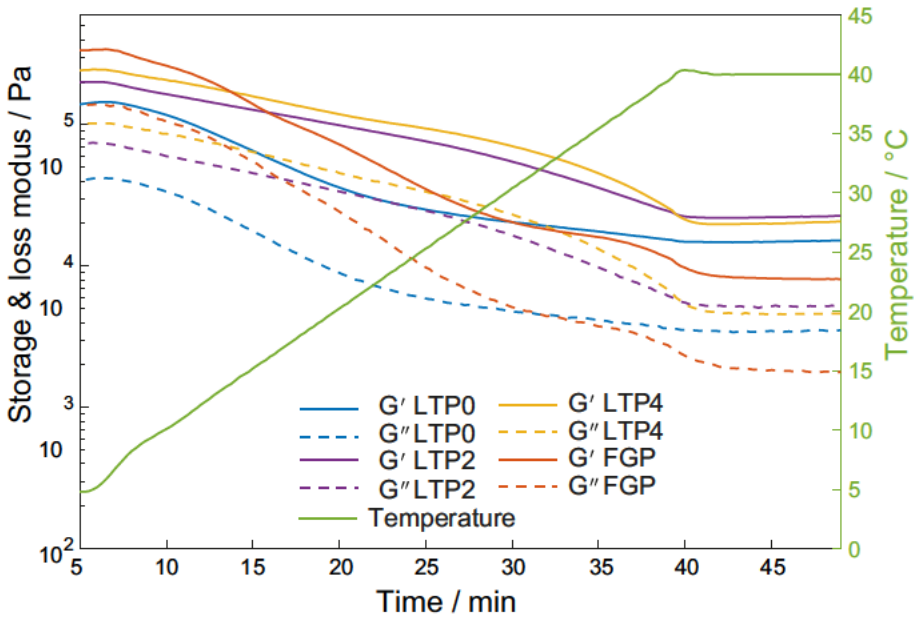

FIGURE 5.13: The moduli for FGP (red), LTP0 (blue), LTP2 (purple), and LTP4 (yellow) as a function of time under increasing temperature (green line), with a heating rate of 1 K/min.

of the hard crystals, which melt only around 40 °C and higher, completely, as seen in DSC experiments. As also seen in the CARS experiments, the crystals are more pronounced for LTP4 as for LTP2. Therefore, LTP4 contains a higher concentration of hard filler particles, which increase the modulus compared to LTP2. Despite the higher moduli of LPT2,4, the melting properties under shear show similar curve shapes in the temperature interval most relevant for oral processing.

In contrast, the simplest approach LTP0, the rendered fat emulsion, does not show any of these features. Even the overall decrease in $G'(t,T)$ remains very low. Simple heated emulsions cannot mimic FGP sufficiently.

A further question is raised by the DSC experiments, and it remains unresolved within the present investigation. The two melting peaks appearing after lipase treatment no. 12,13 and 14, 15 require higher latent heat to melt, as the fat in the foie gras pâté after force-feeding, as shown in Fig. 5.3. Fats and fat blends with high melting enthalpy may induce trigeminal cooling in the oral cavity[184, 202]. The fast melting process takes thermal energy out of the tongue at certain rates which are higher than the restoration by the blood circulation. The temperature may then fall below the thresholds of the trigeminal receptors TRPA1 (cold) a/or TRMP8 (cooling) which induces a cooling sensation. For fat crystals containing only C16 and C18 fatty acids this in unlikely, especially when the crystals are embedded in a water rich matrix formed by the liver proteins.

5.5 Conclusion

In conclusion, the large scale fat structure is a key element in the physical behavior of the pâtés and thus the resulting mouth feel and enjoyment. The application of lipase treatment has been demonstrated to reduce the necessity of force-feeding animals in the production of foie gras-like pâté, which exhibits comparable textural characteristics. The method of modifying the fat structure and, consequently, the textural properties of food has emerged as a promising avenue for further exploration, offering potential applications beyond the scope of this study.

Nevertheless, precise predictions for the technological formulations are nearly impossible to predict. The reasons are straightforward: lipases of varying origins, such as from plants, animals, microorganisms, or other sources, exhibit distinct variances in specific activities at particular process temperatures. Consequently, each lipase batch necessitates preliminary characterization. Notwithstanding, this investigation offers a universal strategy to produce non-force-fed foie gras, which is quasi equivalent to the original[103].

Consequently, the discussion has not addressed flavors and taste, as they do not induce substantial alterations in structural properties. Even when salts (ions) add up to the ionic part of the livers (mono- and bivalent ions, free alkaline and acidic amino acids), added salt is not able to change contributions in the large-scale structure of the fat network. Adding the spices and seasonings from standard (and non-standard) recipes will provide excellent culinary results. In addition, the lipase treatment shows also here its strong advantage. The lipase will cleave short chain fatty acids, fatty acids with equal and lower molecular weight than C 12 contribute to the typical smell of non-spiced foie gras[203]. The lipase treatment defines a solid fundament for foie gras production across various scales.

Supplementary Information

See the supplementary Information for exemplary NMR spectra of all samples. Also, an extended description of the DSC-measurements is presented there. As well as photographs of the samples during and after the compression test.

5.6 Acknowledgments

The project was gratefully funded by VAN HEES GmbH, Walluf, Germany and we acknowledge the materials supply and many discussions with Dr. Alexander Stephan. We would like to thank Robert Graf and Stefan Geiter for providing the NMR and XRD measurements and for their helpful support in the analysis of the data. The work was supported by the Villum Foundataion (Denmark), grant no. 00025414. We acknowledge the use of Danish Molecular Bio-Imaging Center, supported by the Novo Nordisk Foundation, grant no. NNF18SA0032928

Conflict of Interest

The authors have no conflicts to disclose.

Authors contribution

M.B.: sample preparation, texture analysis, rheology measurements, statistical analysis; manuscript draft; A.M.L.M:CARS imaging, image analysis, M.A.V.: CARS imaging, image analysis, M.P.C.: experimental design, interpretation, supervision, writing, manuscript review. T.A.V.: project idea, interpretation, model development, supervision, writing, manuscript review;vb

Data Availability Statement

The data that support the findings of this study are available from the corresponding author upon reasonable request.

Chapter 6

Comparison with a commercial available product

This chapter compares the lipase-treated pâtés from the previous chapter 5 with a commercial product also made without force-feeding. The product was also measured with amplitude sweeps and texture measurements were carried out. It was also imaged using CARS microscopy.

6.1 Comparison of LTP2, LTP4 and FGP to a commercial available product

At this point, it is interesting to compare the results of Chapter 5 with a commercially available product[34], CP. The fundamental difference is that the CP adjusts the elastic properties by adding gelatin, extracted from collagen rich duck parts, combining the liver with rendered fat. In Fig: 6.1 the mechanical measurements of LTP2, LTP4 and FGP samples are compared with those of the CP sample. In part A of Fig. 6.1 amplitude sweeps are shown. The CP sample has a $G'(0)$ of roughly 315.400 Pa and exceeds the FGP samples by ≈60 kPa (FGP: ≈256.800 Pa) and the LTP samples by roughly 70 kPa to 100 kPa (LTP2: ≈216.700 Pa; LTP4: ≈247.400 Pa; See Table 5.5). The LVR and flow point of the CP sample is with 0.18 % and 25.17 % Strain between those of the FGP and LTP4 on the one side and LTP2 on the other side. The LVR for the LTP4 and FGP sample is with 0.14 % 0.12 % shorter compared to the CP. As well as the flow points with 24.42 % and 23.2 %. This indicates that the high amount of gelatin produces a pâté which comes close to the FGP but shows clear rubber-like character. The decay of the pâté structure at higher strains has nearly the same slope for the LFP4 and FGP sample, whereas the CP structure breaks even faster apart and the LTP2 decay is less steep. Taking the texture measurements into account, the increase in the compression stress of the CP sample is the highest, which correlates with the rheological measurements. The LTP4 and LTP2 show a lower increase in the compression stress as the CP which is in line with the $G'(0)$ values. However, at around 7 % the compression stress exceeds the values of the other samples. Whereas the FGP shows a low increase in the compression stress below 2 % strain and increases then accordingly to the LTP4 and CP samples. Thus, the compression tests

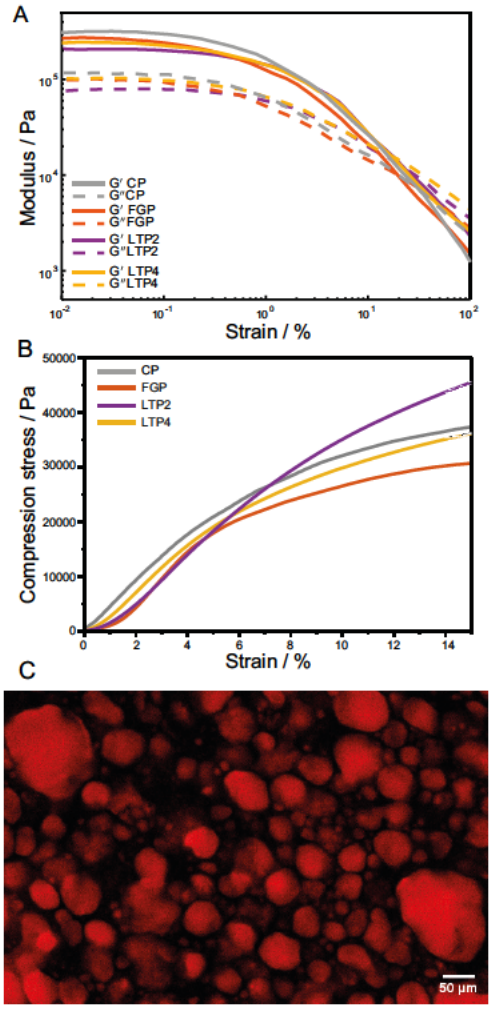

FIGURE 6.1: In Fig A. the amplitude sweeps of foie gras pâté (FGP in red), the lipase treated pâtés (LTP2 in purple; LTP4 in yellow) and the commercial product (CP in grey) are displayed. Fig part B displays the compression stress of the samples. Fig C. shows a CARS image of the commercial product.

should give the same trend as the amplitude sweeps in the low strain region, for these samples it is hardly possible because of the small LVR and rapid fragmentation of the cluster network, especially for the LTP sample. As mentioned above, the resolution of the compression test is not sufficient in these low strain regions. In Fig 6.1 C a CARS image of the CP sample is shown. Compared to the LTP and FGP samples the fat particles appear round and well separated, more like in the LTP0 sample. As discussed previously in chapter 3 and 4, the fat particles contribute only marginal to the mechanical behavior, which is mainly introduced by the tight gel network formed by gelatin.

Chapter 7

Conclusion and Outlook

7.1 Conclusion

The main objective of the thesis was to gain a better understanding of the physical properties of semi-solid protein emulsions, better known as duck liver paté and foie gras paté, with the aim of mimicking foie gras paté without the need to force-feed the animals. Characterisation using various techniques provided some unique insights into the physical properties and microstructure of the systems. In particular, the comparison of foie gras pâté and a simple 'home-made' duck liver pâté, consisting of rendered duck fat and liver, led to two different approaches for influencing the properties of the liver-based emulsion. Firstly, the systematic use of different emulsifiers and, secondly, the approach of modifying the texture of a semi-solid pâté by changing the fat structure itself with lipase treatment. In chapter 3 of this thesis, two commercially available foie gras pâtés and a control pâté, prepared with spontaneously fattened duck liver, rendered duck fat and water, were subjected to various textural measurements. The foie gras pâté and the control pâté showed clear differences in viscoelastic behaviour and in compression tests. The storage modulus G' as well as the hardness of the foie gras samples are one order of magnitude higher compared to the control pâté. Other differences were observed in the LVR and cross point, indicating a faster degeneration of the fat and protein network in the foie gras pâté samples. This result was supported by CARS microscopy imaging of the fat structure, which showed a wide percolation of fat particle clusters in the foie gras samples. Such clusters had not been previously reported and were not found in the control pâté. A key understanding of the work in this chapter 3 was that these unique structures support the protein network as 'hard' filler particles and increase both the storage modulus (G') and hardness. Conversely, the weak links between these particles break easily under shear or compression, causing the rapid irreversible collapse of the structure. A first approach, presented in chapter 3, to influence the basic semi-solid liver emulsion was the use of three different emulsifiers with different properties. Three different concentrations of collagen, sodium stearate and MDG were used. Each of these additives has a different functionality and therefore an individual molecular interaction with the emulsion system. Using the same characterisation methods as established in the work of chapter 3, each system was characterised and showed distinct effects. Each emulsifier increased the G' by

about 20 % without showing any systematic manner. However, each emulsifier showed a clear effect on some textural parameters. Increasing collagen concentration leads to an increase in LVR and hardness of the samples. Supported by the increase in compressive strain at maximum force, the samples behave more elastically compared to the other samples. Sodium stearate has a major effect on the compressibility (hardness and strain of maximum force) of the samples. It introduces negative charges on the surface of the fat droplets, which increases the electrostatic repulsion of the particles. This effect was less pronounced in the rheological measurements. The polar MDG had no significant effect on the rheological and textural properties in the heated state, but in the unheated state the initial G' decreased with increasing concentration. Particle analysis of the CARS microscopy images showed that all additives had a similar effect on fat particle structure. The particle sizes decrease over all concentrations and the area weighted particle size distribution becomes narrower. The particle shapes are slightly less round, but the interparticle distance decreases with emulsifiers compared to the control sample.The CARS microscopy images show an emulsion with well separated particles. A successful approach by treating the duck fat with lipase to improve the rheological and textural properties to match the properties of foie gras pâté is presented in chapter 5. Further investigation of the differences between foie gras pâté and a control pâté revealed a different melting profile in the DSC curves, solid fat content and fatty acid profile. To modify the properties of the native duck fat, a lipase treatment was applied to the fat. The lipase cleaves the fatty acids from the triglycerides, leaving a mixture of mono-, di- and triglycerides and free fatty acids, depending on the treatment time. This treatment changes the properties of the fat, such as melting profile, solid and crystalline fat content, without changing the fatty acid profile of the fat. Compared to the extracted fat from foie gras pâté, the lipase-treated fat matches the melting profile and the solid fat content and exceeds the crystalline fat content. Pâtés made with the lipase-treated fat have similar rheological and textural properties compared to foie gras samples. The microstructure of the lipase treated sample also showed the percolating fat clusters described in chapter 3 and small crystals of free fatty acids depending on the treatment time. Overall, this work has shown that first understanding an emulsion-based food system is key to influencing its properties in a desired way. It has shown that the unique fat particle structure of foie gras pâté is responsible for the difference in texture. It also provided important insights into the use of emulsifiers and their interactions in protein-based emulsions. This knowledge led to a new and very successful approach to mimicking foie gras pâté, as the following excursus shows.

7.2 Outlook

In the future, the work presented in this thesis can be continued in two different ways. Firstly, the characterisation of these spreadable liver-based emulsions can be improved and further techniques applied. As mentioned above, the structure of the fat particles

is the main influence on the textural properties of semi-solid emulsions. It is therefore interesting to complement rheological and textural measurements with tribological measurements to gain insight into the friction of the system. This will lead to further knowledge about the emulsion stability and fat release in these pâté-like systems[145]. This method could be applied to all the systems presented in this work, and it would underline the findings if the differences between the foie gras pâté respectively lipase treated pâté and untreated pâtés, which are mainly discussed in chapter 3 and 5, are supported by tribology. In addition, the samples could be assessed by Stimulated Raman Scattering (SRS) microscopy to gain further insight. This technique can provide contrast-enhanced images with better spectral resolution, and it may therefore be possible to image the protein structure in the aqueous phase[204]. It would be useful to capture a stack of images in the z-direction and combine them into a three-dimensional model of the samples. This could improve the understanding of the interconnected fat particle clusters. The systematic approach of the emuslion system presented in chapter 4 could be applied to other concentrations, but other emulsifiers are also worth investigating in this way to gain insight into their influence on the physicochemical properties of semi-solid meat emulsions. Similarly, the results in chapter 4 provide a basis for investigating syneresis or negative interactions between emulsifiers when they are used in combination. Secondly, the lipase treatment discussed in chapter 5 could be further refined and in order to turn it into a product upscaling tests and further methods such as sensory panels are required[88, 103]. A further comparison with other foie gras pâté analogues[33, 34] would also be interesting, in particular with a pâté made using laboratory grown liver[205]. As suggested in other publications[35, 64], this method could be applied to other types of fats and oils to improve food systems such as (vegetarian/vegan) spreads and pastes. For example, a vegan foie gras paté could be developed using lipase textured vegetable oil or fat and plant based proteins. This would further improve animal welfare by eliminating not only the need for force-feeding, but also the need to slaughter animals.

Bibliography

(1) Ugalde-Benítez, V. *Handbook of Meat and Meat Processing,* **2012**, 447–456.

(2) Feiner, G., *Meat products handbook: Practical science and technology*; Elsevier: 2006.

(3) Totosaus, A.; Pérez-Chabela, M. L. *Handbook of food science, technology, and engineering* **2006**, *4*, 167–1.

(4) Steen, L.; Fraeye, I.; De Mey, E.; Goemaere, O.; Paelinck, H.; Foubert, I. *Food and Bioprocess Technology* **2014**, *7*, 496–505.

(5) Steen, L.; Glorieux, S.; Goemaere, O.; Brijs, K.; Paelinck, H.; Foubert, I.; Fraeye, I. *Food and Bioprocess Technology* **2016**, *9*, 970–980.

(6) Xu, W.; Nikolov, A.; Wasan, D. T. *Journal of food engineering* **2005**, *66*, 97–105.

(7) Jaud, D; Schneider, K; Hilmes, C; CHEONG, S.-H.; FISCHER, A *Fleischwirtschaft (Frankfurt)* **1998**, *78*, 664–670.

(8) Schneider, K; Jaud, D; Hilmes, C.; CHEONG, S.-H.; Fischer, A *Fleischwirtschaft (Frankfurt)* **1998**, *78*, 464–470.

(9) Pyrcz, J.; Pietronczyck, K; Kowalski, R.; Danyluk, B. *Electronic Journal of Polish Agricultural Universities* **2006**, *9*.

(10) Steen, L.; Fraeye, I.; Goemaere, O.; Sifre, L.; Goderis, B.; Paelinck, H.; Foubert, I. *Food and bioprocess technology* **2014**, *7*, 2855–2864.

(11) Tiensa, B. E.; Barbut, S.; Marangoni, A. G. *Food research international* **2017**, *100*, 558–565.

(12) Pětová, M.; Polášek, Z.; Lapčíková, B.; Lapčík, L.; Buňková, L.; Pospiech, M.; Foltin, P.; Talár, J.; Salek, R. N.; Kůrová, V., et al. *LWT* **2024**, *191*, 115614.

(13) Delgado-Pando, G.; Cofrades, S.; Ruiz-Capillas, C.; Triki, M; Jiménez-Colmenero, F. *Meat Science* **2012**, *92*, 44–52.

(14) Barbut, S.; Wood, J.; Marangoni, A. *Meat Science* **2016**, *122*, 155–162.

(15) Barbut, S.; Marangoni, A. G.; Thode, U.; Tiensa, B. E. *Journal of Food Science* **2019**, *84*, 2646–2651.

(16) Barbut, S.; Tiensa, B. E.; Marangoni, A. G. *LWT* **2021**, *139*, 110428.

(17) Županjac, M.; Ikonić, P.; Šojić, B.; Đermanović, B. *Scientific journal" Meat Technology"* **2023**, *64*, 416–421.

(18) Cerón-Guevara, M. I.; Santos, E. M.; Lorenzo, J. M.; Pateiro, M.; Bermúdez-Piedra, R.; Rodríguez, J. A.; Castro-Rosas, J.; Rangel-Vargas, E. *International Journal of Food Science and Technology* **2021**, *56*, 6171–6181.

(19) Rezler, R.; Krzywdzińska-Bartkowiak, M.; Piątek, M. *Lwt* **2021**, *135*, 110264.

(20) Vargas-Ramella, M.; Lorenzo, J. M.; Zamuz, S.; Montes, L.; López, E. M. S.; Moreira, R.; Franco, D. *Lwt* **2022**, *163*, 113522.

(21) Kolpas, N., *Foie Gras: A Global History*; Reaktion Books: 2021.

(22) Bonnefont, C.; Molette, C.; Lavigne, F.; Manse, H.; Bravo, C.; Lo, B.; Rémignon, H.; Arroyo, J.; Bouillier-Oudot, M. *Poult Sci.* **2019**, *98*, 5724–5733.

(23) Lavigne, J. *Gastronomica: The Journal of Food and Culture* **2021**, *21*, 20–31.

(24) Guémené, D.; Guy, G. *World's Poultry Science Journal* **2004**, *60*, 210–222.

(25) Baéza, E.; Marie-Etancelin, C.; Davail, S.; Diot, C. *INRAE Productions Animales* **2013**, *26*, 403–414.

(26) Rochlitz, I.; Broom, D. *Animal Welfare* **2017**, *26*, 135–149.

(27) Chapuis, H.; Lagüe, M; Bonnefont, C. M.; David, I; Bernadet, M.-D.; Hazard, A.; Gilbert, H. *animal* **2024**, *18*, 101234.

(28) Wilhelm, R.; Ternes, W. *FleischWirtschaft* **2016**, *3*, 116–123.

(29) Delpont, M.; Blondel, V.; Robertet, L.; Duret, H.; Guerin, J.-L.; Vaillancourt, J.-P.; Paul, M. C. *Preventive veterinary medicine* **2018**, *158*, 78–88.

(30) Théron, L.; Vénien, A.; Jamme, F.; Fernandez, X.; Peyrin, F.; Molette, C.; Dumas, P.; Réfrégiers, M.; Astruc, T. *Journal of agricultural and food chemistry* **2014**, *62*, 5954–5962.

(31) Théron, L.; Astruc, T.; Bouillier-Oudot, M.; Molette, C.; Vénien, A.; Peyrin, F.; Vitezica, Z.; Fernandez, X. *Meat Sci.* **2011**, *89*, 377–383.

(32) Carrillo, F. S.; Saucier, L.; Ratti, C. *International Journal of Food Properties* **2017**, *20*, 573–584.

(33) Foie, H. Happy Foie product page, `https://happyfoie.com/collections/happy-foie-all`, Accessed: (Dec. 11th 2024).

(34) Terjung, N., EU Patent No. EP 3 556 224 B1, 16 04 2019.

(35) Nicholson, R. A.; Marangoni, A. G. *Nature Food* **2020**, *1*, 684–692.

(36) Goodarzi, F.; Zendehboudi, S. *The Canadian Journal of Chemical Engineering* **2019**, *97*, 281–309.

(37) Ogemdi, I. K. *Colloid Surf. Sci* **2019**, *4*, 24.

(38) Dickinson, E., *Food emulsions and foams*; Elsevier: 1987.

(39) Vilgis, T. A. *Reports on Progress in Physics* **2015**, *78*, 124602.

(40) Jiménez-Colmenero, F. *Food Research International* **2013**, *52*, 64–74.

(41) Shao, P.; Feng, J.; Sun, P.; Xiang, N.; Lu, B.; Qiu, D. *Food Research International* **2020**, *137*, 109376.

(42) McClements, D., *Food Emulsions: Principles, Practices, and Techniques, Third Edition*; CRC Press: 2015.

(43) Israelachvili, J. N., *Intermolecular and surface forces*; Academic press: 2011.

(44) Kabalnov, A. S.; Shchukin, E. D. *Advances in colloid and interface science* **1992**, *38*, 69–97.

(45) Weers, J. G. In *Modern Aspects of Emulsion Science*; The Royal Society of Chemistry: 1998.

(46) Kabalnov, A. S. In *Modern Aspects of Emulsion Science*; The Royal Society of Chemistry: 1998.

(47) Sacanna, S.; Kegel, W.; Philipse, A. *Physical review letters* **2007**, *98*, 158301.

(48) Hasenhuettl, G. L.; Hartel, R. W., *Food emulsifiers and their applications*; Springer: 2008; Vol. 19.

(49) Narsimhan, G.; Wang, Z. In *Food emulsifiers and their applications*; Springer: 2008; Chapter Guidelines for processing emulsion-based foods, pp 349–394.

(50) Leser, M. E.; Sagalowicz, L.; Michel, M.; Watzke, H. J. *Advances in colloid and interface science* **2006**, *123*, 125–136.

(51) Hasenhuettl, G. L. In *Food emulsifiers and their applications*; Springer: 2008; Chapter Synthesis and commercial preparation of food emulsifiers, pp 11–39.

(52) Meena, S. K.; Celiksoy, S.; Schäfer, P.; Henkel, A.; Sönnichsen, C.; Sulpizi, M. *Physical Chemistry Chemical Physics* **2016**, *18*, 13246–13254.

(53) Scholfield, C. *Journal of the American Oil Chemists' Society* **1981**, *58*, 889–892.

(54) Berg, J. M.; Tymoczko, J. L., et al., *Stryer biochemie*; Springer: 2018; Vol. 8.

(55) Dickinson, E. *Food hydrocolloids* **2003**, *17*, 25–39.

(56) Zouari, N.; Fakhfakh, N.; Amara-Dali, W. B.; Sellami, M.; Msaddak, L.; Ayadi, M. *Food and Bioproducts processing* **2011**, *89*, 142–148.

(57) Dickinson, E. *Food hydrocolloids* **2009**, *23*, 1473–1482.

(58) Velikov, K. P.; Velev, O. D. In *Colloid stability and application in pharmacy*; Wiley Online Library: 2007, pp 277–306.

(59) Marina, P. F.; Cheng, C.; Sedev, R.; Stocco, A.; Binks, B. P.; Wang, D. *Angewandte Chemie International Edition* **2018**, *57*, 9510–9514.

(60) Chevalier, Y.; Bolzinger, M.-A. *Colloids and Surfaces A: Physicochemical and Engineering Aspects* **2013**, *439*, 23–34.

(61) Kargar, M.; Fayazmanesh, K.; Alavi, M.; Spyropoulos, F.; Norton, I. T. *Journal of colloid and interface science* **2012**, *366*, 209–215.

(62) Belitz, I. H.-D.; Grosch, I. W., *Food chemistry*; Springer Science & Business Media: 2013.

(63) Jü Figure Triglyceride Hydrogenation V.2 Accessed: (Apr. 14th 2025), Wikimedia Commons, `https://commons.wikimedia.org/wiki/File:Triglyceride_Hydrogenation_V.2.svg`.

(64) Nicholson, R. A.; Marangoni, A. G. *Current Research in Food Science* **2021**, *4*, 163–174.

(65) Sato, K. *Chemical engineering science* **2001**, *56*, 2255–2265.

(66) Knoester, M; De Bruijne, P; Van Den Tempel, M *Chemistry and Physics of Lipids* **1972**, *9*, 309–319.

(67) Wright, A.; Scanlon, M.; Hartel, R.; Marangoni, A. *Journal of food science* **2001**, *66*, 1056–1071.

(68) Tang, D.; Marangoni, A. G. *Advances in colloid and interface science* **2006**, *128*, 257–265.

(69) Shih, W.-H.; Shih, W. Y.; Kim, S.-I.; Liu, J.; Aksay, I. A. *Physical review A* **1990**, *42*, 4772.

(70) Wu, H.; Morbidelli, M. *Langmuir* **2001**, *17*, 1030–1036.

(71) EC 3.1.1.3 nomenclature homepage Accessed: (Apr. 8th 2025), International Union of Biochemistry and Molecular Biology, `https://iubmb.qmul.ac.uk/enzyme/EC3/1/1/3.html`.

(72) McDonald, A. G.; Tipton, K. F. *The FEBS journal* **2023**, *290*, 2214–2231.

(73) Chandra, P.; Enespa; Singh, R.; Arora, P. K. *Microbial cell factories* **2020**, *19*, 1–42.

(74) Sharma, A.; Chaurasia, S. P.; Dalai, A. K. *Catalysis today* **2013**, *207*, 93–100.

(75) Houde, A.; Kademi, A.; Leblanc, D. *Applied biochemistry and biotechnology* **2004**, *118*, 155–170.

(76) Mezger, T. G., *Das Rheologie Handbuch: 5.* Farbe Und Lack: 2016.

(77) Willenbacher, N.; Georgieva, K. In *Product Design and Engineering*; John Wiley & Sons, Ltd: 2013; Chapter 1, pp 7–49.

(78) Mezger, T. G. et al., *The rheology handbook*; 9783748600367; Vincentz Network Hannover, Germany: 2012; Vol. 10.

(79) Li, S.; Ni, F.; Dong, Q.; Zhao, Z.; Ma, X. *International Journal of Pavement Engineering* **2021**, *22*, 87–96.

(80) Pons, M; Fiszman, S. *Journal of texture studies* **1996**, *27*, 597–624.

(81) Szczesniak, A. S. *Journal of food science* **1963**, *28*, 385–389.

(82) Bourne, M. *Journal of food science* **1968**, *33*, 223–226.

(83) Toultchinski, P.; Vilgis, T. A. *Physics of Fluids* **2024**, *36*.

(84) Trinh, K. T.; Glasgow, S. In *Proceedings of the Chemeca*, 2012; Vol. 2012, pp 23–26.

(85) Höhne, G. W. H.; Hemminger, W.; Flammersheim, H.-J., et al., *Differential scanning calorimetry*; Springer: 2003; Vol. 2.

(86) Gill, P.; Moghadam, T. T.; Ranjbar, B. *Journal of biomolecular techniques: JBT* **2010**, *21*, 167.

(87) Drebushchak, V. *Journal of thermal analysis and calorimetry* **2012**, *109*, 545–553.

(88) Baechle, M.; Marques, A. M. L.; Via, M. A.; Clausen, M. P.; Vilgis, T. A. *Physics of Fluids* **2025**, *37*, 037196.

(89) Kong, Y; Hay, J. *European Polymer Journal* **2003**, *39*, 1721–1727.

(90) Evans, C. L.; Xie, X. S. *Annu. Rev. Anal. Chem.* **2008**, *1*, 883–909.

(91) Krafft, C.; Dietzek, B.; Schmitt, M.; Popp, J. *Journal of biomedical optics* **2012**, *17*, 040801–040801.

(92) Dovbeshko, G.; Gnatyuk, O.; Dementjev, A.; Rutkauskas, D.; Kovalska, E.; Baldycheva, A.; Ilchenko, O.; Krasnenkov, D.; Kaplas, T. *FlatChem* **2021**, *27*, 100243.

(93) Hatzakis, E. *Comprehensive reviews in food science and food safety* **2019**, *18*, 189–220.

(94) Spyros, A.; Dais, P., *NMR spectroscopy in food analysis*; Royal Society of Chemistry: 2012.

(95) Bhande, S. S.; Bhosale, S. In *Nanomaterials for Sustainable Development: Opportunities and Future Perspectives*, Mane, R. S., Sharma, R. P., Kanakdande, A. P., Eds.; Springer Nature Singapore: Singapore, 2023, pp 25–63.

(96) Laws, D. D.; Bitter, H.-M. L.; Jerschow, A. *Angewandte Chemie International Edition* **2002**, *41*, 3096–3129.

(97) Asakura, T.; Ando, I., *Solid state NMR of polymers*; Elsevier: 1998; Vol. 84.

(98) Kiss Figure NMR Accessed: (Apr. 15th 2025), Technology Networks, `https://www.technologynetworks.com/analysis/articles/nmr-spectroscopy-principles-interpreting-an-nmr-spectrum-and-common-problems-355891`.

(99) Calligaris, G. A.; da Silva, T. L.; Ribeiro, A. P. B.; Dos Santos, A. O.; Cardoso, L. P. *Chemistry and physics of lipids* **2018**, *212*, 51–60.

(100) De Jeu, W. H., *Basic X-ray scattering for soft matter*; Oxford University Press: 2016.

(101) M., M. Figure Bragg Accessed: (Apr. 14th 2025), Wikimedia Commons, `https://commons.wikimedia.org/wiki/File:Bragg.svg`.

(102) DrBoStefanov Figure diffractometer Accessed: (Apr. 14th 2025), Wikimedia Commons, `https://commons.wikimedia.org/wiki/File:XRD_diffractometer.svg`.

(103) Vilgis, T. A.; Baechle, M., EP priority application filed 5.12.2023, PCT application filed 5.12.2024, 5 12 2023.

(104) Marangoni, A. G.; Wesdorp, L. H., *Structure and properties of fat crystal networks*; CRC Press: 2012.

(105) Chen, J.; Rosenthal, A. In *Modifying Food Texture*, Chen, J., Rosenthal, A., Eds.; Woodhead Publishing Series in Food Science, Technology and Nutrition; Woodhead Publishing: 2015, pp 3–24.

(106) Foegeding, E.; Daubert, C.; Drake, M.; Essick, G.; Trulsson, M.; Vinyard, C.; Van de Velde, F. *Journal of Texture Studies* **2011**, *42*, 103–129.

(107) Pedersen, M. T.; Hansen, P. L.; Clausen, M. P. *International Journal of Food Design* **2021**, *6*, 153–180.

(108) Carrillo, F. S.; Saucier, L.; Ratti, C. *International Journal of Food Properties* **2017**, *20*, 573–584.

(109) Mandigo, R.; Esquivel, O. In *Encyclopedia of Meat Sciences, vol. 1: Chemistry and Physics of Comminuted Products*; Elsevier: 2014, pp 283–288.

(110) Allais, I. In *Handbook of Meat Processing*; John Wiley & Sons, Ltd: 2010; Chapter 7, pp 143–168.

(111) Wu, M.; Xiong, Y. L.; Chen, J.; Tang, X.; Zhou, G. *Journal of Food Science* **2009**, *74*, E207–E217.

(112) Fernandez, X; Lazzarotto, V; Bernadet, M.-D.; Manse, H *Poultry Science* **2019**, *98*, 6149–6160.

(113) Youssef, M.; Barbut, S. *Meat Science* **2009**, *82*, 228–233.

(114) Youssef, M.; Barbut, S. *Journal of Food Science* **2010**, *75*, S108–S114.

(115) Han, M.; Clausen, M. P.; Christensen, M.; Vossen, E.; Van Hecke, T.; Bertram, H. C. *Food Funct.* **2018**, *9*, 4017–4027.

(116) Roeffaers, M.; Zhang, X.; Freudiger, C.; Saar, B.; Xie, X.; van Ruijven, m.; van Dalen, G.; Xiao, C. *Journal of Biomedical Optics* **2011**, *16*, 1–6.

(117) Meyer, T.; Akimov, D.; Tarcea, N.; Chatzipapadopoulos, S.; Muschiolik, G.; Kobow, J.; Schmitt, M.; Popp, J. *The journal of physical chemistry.* **2008**, *112*, 1420–1426.

(118) Terrasa, A.; Dello Staffolo, M.; Tomás, M. *LWT - Food Science and Technology* **2016**, *66*, 678–684.

(119) Schindelin, J. E. et al. *Nature Methods* **2012**, *9*, 676–682.

(120) Huang, L.-K.; Wang, M.-J. J. *Pattern Recognition* **1995**, *28*, 41–51.

(121) Lo, B.; Marty-Gasset, N.; Pichereaux, C.; Bravo, C.; Manse, H.; Domitile, R.; Rémignon, H. *Frontiers in Physiology* **2020**, *11*.

(122) Vilgis, T. A.; Heinrich, G.; Klüppel, M., *Reinforcement of polymer nano-composites: theory, experiments and applications*; Cambridge University Press: 2009.

(123) Huber, G.; Vilgis, T. A.; Heinrich, G. *Journal of Physics: Condensed Matter* **1996**, *8*, L409.

(124) Joshi, B.; Beccard, S.; Vilgis, T. A. *Current Opinion in Food Science* **2018**, *21*, 39–45.

(125) Huber, G.; Vilgis, T. A. *Macromolecules* **2002**, *35*, 9204–9210.

(126) Cummings, C. G.; Hamilton, A. D. *Current opinion in chemical biology* **2010**, *14*, 341–346.

(127) Kumar, S.; Nussinov, R. *ChemBioChem* **2002**, *3*, 604–617.

(128) Vilgis, T. A. In *Handbook of Molecular Gastronomy*; CRC Press: Boca Raton, 2021, pp 581–584.

(129) Lazárková, Z.; Kratochvílová, A.; Salek, R. N.; Polášek, Z.; Šiška, L.; Pětová, M.; Buňka, F. *Foods* **2023**, *12*, 2423.

(130) Reig, M.; Aristoy, M.-C.; Toldrá, F. *Food chemistry* **2013**, *140*, 478–482.

(131) Feliu-Alsina, N.; Saguer, E. *Polish Journal of Food and Nutrition Sciences* **2023**, *73*, 130–138.

(132) Schilling, M. W. *Food emulsifiers and their applications* **2019**, 347–377.

(133) Barbut, S *British poultry science* **2007**, *48*, 655–660.

(134) Krog, N. J.; Sparso, F. V. *Food emulsions* **2004**, *12*.

(135) Whiting, R. *Journal of Food Science* **1987**, *52*, 1130–1132.

(136) Neklyudov, A. *Applied Biochemistry and Microbiology* **2003**, *39*, 229–238.

(137) Prestes, R. C.; Carneiro, E. B. B.; Demiate, I. M. *Ciência Rural* **2012**, *42*, 1307–1313.

(138) Prabhu, G.; Doerscher, D.; Hull, D. *Journal of food science* **2004**, *69*, C388–C392.

(139) Onley, J. H.; Bertuzzi, P. F. *Journal of the Association of Official Analytical Chemists* **1966**, *49*, 370–374.

(140) Sousa, S. C.; Fragoso, S. P.; Penna, C. R.; Arcanjo, N. M.; Silva, F. A.; Ferreira, V. C.; Barreto, M. D.; Íris B.S. Araújo *LWT - Food Science and Technology* **2017**, *76*, SLACA 2015: "Food Science for quality of life and health ageing", 320–325.

(141) Prestes, R. C.; Graboski, A.; Roman, S. S.; Kempka, A. P.; Toniazzo, G.; Demiate, I. M.; Di Luccio, M. *Journal of Applied Poultry Research* **2013**, *22*, 885–903.

(142) Jarnot, J. *" Annals of the University of Craiova-Agriculture Montanology Cadastre Series"* **2022**, *52*, 218–223.

(143) Udo, T.; Mummaleti, G.; Mohan, A.; Singh, R. K.; Kong, F. *Food Research International* **2023**, 113369.

(144) Colmenero, F. *Trends in Food Science & Technology* **1996**, *7*, 41–48.

(145) Ghebremedhin, M.; Baechle, M.; Vilgis, T. A. *Physics of Fluids* **2022**, *34*.

(146) Dille, M.; Haug, I.; Draget, K. In *Handbook of hydrocolloids*; Elsevier: 2021, pp 1073–1097.

(147) Liu, G.; Ozores-Hampton, M.; McAvoy, G.; Hogue, B.; Snodgrass, C. A. *EDIS* **2013**, *2013*.

(148) De Villiers, M. *A Practical Guide to Contemporary Pharmacy Practice; Thompson, JE, Ed.; Lippincott Williams and Wilkins: Philadelphia, PE, USA* **2009**, 251.

(149) Van Vliet, T.; van Aken, G. A.; de Jongh, H. H.; Hamer, R. J. *Advances in Colloid and Interface Science* **2009**, *150*, 27–40.

(150) Tunick, M. H. *Journal of agricultural and food chemistry* **2011**, *59*, 1477–1480.

(151) Ray, F. K.; Miller, B.; Van Sickle, D.; Aberle, E.; Forrest, J.; Judge, M. *Journal of Food Science* **1981**, *46*, 694–696.

(152) Han, M.; Clausen, M. P.; Christensen, M.; Vossen, E.; Van Hecke, T.; Bertram, H. C. *Food & function* **2018**, *9*, 4017–4027.

(153) Meyer, T.; Akimov, D.; Tarcea, N.; Chatzipapadopoulos, S.; Muschiolik, G.; Kobow, J.; Schmitt, M.; Popp, J. *The Journal of Physical Chemistry B* **2008**, *112*, 1420–1426.

(154) Roeffaers, M. B.; Zhang, X.; Freudiger, C. W.; Saar, B. G.; Ruijven, M. v.; Dalen, G. v.; Xiao, C.; Xie, X. S. *Journal of biomedical optics* **2011**, *16*, 021118–021118.

(155) Via, M. A.; Baechle, M.; Stephan, A.; Vilgis, T. A.; Clausen, M. P. *Physics of Fluids* **2021**, *33*, 117119.

(156) Bourne, M. *Food Technology* **1978**, *32*, 62–66.

(157) Christie, W. W. *Journal of Lipid Research* **1985**, *26*, 507–512.

(158) Parry, D. A.; Craig, A. S. In *Ultrastructure of the connective tissue matrix*; Springer: 1984, pp 34–64.

(159) Parry, D. A. *Biophysical chemistry* **1988**, *29*, 195–209.

(160) Veis, A.; Cohen, J. *Nature* **1960**, *186*, 720–721.

(161) Moonen, H.; Bas, H. *Emulsifiers in food technology* **2014**, 73–92.

(162) Zhang, T.; Xu, J.; Zhang, Y.; Wang, X.; Lorenzo, J. M.; Zhong, J. *Trends in Food Science & Technology* **2020**, *106*, 113–131.

(163) Lavoisier, A.; Vilgis, T. A.; Aguilera, J. M. *Current research in food science* **2019**, *1*, 31–42.

(164) Guo, L.; Colby, R. H.; Lusignan, C. P.; Whitesides, T. H. *Macromolecules* **2003**, *36*, 9999–10008.

(165) Vilgis, T.; Heinrich, G *Die Angewandte Makromolekulare Chemie* **1992**, *202*, 243–259.

(166) Zielbauer, B. I.; Schönmehl, N.; Chatti, N.; Vilgis, T. A. *Designing of elastomer nanocomposites: From theory to applications* **2017**, 187–233.

(167) Wartewig, S; Helmis, G; Vilgis, T. In *Physics of Polymer Networks*, 1992, pp 1–12.

(168) Dobrynin, A. V.; Rubinstein, M. *Progress in polymer science* **2005**, *30*, 1049–1118.

(169) Kontogeorgis, G. M.; Maribo-Mogensen, B.; Thomsen, K. *Fluid Phase Equilibria* **2018**, *462*, 130–152.

(170) Vilgis, T. A.; Borsali, R. *Physical Review A* **1991**, *43*, 6857.

(171) Wohlert, J.; Edholm, O. *Biophysical journal* **2004**, *87*, 2433–2445.

(172) Vilgis, T. A. *Nature Reviews Physics* **2024**, *6*, 212–214.

(173) Gerrard, J. A. *Trends in food science & technology* **2002**, *13*, 391–399.

(174) Mognard, E. In *Tourism Experiences and Animal Consumption*; Routledge: 2018, pp 119–134.

(175) Normand, V.; Muller, S.; Ravey, J.-C.; Parker, A. *Macromolecules* **2000**, *33*, 1063–1071.

(176) Liu, K.; Stieger, M.; van der Linden, E.; van de Velde, F. *Food Hydrocolloids* **2015**, *44*, 244–259.

(177) Baechle, M.; Via, M. A.; Clausen, M. P.; Vilgis, T. A. *Food Biophysics* **2025**, *20*, 57.

(178) Beccard, S.; Bernard, J.; Wouters, R.; Gehrich, K.; Zielbauer, B.; Mezger, M.; Vilgis, T. A. *Food Hydrocolloids* **2019**, *89*, 302–310.

(179) Nicholson, R. A.; Mazzanti, G.; Marangoni, A. G. *Crystal Growth & Design* **2021**, *22*, 414–427.

(180) Buzała, M; Adamski, M.; Janicki, B. *World's Poultry Science Journal* **2014**, *70*, 531–542.

(181) Marangoni, A. G. In *Lipid biotechnology*; CRC Press: 2002, pp 416–448.

(182) Islam, M.; Bełkowska, L.; Konieczny, P.; Fornal, E.; Tomaszewska-Gras, J. *Journal of Food and Drug Analysis* **2022**, *30*, 185.

(183) Macias-Rodriguez, B. A.; Marangoni, A. A. *Critical Reviews in Food Science and Nutrition* **2018**, *58*, 2398–2415.

(184) Joshi, B. L.; Zielbauer, B. I.; Vilgis, T. A. *Foods* **2020**, *9*, 327.

(185) Chen, W; Lu, F; Frew, D.; Forrestal, M. *J. Appl. Mech.* **2002**, *69*, 214–223.

(186) Funami, T.; Nakauma, M. *Food Hydrocolloids* **2022**, *124*, 107253.

(187) Van Putte, K.; Van Den Enden, J *Journal of the American Oil Chemists' Society* **1974**, *51*, 316–320.

(188) Joshi, B. L.; Graf, R.; Gindra, S.; Vilgis, T. A. *Current Research in Food Science* **2021**, *4*, 784–799.

(189) Jahurul, M.; Zaidul, I.; Norulaini, N. N.; Sahena, F; Abedin, M.; Ghafoor, K.; Omar, A. M. *Food Research International* **2014**, *55*, 103–109.

(190) Chu, B.; Hsiao, B. S. *Chemical reviews* **2001**, *101*, 1727–1762.

(191) Clausen, M. P.; Christensen, M.; Mouritsen, O. G. In *Handbook of molecular gastronomy*; CRC Press: 2021, pp 409–413.

(192) De Freitas Santos, P. D.; Keshanidokht, S.; Kumar, S.; Clausen, M. P.; Via, M. A.; Favaro-Trindade, C. S.; Andersen, M. L.; Risbo, J. *LWT* **2024**, *193*, 115776.

(193) *Animal and vegetable fats and oils — Gas chromatography of fatty acid methyl esters Part 2: Preparation of methyl esters of fatty acids*; Standard; Geneva, CH: International Organization for Standardization, 20017.

(194) *Animal and vegetable fats and oils — Determination of monoacylglycerols, diacylglycerols, triacylglycerols and glycerol by high-performance size-exclusion chromatography (HPSEC)*; Standard; Geneva, CH: International Organization for Standardization, 2005.

(195) Rodrigues, R. C.; Fernandez-Lafuente, R. *Journal of molecular catalysis B: Enzymatic* **2010**, *66*, 15–32.

(196) Sathivel, S.; Prinyawiwatkul, W.; Negulescu, I. I.; King, J. M. *Journal of the American Oil Chemists' Society* **2008**, *85*, 291–296.

(197) Smith, K. W.; Bhaggan, K.; Talbot, G.; Van Malssen, K. F. *Journal of the American oil chemists' society* **2011**, *88*, 1085–1101.

(198) Jariyavidyanont, K.; Schick, C.; Androsch, R. *Thermochimica Acta* **2022**, *717*, 179349.

(199) Arita-Merino, N.; van Valenberg, H.; Gilbert, E. P.; Scholten, E. *Crystal Growth & Design* **2020**, *20*, 5193–5202.

(200) De Arcangelis, L.; Redner, S; Herrmann, H. *Journal de Physique Lettres* **1985**, *46*, 585–590.

(201) Cates, M. E.; Edwards, S. F. *Proceedings of the Royal Society of London. A. Mathematical and Physical Sciences* **1984**, *395*, 89–109.

(202) Vilgis, T. A. In *Handbook of Molecular Gastronomy*; CRC Press: 2021, pp 130–138.

(203) Tabak, T.; Yılmaz, İ.; Tekiner, İ. H. *International Journal of Gastronomy and Food Science* **2021**, *25*, 100398.

(204) Clark, M. G.; Brasseale III, K. A.; Gonzalez, G. A.; Eakins, G.; Zhang, C. *Journal of Visualized Experiments (JoVE)* **2022**, e63677.

(205) Forged by Vow - lab grown foie gras pâté Accessed: (Apr. 14th 2025), Vow Group Pty Ltd, `https://www.forgedbyvow.com/our-craft`.

Acknowledgements

Appendix A

Supporting Information of published Papers

A.1 Microscopic Characterization of Fatty Liver based Emulsions: Bridging Microstructure and Texture in Foie Gras and Pâté

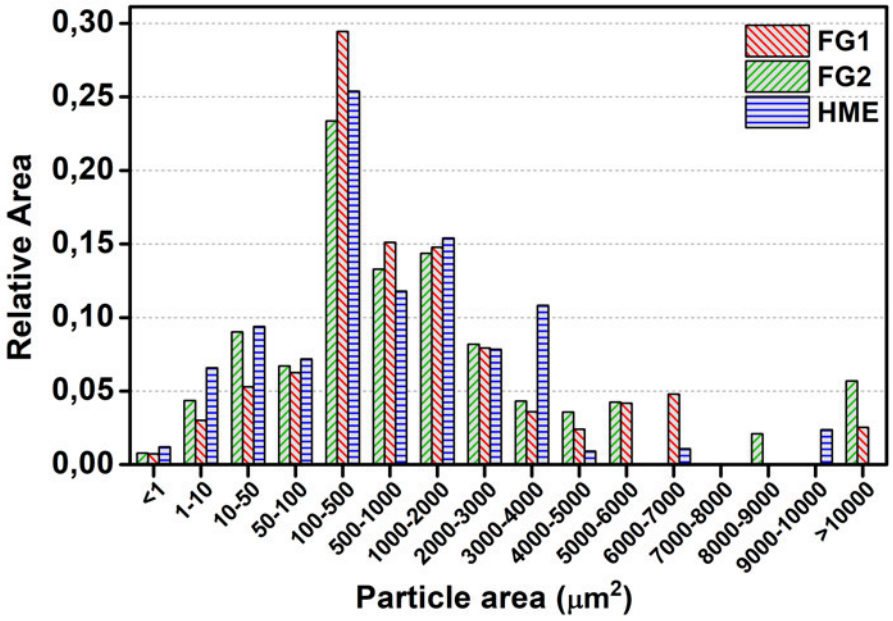

Figure A.1: Fat particle distribution weighed by area of FG1 (red), FG2 (green), and HME (blue).

A.2 Function of Different Emulsifiers in Spreadable Meat Emulsions: A Systematic Study of Physical Properties

A.2.1 Area changes

The area changes were calculated as the differences in relative area covered before and after heating of the samples. $\Delta A = A_{heated} - A_{unheated}$ Therefore, a negative ΔA means area reduction and a positive ΔA more area coverage.

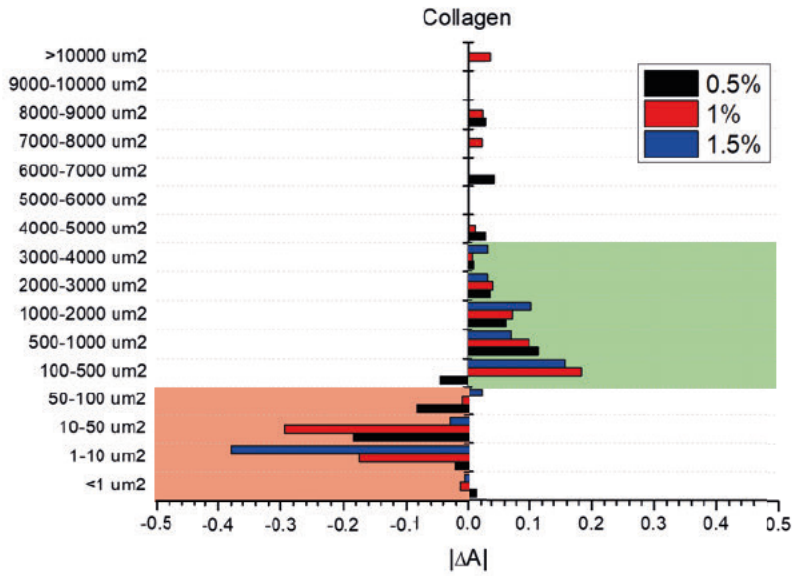

FIGURE A.2: Fat particle merging in collagen samples during cooking. Particles smaller than 100 μm^2 merge to bigger particles of size ranges from 100 to 4000 μm^2

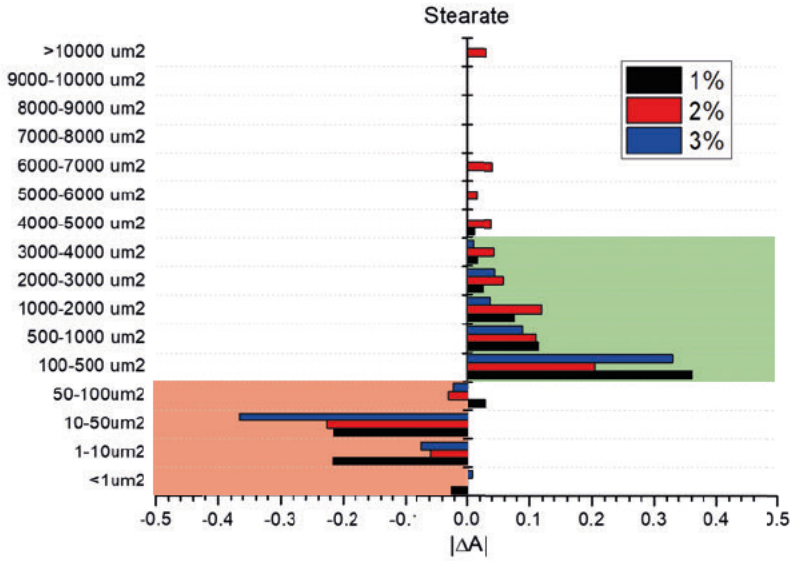

FIGURE A.3: Fat particle merging in stearate samples during cooking. Particles smaller than 100 μm^2 merge to bigger particles of size ranges from 100 to 4000 μm^2

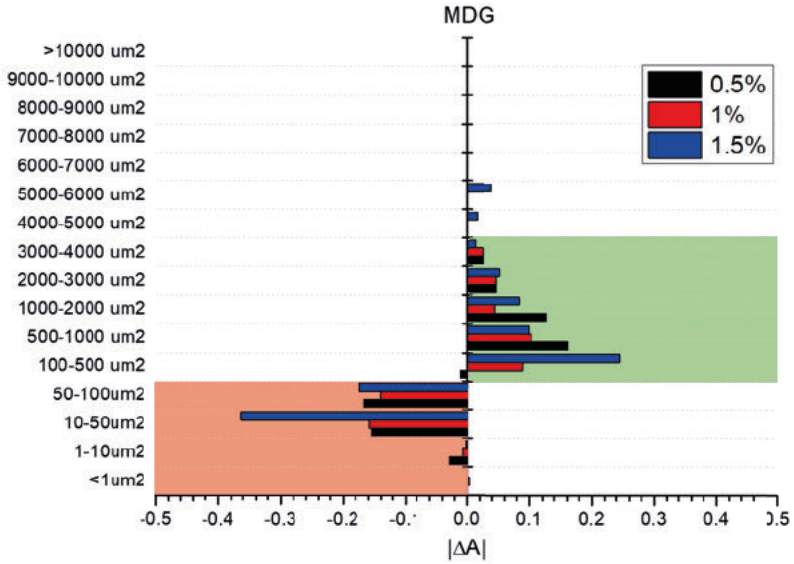

FIGURE A.4: Fat particle merging in MDG samples during cooking. Particles smaller than 100 μm^2 merge to bigger particles of size ranges from 100 to 4000 μm^2

A.3 Foie Gras Pâté without Force-Feeding

A.3.1 Solid fat content - NMR Spectra

The determination of the solid fat content (SFC) based on NMR is evaluated by integration of the full spectrum $A_{(fs)}$ and of the sharp peak $A_{(sp)}$. The SFC is calculated with the following equation $SFC(\%) = 1 - LFC * 100\%$. Where liquid fat content (LFC) is calculated by the fraction of $A_{(sp)}$ divided by $A_{(fs)}$ (see Fig. A.5).

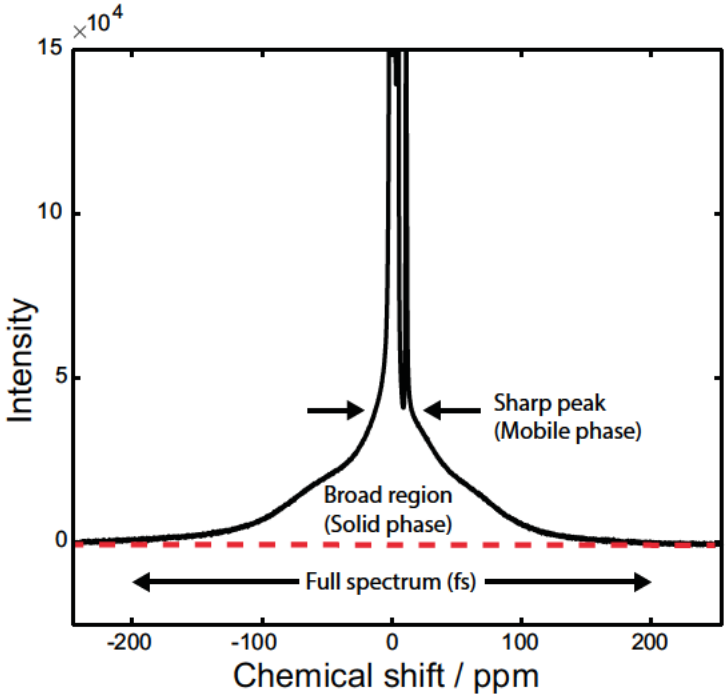

FIGURE A.5: Example NMR spectrum with highlighted sharp peak (sp) of the mobile phase and the broad peak of the solid phase. To estimate the solid fat content, the Integral of the full spectrum (red line) $A_{(fs)}$ and sharp peak $A_{(sp)}$ have been evaluated.

In the following figures (Fig. A.6 to A.9) are example spectra of NMR measurements of the different fat samples at different temperatures (T=−20 °C, T=5 °C and T=35 °C) are shown.

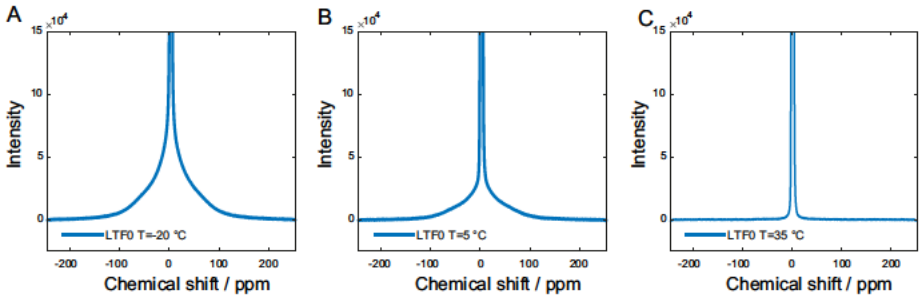

FIGURE A.6: Example NMR spectra for the LTF0 sample. Part A shows spectra at −20 °C, whereas Part B shows the sample at 5 °C. In Panel C the spectra measured at 35 °C is shown.

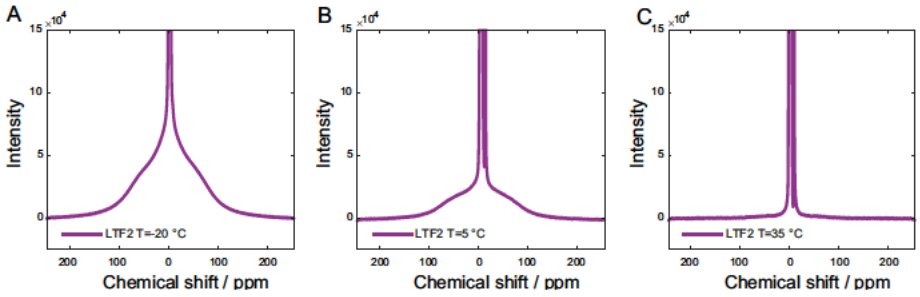

FIGURE A.7: Example NMR spectra for the LTF2 sample. Part A shows spectra at −20 °C, wheras Part B shows the sample at 5 °C. In Panel C the spectra measured at 35 °C is shown.

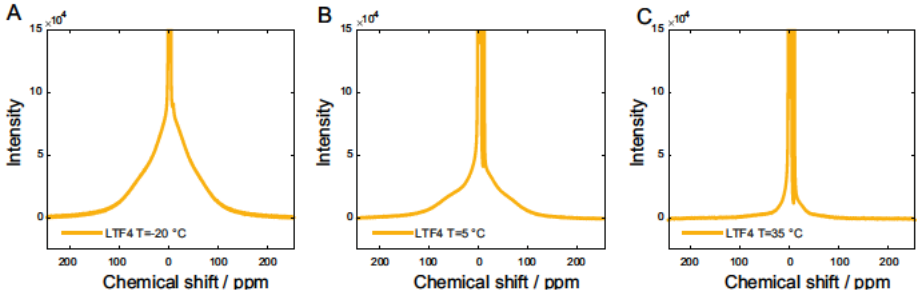

FIGURE A.8: Example NMR spectra for the LTF4 sample. Part A shows spectra at −20 °C, whereas Part B shows the sample at 5 °C. In Panel C the spectra measured at 35 °C is shown.

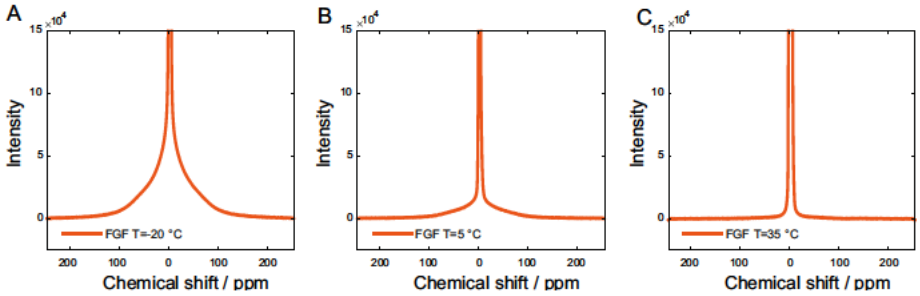

FIGURE A.9: Example NMR spectra for the FGF sample. Part A shows spectra at −20 °C, whereas Part B shows the sample at 5 °C. In Panel C the spectra measured at 35 °C is shown.

A.3.2 DSC - Crystallization

The DSC experiments (see Fig. A.10 A) indicate a notable distinction in the melting and crystallization behavior between the native (rendered) duck fat (LTF0) and the foie gras fat (FGF). Whereas foie gras fat first very broad and pronounced multiple melting regime starting from −20.5 °C to 14.6 °C with a pronounced peak at 4.4 °C (A.10 C, peak no. 21). Immediately it is followed by a second melting regime between 14.7 °C and 44.2 °C, with two peaks at 19.4 °C (peak no. 23) and 38.5 °C (peak no. 27). Native, rendered duck fat exhibits melting already at temperatures between −23.2 °C and −2.6 °C with a peak at −10.8 °C, peak no. 17 in A.10 C, a distinct melting between −2.3 °C and 7.5 °C (peak no. 18: 1.3 °C), followed by another broad melting regime between 8.9 °C and 40.2 °C with peaks at 14.9 °C and 35.9 °C (peak nos. 22 and 26).

Thus, the comparison of the melting profile shows, that pure rendered duck fat will not be able to imitate the melting behaviour of foie gras fat, especially in the temperature range between 0 °C and 37 °C, relevant for oral processing, where their melting profiles are different. Rendered (native) duck fat melts at lower temperatures, and thus the long-lasting melting effect known from foie gras is missing.

Table 1 in the main paper shows the molecular origin of then differences in the melting properties. Foie gras fat contains more saturated fatty acids than rendered duck fat, especially stearic acid, C18:0, which is about the double in concentration. Furthermore, oleic acid, C18:1, is found to be significantly more prevalent at 51 % than in rendered fat at 43 %. On the other hand, more linoleic acid, C18:2, appears in rendered fat than in foie gras fat. Only the concentration of palmitic acid, C16:0, is about the same in both fats.

Lipase treatment shows for both exposure times, 2h and 4h, an equalization of the melting and crystallization curves compared to rendered duck and foie gras fat. The multiple melting peaks and regimes between −23.2 °C and 8.9 °C are blurred and joined on a more pronounced broader peak (LTF2: no. 20, LTF4: no. 20) ranging between −16.1 °C to about 6.7 °C. In addition, two lower melting peaks nos. 13, 14 and 15, 16, appear around −37 °C and around −19 °C (see Fig. A.10 C). These low-temperature peaks can be addressed to the melting points of short chain fatty acids or poly unsaturated fatty acids. The melting ranges of the unsaturated linolenic acid (C 18:3) and arachidonic acid (C 20:4) are determined −21.0 °C to 10.4 °C and −43.4 °C to 38.4 °C These correspond to the result from Fig.A.10. Table 1 in the main paper shows that these fatty acids have been cleaved by the lipase from rendered duck fat, since the corresponding much broader crystallization peak shows at about 10 °C higher temperatures. The low-temperature peaks 13 and 14 proof the cleaving process, however, these fractions do not play a significant role in the mouthfeel and serve merely as a useful check.

In foie gras fat samples these low-temperature peaks do not show up in the melting, despite their presence, because these fatty acids are mostly bound in triglycerides and cannot form larger crystals among themselves. However, signatures of triglycerides

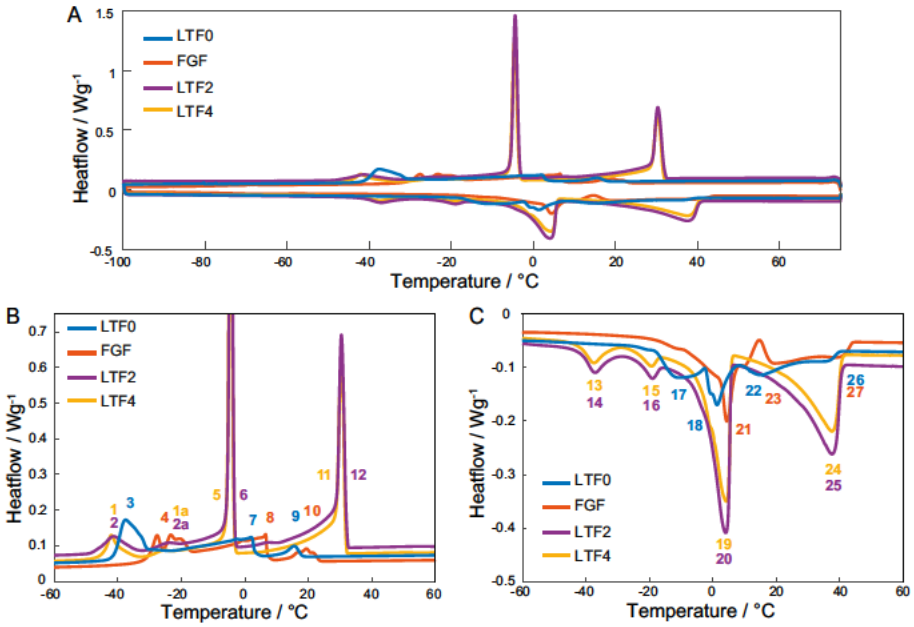

FIGURE A.10: Panel A displays the mean DSC curve for each fat sample. Panel B provides a magnified view of the crystallization process of the DSC measurements. Panel C illustrates the melting profile during the heating of the fat samples. The untreated duck fat (LTF0) is shown in blue, the fat extracted from the foie gras pâté is marked in red (FGF). The two different lipase treated fat samples are plotted in purple (2 h: LTF2) and yellow (4 h: LTF4).

containing polyunsaturated fatty acids can be detected in the crystallization profile Fig.A.10 B in the temperature −30 °C to −18 °C.

The pronounced melting peaks 19 and 20 in Fig.A.10 A and C within the range −5 °C to 15 °C after lipase treatments are most likely generated from oleic acid, C18:1 dominated crystals, which takes a large fraction in the duck fat, as can be seen in Table 1. The corresponding crystallization peaks 5 and 6 can be located at about −5 °C and −10 °C. Thus suggests again, that a sufficient number of the C 18:1 fatty acids are cleaved from the triglycerols in the rendered fat to form reversible melting in crystallization.

It is evident that the melting peaks are considerably broader in width and thus encompass a more extensive temperature range than the crystallization peaks. Most important for the texture and the mouthfeel are the pronounced melting regimes between −8.9 °C to 6.6 °C and the broad regime between 6.7 °C and 42.4 °C, which are induced by the lipase treatment. These melting peaks (LTF2: peak nos 20 and 25, LTF4: peak nos. 20 and 24) show a broad distribution starting with a shoulder to lower temperatures, leading to a peak temperature of 4.1 °C and 37.6 °C.

A comparison between the foie gras fat (FGF) shows immediately, that this lipase treatment induced melting region is similar with the melting regime of the foie gras. In other words, the broad melting regime of the LTF0 (native duck fat) between peaks nos. 22 and 26 becomes shifted to higher temperature ranges, close to the FGF. This is quite intriguing, since the lipase action under given time and activity increases the

number of free fatty acids in such a way the higher effect of the higher amount of C18:0 lipids in foie gras becomes compensated.

TABLE A.1: Enthalpy of melting ΔH_m and peak temperatures of the melting profile and enthalpy of crystallization ΔH_c and peak temperatures of the crystallization profile for untreated duck fat (LTF0), extracted foie gras fat (FGF) fat and 2h and 4h lipase treated fat (LTF2,4) samples. In Fig. A.10 the corresponding crystallization peaks are numbered in part B and the melting peaks are marked in C.

			Melting			
Sample	Peak no.	17	18	22	26	Total ΔH_m
LTF0	T / °C	-10.8 ± 0.1	1.3 ± 0.1	14.9 ± 0.6	35.9 ± 0.4	
	ΔH_m / J/g	-22.0 ± 0.7	-21.7 ± 0.6	-28.2 ± 0.7		-71.9 ± 1.9
	Peak no.	21	23	27		Total ΔH_m
FGF	T / °C	4.4 ± 0.1	19.4 ± 0.1	38.5		
	ΔH_m / J/g	-40.7 ± 4.1	-24.5 ± 2.3			-65.1 ± 6.5
	Peak no.	14	16	20	25	Total ΔH_m
LTF2	T / °C	-40.2 ± 2.31	-19.4 ± 0.9	4.0 ± 0.1	37.5 ± 0.1	
	ΔH_m / J/g	-9.7 ± 0.1	-8.5 ± 1.5	-66.5 ± 1.5	-61.9 ± 1.2	-146.6 ± 4.3
	Peak no.	13	15	19	24	Total ΔH_m
LTF4	T / °C	-37.5 ± 0.1	-19.4 ± 0.5	4.2 ± 0.1	37.4 ± 0.1	
	ΔH_m / J/g	-9.1 ± 0.2	-8.2 ± 0.7	-67.5 ± 0.5	-61.04 ± 0.3	-145.9 ± 1.7
			Crystallization			
	Peak no.	3	7	9		Total ΔH_c
LTF0	T / °C	-37.5 ± 0.1	2.0 ± 0.1	15.4 ± 0.2		
	ΔH_c / J/g	31.7 ± 0.7	33.4 ± 0.8	4.9 ± 0.1		70.0 ± 1.5
	Peak no.	4	8	10		Total ΔH_c
FGF	T / °C	-23.3 ± 0.1	6.5 ± 0.1	19.4 ± 0.3		
	ΔH_c / J/g	28.7 ± 2.3	37.5 ± 2.2	7.9 ± 0.5		74.1 ± 5.0
	Peak no.	2	2a	6	12	Total ΔH_c
LTF2	T / °C	-41.5 ± 0.2	-21.8 ± 1.9	-4.5 ± 0.2	30.4 ± 0.1	
	ΔH_c / J/g	10.1 ± 0.1	5.9 ± 0.4	63.5 ± 1.1	60.9 ± 1.2	140.4 ± 3.0
	Peak no.	1	1a	5	11	Total ΔH_c
LTF4	T / °C	-42.2 ± 0.1	-24.4 ± 3.25	-4.6 ± 0.2	30.6 ± 0.1	
	ΔH_c / J/g	10.6 ± 0.4	4.4 ± 0.6	63.8 ± 1.4	61.3 ± 1.3	140.1 ± 3.6

The peaks of the lipase treated samples indicate a higher heat flux than the native and FG fat samples. Integration of the peaks shows that the enthalpy of melting is, with around $-146\,\mathrm{J/g}$, two times higher in total in the lipase treated samples (see table A.1) compared to the native duck fat and foie gras fat. The three peaks of the native duck fat contribute with $-22.0\,\mathrm{J/g}$ (peak no. 17), $-21.7\,\mathrm{J/g}$ (peak no. 18) and $-28.2\,\mathrm{J/g}$ for the regime of peak nos. 22 and 26 to a total heat of fusion of $-71.9\,\mathrm{J/g}$. For the foie gras fat the two broad regimes have a total melting enthalpy of $-40.7\,\mathrm{J/g}$ (peak no. 21) and $-24.7\,\mathrm{J/g}$ (sum of peak no. 23 and 27). Both lipase treated samples differ only marginal in the release of heat during melting. The peaks of the lipase treated samples in the low-temperature regime contribute with $-17\,\mathrm{J/g}$ to $-18\,\mathrm{J/g}$ (LTF2: peak nos. 14 and 16; LTF4: peak nos. 13 and 15). Whereas the more pronounced peaks in both samples (nos. 20,19 and 25,24 in panel C of fig. A.10) release around $-67\,\mathrm{J/g}$ and $-61\,\mathrm{J/g}$ heat, leading to a total heat of fusion of around$-146\,\mathrm{J/g}$ (see Table A.1.

These differences are also manifested by the crystallization behaviour. The crystallization of different fractions of the foie gras fat (FGF) starts about 3.8 °C to 13.8 °C (peak no. 10) earlier as those of the rendered duck fat (LTF0 peak no. 9). Three different crystallization peaks are visible for both samples and the first starting at

23.9 °C and transition into the next peak no. 8 at 9.0°C for the foie gras fat respectively 4.8 °C (peak no. 7) for the native duck fat. The peak temperature is at6.6 °C for the foie gras fat and 2.1 for the native duck fat, and both show a shoulder to lower temperatures. For the foie gras fat, the last peak no. 4 ranges from −16.4 °C to −36.8 °C and for the native duck fat from −29.7 °C to −44.7 °C (peak no. 3). On the reverse, the corresponding crystallization process starts at 32 °C for both lipase treated samples, with sharp peaks (nos. 11 and 12) at 30.4 °C. They both have a shoulder to higher temperatures ending at −2.3 °C and with a transition into the next peaks at −2.4 °C. The peak maximum of the peaks no. 5 and 6 is at −4.5 °C and has a broader shoulder to lower temperatures, which transition into two peaks nos. 1a and 2a at −24.9 °C and −41.5 °C (peak nos. 1 and 2), as shown in Fig. A.10 Panel B and Table A.1).

As for the melting, the energy released by crystallization is with around 140 J/g for the lipase treated samples as twice as high as for the native duck fat and foie gras fat samples with 70.0 J/g respectively 74.1 J/g (see Table A.1). The crystallization enthalpy of the peaks for the native duck fat is with 31.7 J/g, 33.4 J/g and 4.9 J/g for peak nos. 3,7 and 9 slightly different from the peaks in the melting profile (see Table A.1), which all take up roughly the same amount of energy. The foie gras fat sample has one crystallization peak more compared to the melting peaks. The peaks nos. 4,8 and 10 release 28.7 J/g, 27.5 J/g and 7.9 J/g of energy during the crystallization process. The crystallization profile of both the lipase treated samples are similar to each other and also similar to the corresponding melting peaks. The crystallization enthalpy of the sharp peaks numbered 11 and 12 is approximately 61 J/g, while the peaks numbered 5 and 6 exhibit a crystallization enthalpy of approximately 63.5 J/g, whereas the peaks at lower temperature only release around 10 J/g (peak nos. 1 and 2) and peak nos. 1a and 2a release 4.4 J/g and 5.9 J/g.

A.3.3 Texture measurements - pictures of breaking events

In the following photographs of the texture analyzer measurements are shown to demonstrate the breaking behavior under compression of the samples LTP0, LTP2 and FGP.

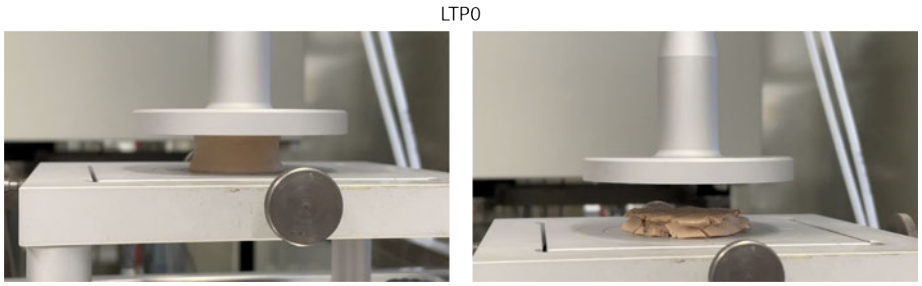

FIGURE A.11: Picture of texture measurement of LTP0 sample. Left side shows the sample during compression and right side shows after the compression.

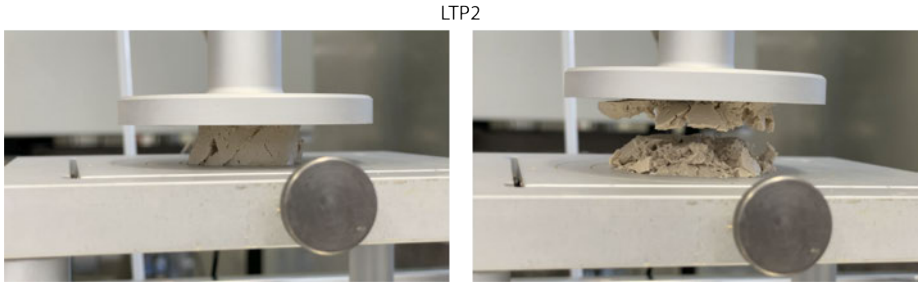

FIGURE A.12: Picture of texture measurement of LTP2 sample. Left side shows the sample during compression and right side shows after the compression.

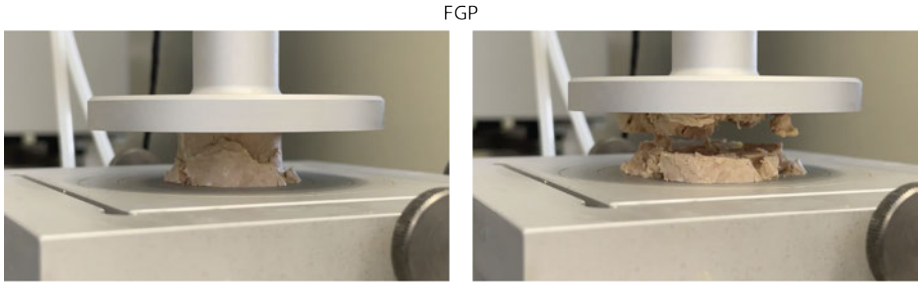

FIGURE A.13: Picture of texture measurement of FGP sample. Left side shows the sample during compression and right side shows after the compression.

Appendix B

Copyrights of Published Papers

B.1 Microscopic Characterization of Fatty Liver based Emulsions: Bridging Microstructure and Texture in Foie Gras and Pâté

The manuscript and supporting information of *Microscopic Characterization of Fatty Liver based Emulsions: Bridging Microstructure and Texture in Foie Gras and Pâté* is an open access article which permits an unrestricted use under terms of the Creative Commons CC BY license.

Figure B.1: Copyright Microscopic Characterization of Fatty Liver based Emulsions: Bridging Microstructure and Texture in Foie Gras and Pâté

B.2 Function of different emulsifiers in spreadable meat emulsions: A systematic study of physical properties

The manuscript and supporting information of *Function of different emulsifiers in spreadable meat emulsions: A systematic study of physical properties* is an open access article which permits an unrestricted use under terms of the Creative Commons CC BY license.

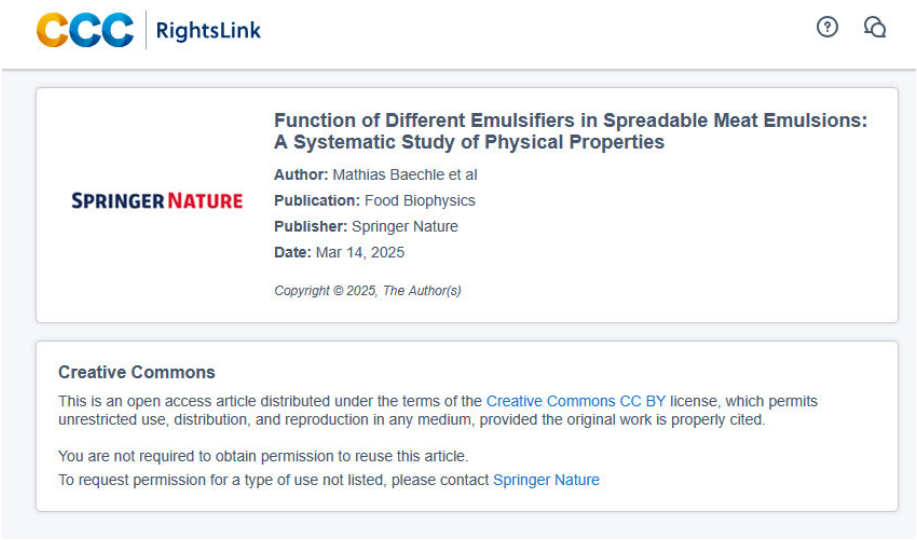

FIGURE B.2: Copyright Function of different emulsifiers in spreadable meat emulsions: A systematic study of physical properties

B.3 Foie gras pâté without force-feeding

The manuscript and supporting information of *Foie gras pâté without force-feeding* is an open access article which permits an unrestricted use under terms of the Creative Commons CC BY license.

FIGURE B.3: Copyright Foie gras pâté without force-feeding

Appendix C

Declaration of use of AI-tools

Table C.1: The following AI-Tools were used during writing this Thesis

AI tool	**Used for**	**Reason**	**Time of Usage**
DeepL write	Correction of drafts and Text	Improved readability	During complete work
DeepL translate	Translation of Abstract	consistency of both texts	Writing abstract.
ChatGPT	Outline of theory chapter in keywords	Improvement of Chapter structure	Writing theory
ChatGPT	Explaining certain aspects of theory	Enhance insights	Writing Theory chapter
ChatGPT	Alternative phrasing of sentences	Improve readability and comprehensibility	During correction